UNIVERSITY OF CALIFORNIA,
IRVINE

DETERMINATION OF THE COMPLEX PERMITTIVITY OF PACKAGING MATERIALS AND DESIGN OF AN ANTENNA ARRAY FOR THE 60GHz BAND

THESIS

submitted in partial satisfaction of the requirements for the degree of

Telecommunications Engineering
and
Computer Sciences Engineering

by

Anna Papió Toda

Thesis Advisor:
Professor Franco de Flaviis

© 2008 Anna Papió Toda

The Thesis of Anna Papió Toda is approved by:

_____

_____

_____

Thesis Committee

University of California, Irvine
2008

"Whatever the mind can conceive and believe, it can achieve."

Dr. Napoleon Hill

RESUMEN

Titulo: Calculo de la permitividad compleja de materiales usados en PCB y diseño de una agrupación de antenas para la banda de 60GHz.

Con la aparición de una multitud de aplicaciones multimedia que requieren grandes velocidades de transmisión de datos, la demanda de sistemas de comunicación sin hilos que satisfagan tales necesidades crece diariamente. En concreto, es una necesidad urgente el desarrollo de dichos sistemas de comunicación para los denominados entornos PAN (personal area network) y enlaces punto-a-punto o punto-a-multipunto. Esta demanda ha impulsado el desarrollo de tecnologías y sistemas operando en la banda de frecuencias denominada milimétrica (mm-W).

La disponibilidad de diversos giga-hercios de ancho de banda en el espectro alrededor de los 60GHz representa una oportunidad inmejorable para los sistemas de comunicación sin hilos de alta velocidad y corto alcance. Sin embargo, existen aún numerosos retos para hacer de los sistemas en esta banda frecuencial una solución viable para aplicaciones de consumo.

Los recientes avances en tecnología CMOS y SiGe han hecho posible el diseño de mm-W radios de bajo coste en silicio. En combinación con un óptimo empaquetado, representa una oportunidad única para desarrollar Gb/s radios que podrían dar respuesta a la creciente demanda en términos de capacidad de transmisión de datos de los sistemas de comunicación sin hilos de banda ancha.

El empaquetado de componentes en la banda milimétrica es especialmente exigente por la complejidad asociada en diseño y fabricación. El uso de las técnicas de bajo coste convencionales CSP (chip-scale packaging), PBGAs (plastic ball grid arrays) o DCA (direct-chip-attach) está limitado y solo se ha aplicado a bajas frecuencias. Además, los materiales estándares y PCB (printed circuit board) generalmente no están eléctricamente caracterizados a altas frecuencias.

Por otra parte, el canal de comunicaciones a 60GHz tiene algunas características únicas que difieren significativamente de las características de los canales de comunicación en la banda baja del espectro radioeléctrico. Algunas de esas diferencias son debidas a propiedades electromagnéticas o de los materiales, mientras que otras son causadas por factores extrínsecos, como organismos reguladores. Aunque se han llevado a cabo numerosos estudios y medidas cuantificando diversos parámetros del canal de comunicaciones a 60GHz en entornos cerrados, existe poca información acerca de la dinámica del canal, aún cuando es crítica para determinar las características del diseño de la capa física de los dispositivos.

El propósito de este proyecto es dual. Por una parte, el objetivo es caracterizar eléctricamente en la banda milimétrica diversos materiales utilizados para el empaquetado de chips y PCB. El conocimiento acurado de la permitividad y la tangente de pérdidas de estos materiales va a permitir un diseño mucho mas acurado de los circuitos, puesto que la información disponible a frecuencias más bajas puede no modelar el comportamiento actual de los materiales en las frecuencias de interés.

En este sentido, se han analizado 3 técnicas de medida de permitividad y tangente de pérdidas, comúnmente utilizados a bajas frecuencias. A partir de un análisis utilizando herramientas de simulación electromagnética, se ha determinado su exactitud y aplicabilidad a las frecuencias de interés. El primer método consiste en una línea microstrip, impresa sobre un material "conocido" a 60GHz, que se cubre con el material de test. Diversos análisis demuestran el correcto funcionamiento para la determinación de la permitividad, pero limitada capacidad para la extracción de la tangente de pérdidas. El segundo método representa una variante del anterior, utilizando una línea coplanar en lugar de la microstrip. Diversas simulaciones y resultados resultan incoherentes entre ellos, por lo cual se establece que el método no es útil. El último método consiste en un resonador, que también se cubre con el material de test. Los resultados de las simulaciones prueban su correcto funcionamiento pero demuestran menos precisión en la determinación de la tangente de pérdidas.

Finalmente, se ha procedido al diseño de un prototipo para implementar el primero de los métodos. La calibración y correcta simulación del prototipo se demuestran imprescindibles para la obtención de resultados correctos. Las medidas en el laboratorio y los datos proporcionados por los fabricantes de materiales son comparadas, comprobándose el correcto funcionamiento del sistema de medida.

Por otra parte, el objetivo es diseñar una agrupación de antenas para la banda de 60GHz, con el propósito de utilizarlo para medidas de canal. Una agrupación de antenas permite caracterizar la variación temporal del canal MIMO (múltiple input-multiple output) puesto que la matriz de canal se puede capturar casi instantáneamente. Esto es crítico para desarrollar algoritmos de formación de haz en la banda milimétrica.

En base a los estudios de canal realizados hasta el momento a 60GHz y las características que se anhelan en los futuros dispositivos móviles, se establecen algunas de las especificaciones para la agrupación de antenas. Teniendo en cuenta también que se desea un sistema MIMO, cada antena debe controlarse individualmente con un transceptor. Dicho transceptor se comercializa actualmente y nos va a determinar en gran medida el diseño. El diseño inicial para la agrupación de antenas, consistente en 8 guías de onda radiando al aire libre. Un análisis teórico basado en las formulas de radiación en espacio libre de guías de onda y horn antenas acaba refinando el diseño.

Posteriormente, se presenta un estudio basado en simulaciones electromagnéticas que nos permite inferir el efecto de la red de alimentación en el funcionamiento de la agrupación. Dicha red de alimentación está pensada para permitir la conexión directa de cada transmisor o receptor a una antena, con la peculiaridad que todos los caminos de

derivación de la señal deben tener la misma longitud. Parámetros como la adaptación, la eficiencia, la directividad y la dirección de radiación en función de la fase de alimentación se consideran para refinar el diseño y escoger los materiales adecuados para un funcionamiento óptimo.

Finalmente, se hace un análisis detallado de la influencia de errores en la fase de la señal de alimentación en el diagrama de radiación, y se presenta un método de corrección de dichos errores.

Para concluir, se presenta una breve guía sobre posibles campos de investigación derivados de este proyecto y se constata la utilidad de este proyecto para las empresas del sector.

Table of Contents

List of Tables

List of Figures

Acknowledgements

I wish to thank the director of my thesis, Prof. Franco de Flaviis for giving me the opportunity to closely work with him and the abundance of research information and guidance he has provided. Equally, I would like to give special thanks to Prof. Lluis Jofre Roca, who introduced me to research and provided a way to come to the University of California Irvine and for his priceless comments and advice.

Thanks to Broadcom Corporation for providing such a nice and unique work environment as well as really valuable technical and economical support. Thanks to the RF team, and especially to Jesus Castaneda, Maryam Rofougaran and Reza Rofougaran. Thanks to Chris Hansen for the guidance and faith in this project. Special thanks to Edward Roth, manager in Engineering Services, for his invaluable help and patience. Thanks to Alfred Grau, Yoon Seunghwan and Michael Boers for their close collaboration, and many thanks to all the work colleagues who have directly or indirectly contributed to the development of this project.

A thank you is in order to the International Relations team from the ETSETB of the Polytechnic University of Catalonia for the help provided in making this project possible. Thanks to the CFIS directors and staff for their continuous effort and assistance to provide the best education opportunities. Thanks as well to Prof. Francesc Guinjoan Gispert and to Prof. Jorge Garcia Vidal for their valuable comments and advice.

Thanks to the financial sponsors Fundació Vodafone Espanya and Ministerio de Educación y Ciencia for supporting numerous research projects contributing to global development.

Last but not least, I would like to give special thanks to my parents and brother, for their unconditional and unique support. Thanks to all my friends worldwide for the advice and the shared experiences and knowledge.

Abstract of the Thesis

DETERMINATION OF THE COMPLEX PERMITTIVITY OF PACKAGING MATERIALS AND DESIGN OF AN ANTENNA ARRAY FOR THE 60GHz BAND

by

Anna Papió Toda

Degree in Telecommunications Engineering and Computer Sciences Engineering
University of California, Irvine, 2008
Prof. Franco de Flaviis, Chair

The demand for ultra-high data rate wireless communication systems is increasing daily with the emergence of a multitude of multimedia applications. In particular, the needs become urgent for ultrahigh speed personal area networking and point-to-point or point-to-multipoint data link. This demand has pushed the development of technologies and systems operating at the millimeter-wave (mm-W) frequencies.

The availability of several GHz bandwidth unlicensed ISM (Industrial, Scientific and Medical) bands in the 60GHz spectrum represents a great opportunity for ultra-high speed short-range wireless communications. However, a number of challenges remain for this spectrum to be a viable solution for high volume consumer applications.

The recent advances of CMOS (Complementary Metal-Oxide-Semiconductor) and SiGe process technologies have now made the design of low-cost highly integrated millimeter-wave (mm-W) radios possible in silicon. In combination with an optimum packaging approach, this represents a unique opportunity to develop Gb/s radio that could address the increasing demand in terms of data throughput of the emerging broadband wireless communication systems.

Packaging of mm-W components is particularly challenging because of the associated complexity in both the design and fabrication. The use of low-cost conventional chip-scale packaging (CSP), plastic ball grid arrays (PBGAs) or direct-chip-attach (DCA) technologies is limited and has only been reported at lower frequencies. Moreover, standard mold materials and PCB (Printed Circuit Board) materials have not generally been characterized at millimeter-wave frequencies.

The 60GHz channel has some unique characteristics that differ significantly from the characteristics of communication channels in the low-GHz regime. Some of these differences stem from basic electromagnetic or materials properties whereas some are caused by extrinsic factors such as practical issues regarding device from factor. Although numerous studies and measurement campaigns quantifying various parameters of the 60GHz indoor channel have been conducted, existing 60GHz channel models have provided little information on channel dynamics, even though this information is critical for determining the requirements for the PHY (Physical Layer) design and especially for beamforming.

The purpose of this project is twofold. On the one hand, the objective is to electrically characterize several standard packaging materials at mm-W frequencies. Accurate permittivity and loss tangent measurements of these materials will allow for greater design accuracy, as properties may vary substantially from those at low frequencies and available data may not model the actual behavior.

On the other hand, the objective is to design a 60GHz antenna array for channel measurements. A transceiver for each antenna on the array allows characterization of the time varying MIMO (Multiple Input Multiple Output) channel since the entire channel matrix can be captured almost instantaneously. This is critical for developing 60GHz beamforming algorithms.

Chapter 1

Introduction

1.1. Trends in High Data-Rate Wireless Systems

Wireless technology has had a dramatic impact on the way we work, live and play. Fifteen years ago, it was unthinkable to imagine that an individual could have data connectivity anywhere other than at a terminal or desktop that was tethered to an Ethernet port or dial-up modem. Today, it is commonplace to assume that, through the use of wireless communications technology, a person can have voice, video, and data access anywhere in his office, his home, or just about any corner of the globe. With the rapid commercialization of wireless local area networking (WLAN) technologies such as 802.11 over the past several years, achievable indoor wireless data rates have scaled from roughly 1 Mb/s to over several hundreds of Mb/s. This growth in bandwidth has enabled a host of new technologies and applications, including real-time audio and video streaming. Furthermore, the use of wireless, instead of wired, communications technology has helped spread the overall adoption of the technology in the consumer market, as ease of installation and customer satisfaction is greatly increased by the elimination of unwieldy and unsightly wires and cables.

As wireless access has become an increasingly important part of our everyday lives, the demand for wireless bandwidth similarly increases. Applications that were typically run over traditional wired networks can now be easily run on 802.11 wireless networks. Similarly, recent developments in ultrawideband (UWB) technologies show promise for delivering "wireless USB" connectivity between computers and storage-intensive peripherals like digital cameras, camcorders, and external hard disk drives at rates of up to 480Mb/s [1].

However, there are new wireless applications [2, 3] that demand even greater bandwidth than either 802.11 or UWB can provide. With the widespread adoption of HDTV's and sources of HD content (such as HD set-top boxes, Blu-Ray DVD players, HD camcorders, et al), there is growing demand for real-time wireless streaming between these various HD devices. Similarly, wireless connectivity between a PC and a display is desirable in many environments. Additionally, the prevalence of mobile personal video players motivates for the capability to "instantaneously" synchronize and transfer large media files between the mobile device and a personal computer over a high-speed wireless link. As shown in figure 1.1, these applications require throughput exceeding 1

Gb/s, well beyond the capacity of existing wireless systems. Therefore, other technologies must be developed in order to accommodate these new applications. These applications require short-range (1-10m) wireless communications capable of handling throughputs of 1 Gb/s and above in typical indoor residential and corporate environments.

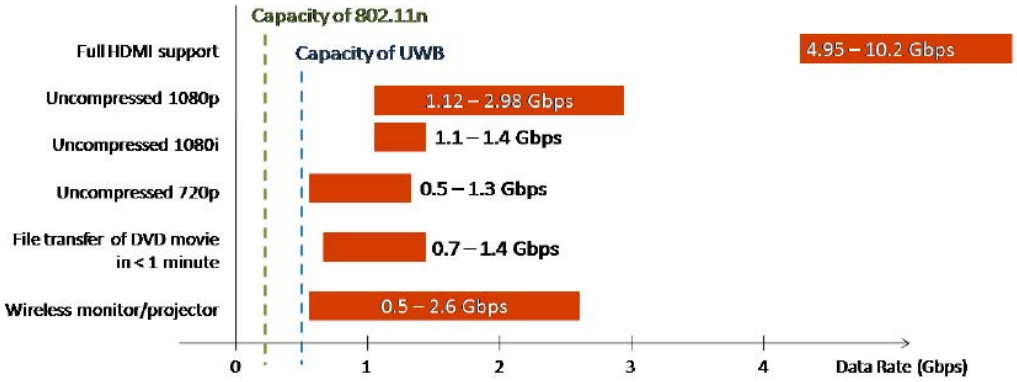

Fig. 1.1: New wireless applications and their associated data rate requirements.

1.2. Recent Developments in 60GHz Regulatory and Industrial landscape

In 1995, the FCC (Federal Communications Commission) allocated the spectrum from 59GHz to 64GHz as an unlicensed band [4]. Shortly thereafter, the FCC amended their rules to extend this unlicensed band to 57-64GHz, thus providing 7GHz of unlicensed spectrum for general purpose use [5]. Furthermore, regulatory bodies across the globe have also set aside multi-GHz blocks of spectrum at 60GHz for unlicensed use; Japan has allocated 59-66GHz as an unlicensed band and Europe has allocated 57-66GHz.

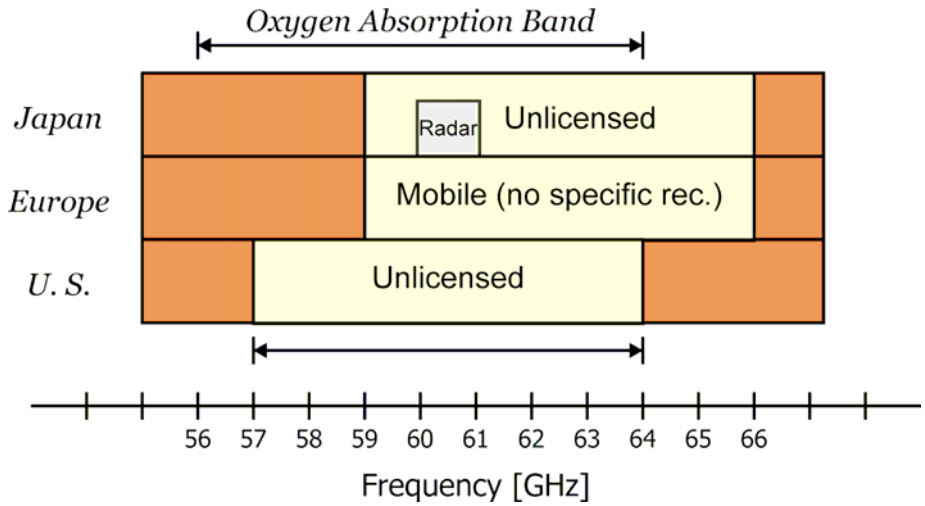

Fig. 1.2: Worldwide allocation of unlicensed spectrum around 60GHz.

The availability of a true multi-GHz worldwide band has sparked immense commercial interest in developing 60GHz technology in order to meet the demands of these new

high-bandwidth wireless applications. In 2005, IEEE (Institute of Electrical and Electronics Engineers) organized the 802.15.3c task group to develop a standard for a 60GHz wireless personal area network with bandwidths in excess of 1Gb/s [6]. Around that same timeframe, several companies began research and development of 60GHz wireless technology for commercial applications and joined efforts to develop other standards, such as the NGMS or the WirelessHD [7].

1.3. Research goals and contributions

The goal of the research presented here is to provide or help obtain relevant data for the development of future WLAN 60GHz communication systems. In this sense, investigation is focused on two main directions:

1. Determination of the complex permittivity of packaging and substrate materials.
2. Design of a high-gain 60GHz array to aid channel measurements.

Accurate measurement of packaging and substrate materials will allow for greater 60GHz systems design accuracy, as properties can vary substantially from low frequencies and available data may not model the actual behavior. Some measurement techniques are analyzed and experimental permittivity and loss tangent measurement results are provided for some common PCB materials.

A multiple antenna array with one transceiver for each antenna forming the array allows characterization of the time varying MIMO channel since the entire channel matrix can be captured almost instantaneously. This is critical for developing 60GHz beamforming algorithms. Since 60GHz arrays are not commercially available and only some design attempts have been reported in literature [8-10] but do not meet our design criteria, a novel 60GHz waveguide array is designed and the frequency behavior optimized.

1.4. Organization of the Dissertation

The rest of this dissertation is organized in two parts according to the two differentiated research objectives. Part I exposes the problem and need of electrically characterizing packaging and substrate materials at mm-Wave frequencies and explores different techniques to determine the complex permittivity of these materials. In Chapter 2 fundamental concepts related to dielectric properties of microelectronic substrate materials are reviewed. Chapter 3 presents various frequency-dependent permittivity measurement methods and in chapter 4 their performance is analyzed using electromagnetic (EM) simulation tools. Chapter 5 gives permittivity measurement results on substrate and circuit-board materials.

Part II analyses the key characteristics of the 60GHz channel and the need of further channel studies (Chapter 6). The need of high gain antennas for mm-Wave communications and previous determination of communication system requirements is evidenced. Chapter 7 presents waveguide and radiation theory and in chapter 8 a 60GHz high-gain waveguide array is designed and analyzed both theoretically and by simulation. Chapter 9 gives an insight on 60GHz channel studies conducted to the moment by other research groups.

Part I

Determination of the Complex Permittivity of Packaging Materials at mm-W Frequencies

Introduction

Dielectric materials have many important functions in the microelectronics industry. New packaging technology requires substrates with low permittivity, interconnections made of high-conductivity metals, high wiring density and embedded passive circuit elements. The use of fine-line signal conductors requires thinner, laminated, printed wiring board (PWB), thin films, low-temperature co-fired ceramics (LTCC) and other substrate materials. As electrical components are miniaturized, the need for well-characterized dielectric measurements on thin materials increases. Accurate measurement of complex permittivity is needed for circuit design, minimization of crosstalk and characterization of signal-propagation speed.

In Chapter 2 we review important fundamental concepts related to dielectric properties of microelectronic substrate materials. This includes the types of materials and laminates commonly used and the definitions of important electrical concepts. In Chapter 3 and 4 we present and theoretically analyze three frequency-dependent permittivity measurement methods for thin materials. In Chapter 5 a prototype for dielectric measurements is developed and measurement results of substrate and circuit-board materials are presented.

Chapter 2

Dielectric Materials

2.1. Overview of Packaging Technology and Materials

Substrates are used in PWBs, central processing units, and for thin films. Important properties of substrate materials include low electrical loss, high thermal conductance, low thermal expansion, and high interfacial adhesion to metal surfaces or other films (see table 2.1). Low electrical loss decreases heating and signal attenuation, high thermal conductivity rapidly removes heat from the circuit and low thermal expansion promotes circuit durability.

In high-speed or high-frequency circuits, the speed of signals propagation is important. The signal propagation delay depends on both the dielectric constant and the transmission-line structure. This dependence is manifest in the equation for propagation delay for transverse electromagnetic (TEM) propagation modes which, in a lossless line is:

$$t_d = \frac{l\sqrt{\varepsilon'_r \mu'_r}}{c} \tag{2.1}$$

where c is speed of light in vacuum, l is line length, μ'_r is the real part of the relative permeability given by $\mu = \mu_0[\mu'_r - j\mu''_r]$, ε'_r and ε''_r are the real and imaginary parts of the relative permittivity, $\varepsilon = \varepsilon_0[\varepsilon'_r - j\varepsilon''_r]$, and ε_0 and μ_0 are the permittivity and permeability of vacuum. ε'_r provides a measure of the relative phase change as a sinusoidal signal propagates through a material. ε''_r is related to attenuation of the signal and includes both dielectric and dc-conductivity losses. Generally, the loss in a material is expressed in terms of the loss tangent, $\tan\delta = \varepsilon''_r/\varepsilon'_r$. Dielectrics with low loss provide reduced attenuation and heating in circuits. They also provide greater signal integrity.

Property	Advantages	Desired range
Low permittivity	Minimize cross talk	$\epsilon'_r \approx 1-4$
	Decreased propagation delay	
High-medium permittivity	Smaller circuits	$\epsilon'_r \approx 8-500$
	Generate phase changes	
Low loss	Less heat generated	$\tan\delta < 5\times10^{-4}$
	Less signal attenuation.	
Low thermal expansion	Less circuit failure	$\alpha < 10^{-5}(°C^{-1})$
	Less impedance	
	temperature dependence	
High thermal conductance	Cooler operation	$k > 30$ $(W/m°C)$

Table 2.1: Summary of substrate properties and applications.

The propagation delay can be reduced by using substrates with a low value of ε'_r, by using different transmission-line structures such as microstrip, stripline, coplanar waveguide, coplanar strips, or by varying the geometries of signal line widths and conductor spacings of the transmission-line structure. Crosstalk is also an important parameter in the design of high-speed or high-frequency circuits. Crosstalk can increase the noise and spurious content on signal lines, which will affect both analog and digital circuits. A low value for ε'_r can decrease the signal crosstalk between conductors by decreasing the capacitive coupling. Materials with low dielectric constants include Teflon, cross-linked polystyrene and fused silica.

2.2. Ceramic Substrates

Ceramic substrate designs include thick film, plated copper, photo-patterned thick film, high-temperature co-fired ceramics (HTCC), and low-temperature co-fired ceramics (LTCC). The advantages of ceramic materials over polymers for substrates are durability, low thermal expansion coefficient, and relatively high thermal conductivity. High permittivity manifests itself in slower propagation speed and larger crosstalk in circuits. The propagation speed varies roughly as the square root of ε'_r. The permittivity of ceramics is strongly influenced by the microstructure. Ceramics with lower than theoretical density have a lower permittivity and higher loss due to interfacial charges on the pore surfaces. Grain size also influences permittivity.

In LTCC technology [11] it is possible to fire the ceramics with embedded passives and conductors. The type of metal used as a conductor for a specific application is related to its melting temperature, resistivity, migration resistance, cost, line resolution and solderability. Typical conductors used in LTCC are aluminum, copper, gold, silver and palladium-silver alloys. The embedded passives include resistors made from lossy metallic films, inductors, made from spiraled or serpentine conductors, and capacitors, made from high-permittivity materials.

The ability to include components into the modules reduces the number of interconnects which increases reliability and reduces the size and the cost. LTCC technology also allows for a high density of signal lines throughout the module and vias as small as 75um in diameter. Another advantage of ceramic multichip modules (MCM-C) over PWB-based multichip modules is the lower thermal expansion coefficient.

The permittivity of low-loss ceramics is relatively constant with frequency. In most ceramics the loss tangent increases as the frequency increases. The loss tangent for many ceramic materials and some polymers obey a quasi-linear dependence with frequency *f*, of the form $\tan\delta = af+b$, where *a* is usually a positive number. However, this dependence is not applicable to all ceramics, for example, aluminum nitride.

2.3. Organic Substrates

Organics (plastics or polymers) are commonly used in packaging materials. Substrate materials for PWB are usually composite organic materials and may be anisotropic. Laminations and woven-glass cloth are usually the cause of dielectric anisotropy. Examples of laminates are fiberglass-epoxy composites (FR-4), high-temperature fiberglass-epoxy composites (FR-5), bismalimide triazine-epoxy, cyanate ester, arimid-epoxy, polyimide-glass and polyimide-quartz. The composites commonly consist of a mixture of plastics, glass, and/or ceramics, together with reinforcing materials. Plastics usually are reinforced with glass fibers or impregnated with glass or ceramics. Typical reinforcing materials used are paper fabric, woven glass cloth, random fiberglass fibers, and aramid fiber cloth. The fabric and fiber weaving have some variability due to manufacturing limitations, and this translates into variability in permittivity.

These polymers all have low ε'_r. Plastics, however, have large coefficients of thermal expansion (CTE) and low mechanical strength. Moreover, the thermal expansion

coefficients have nonlinear temperature dependence. Very low ε'_r can be achieved by introducing porosity, use of low-permittivity materials, or by forming hollow stripline ceramic structures.

Cost is crucial for the widespread acceptance of a specific material. In PWB applications, epoxy-glass, such as FR-4, is the least expensive material and, as a consequence, holds a large market share. There are many variations of FR-4 epoxy-glass materials, with a variation in permittivity from 3.8 to 4.6. In increasing order of cost are epoxy-glass, polyimide, polyimide-quartz and polytetrafluoroethylene (PTFE).

2.4. Other Substrates

There are a number of other materials commonly used as substrates. Semiconducting materials such as silicon and gallium arsenide are used as substrates. Silicon is very lossy at low frequencies, whereas gallium arsenide has low loss. A substrate becoming more commonly used is gallium nitride. Anisotropic substrates are single-crystal sapphire, rutile, silicon, and quartz. Sapphire has a high thermal conductivity and very low dielectric loss. Sapphire and quartz are both brittle and difficult to drill and cut. Glasses such as fused silica and borosilicate have low loss and medium values of permittivities. Fused silica and most glasses have poor thermal conductivity. Rutile has a very high permittivity and medium loss.

Chapter 3

Dielectric Measurement Methods for the Permittivity of thin Substrates

3.1. Overview of the Measurement Problem

Dielectric properties of a specimen depend on frequency, homogeneity, anisotropy, temperature and surface roughness. No single technique can accurately characterize all materials over all frequencies and temperatures. Each frequency band and loss regime usually requires a different method.

The measurement of thin materials presents a special challenge in that uncertainty in thickness of the specimen translates into uncertainty in the permittivity. Measurement methods on thin films (thickness<3mm) that depend less on sample thickness and more on transverse dimensions yield more accurate results for ε'_r.

The reentrant cavity, stripline, microstrip, and full-sheet resonance techniques [12] are useful for measurement of the component of permittivity normal to the sample face. However, if the sample is not metalized, measurements with this type of field orientation can suffer from the effects of air gaps between the sample and electrode. The stripline technique has the advantage of easily accommodating PWB materials. It gives reasonable estimates for ε'_r but dubious estimates for ε''_r. Fabry-Perot resonators and open resonators [13] are useful at high frequencies but preparation of the test samples is critical as measurement results highly vary with thickness of the specimen and some skill is required to successfully operate the resonators.

In the radio-frequency and microwave bands, ε'_r is a monotonically decreasing function of increasing frequency. In the radio-frequency and low microwave bands, an increase in ε'_r as the frequency increases is almost always due to a fixture geometrical resonance or other fixture-dependent resonance. For lossy materials ε'_r decreases faster as frequency increases (dispersion) than it does in non-lossy materials. On the other hand ε''_r does not necessarily decrease as frequency increases. It may increase as frequency increases or form a Debye loss peak, rapidly increasing and then decreasing again in a certain frequency range. The loss tangent of most ceramics increases nearly linearly as frequency increases; in such cases, it is possible to extrapolate measurement data from one

frequency range to another. Materials of very low-loss have loss tangents in the microwave spectrum that are nearly frequency independent. In materials with a finite dc conductivity, ε''_r increases at low frequencies as $1/\omega$, where ω is radial frequency.

The real and imaginary parts of the permittivity are related by Kramers-Kronig dispersion relations [14]. A consequence of these relations is that frequency-dependent changes in the real and imaginary parts of the permittivity are correlated.

There are many models used for extracting permittivity. Methods based on Maxwell's equations are single or full-mode models that relate the resonant frequency or transmission and reflection coefficients to functions of the permittivity. These types of models are accurate, but require complicated solutions to Maxwell's equations and can be computationally intensive.

3.2. Measurement Methods

In this section, we overview 3 Maxwell's equations based measurement techniques for thin materials. The strengths and weaknesses of each technique are discussed and compared.

3.2.1. Two-Layer Stripline Method

This method [15] uses a stripline with two different substrates on both sides of the conductor. One of them is referred to as the "standard" substrate, whose dielectric constant and loss tangent are known beforehand; the other is referred to as the "test" substrate, whose dielectric constant is to be determined. The standard substrate is permanently connected to the test setup, but the test substrate can be very easily removed and replaced by another one to be tested, and hence can be very flexible to use for measurement of a large number of substrates.

This technique uses a 50Ω microstrip line on a "standard" substrate, whose dielectric constant is determined using some other accurate measurement technique. The width of the microstrip line and the thickness of the standard substrate must be measured accurately. This standard substrate is connected to a network analyzer by two connectors at the ends of the 50Ω line (see figure 3.1). The substrate under test is etched to remove the cooper on one or both sides, and is cut into a rectangular shape. The dimensions of the test piece need not be of any specific size, and hence the method can be flexibly used for measurement of dielectric constant of any size substrate. It should, however, be greater than about two wavelengths wide, but can be of any suitable length.

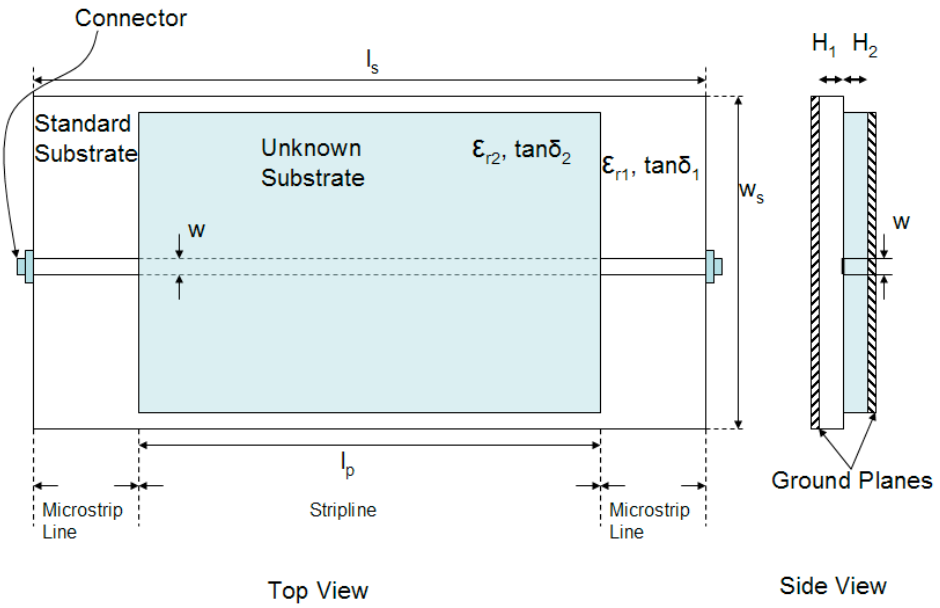

Fig. 3.1: Setup for the two-layer stripline method.

The test substrate is used to cover a portion of the standard microstrip line and is sucked (fig. 3.2) from the bottom to form a stripline structure. The objective is to get rid of any air gap between the standard substrate and the test substrate. The entire transmission structure is then a cascade of microstrip line, stripline, and again microstrip line.

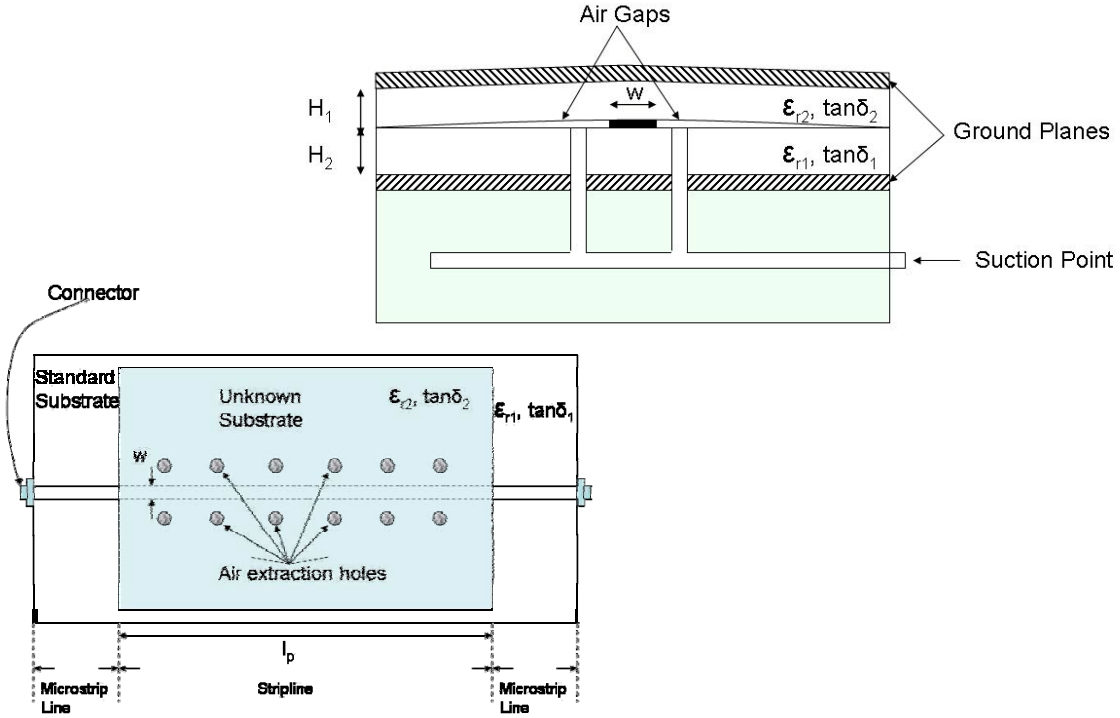

Fig. 3.2: Two-layer stripline method air removal mechanism.

The electrical length of the covered microstrip is different from the bare microstrip line because of the difference of the effective dielectric constants of the bare micrsotrip line

and that of the layered stripline with the standard substrate on one side and the test substrate on the other. The connectors are not changed and do not introduce any error since the discontinuity in the connectors appears identically in both cases. Thus, the electrical length change is due solely to the effective dielectric constant of the stripline under the test piece. The attenuation differs also only due to the stripline under the test piece, so, by measuring the difference, one can infer the loss tangent.

By measurement of the S-parameters of the covered and uncovered transmission line and varying the complex permittivity of the coating material in an Electromagnetic tool the correct values of permittivity and loss tangent of the test substrate can be obtained when simulation results fit the measured values best:

$$\begin{aligned} &\min(\Delta\phi_{meas} - \Delta\phi_{sim}) \\ &\min(\Delta\alpha_{meas} - \Delta\alpha_{sim}) \end{aligned} \tag{3.1}$$

where:

$$\begin{aligned} \Delta\phi &= phase(S_{12})_{\text{cov}} - phase(S_{12})_{un\,\text{cov}} \\ \Delta\alpha &= mag(S_{12})_{\text{cov}} - mag(S_{12})_{un\,\text{cov}} \end{aligned} \tag{3.2}$$

for both measured and simulated results.

A few important points can be mentioned regarding this measuring technique:

1. One side or both of the test substrate can quickly be etched free of copper and made ready for test. The size of the substrate need not be of any particular dimensions.
2. A fixed test setup can be used for a number of different types of substrates of different dielectric constants and different thicknesses.
3. The error introduced in the measurement because of the tolerances of dimensions of the substrate is negligible and also is insensitive to discontinuities in connectors and microstrip-stripline junctions.
4. The method requires the accurate determination of the dielectric constant of the standard substrate.
5. The main problem with this method is avoiding the air gap between the standard and test substrates, and this may determine the final accuracy of the results.
6. To suit a specific application, the system can be optimized for best results, since it is preferable to have the dielectric constant of the substrate under test close to that of the standard to minimize errors due to large discontinuities in the microstrip-stripline junction, which introduces uncertainties (not error) in the measurement process. Similarly, better results will be obtained if the thicknesses of the test and standard substrates are not markedly different.
7. The variation of the dielectric constant over a frequency range can be easily measured. This is done by changing the frequency of the test and using the theoretical data corresponding to that frequency.
8. Extraction of the permittivity and loss tangent using an EM simulation tool to match measured data is computationally intensive.

3.2.2. Two-layer CPW Method

This method [16] is a variation of the two-layer stripline method. It uses a 50Ω coplanar waveguide (CPW) instead of the 50Ω microstrip line but the measurement procedure is the same (see fig. 3.3). The experimental setup is simulated on an Electromagnetic tool and electrical parameters of the test substrate are varied until simulation results fit measurement results best (3.1).

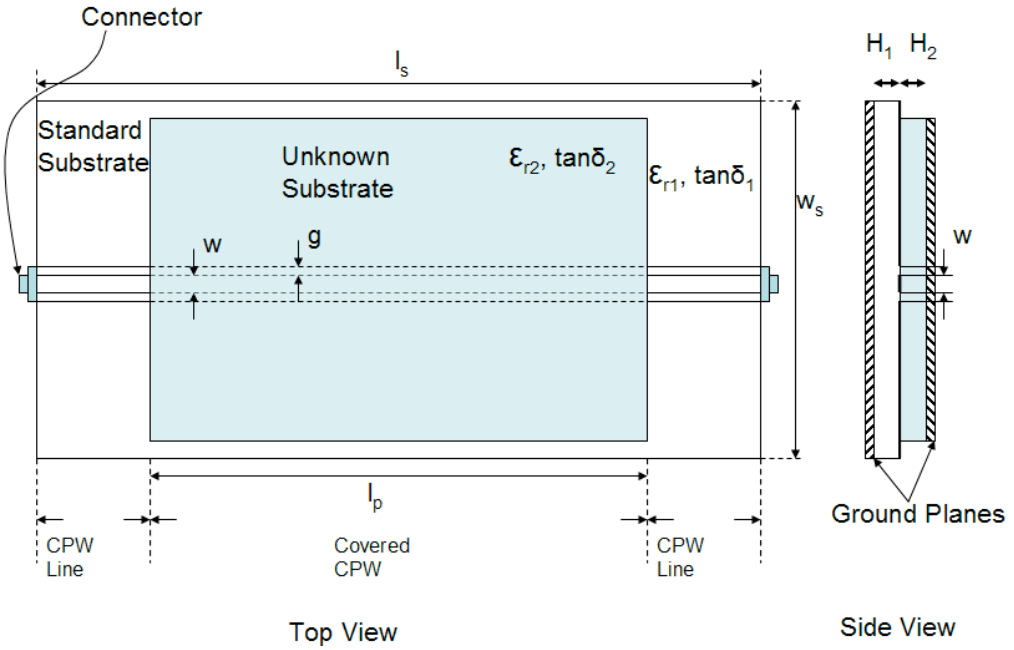

Fig. 3.3: Setup for the two-layer CPW method.

This technique offers the same strengths and weaknesses as the two-layer stripline method, but could yield to more accurate results, as electric fields in a CPW travel mostly in the air and thus, will have a greater interaction with the test substrate. Figure 3.4 shows the electric fields in a CPW and microstrip line.

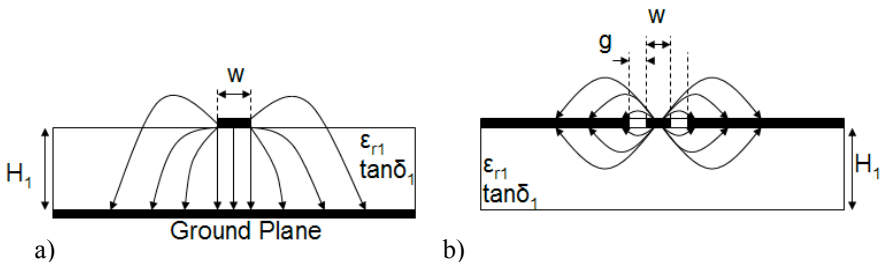

Fig. 3.4: Electric field distributions in a) Microstrip Line; b) CPW line.

3.2.3. Microstrip Ring Resonator

A microstrip ring resonator [17] is a simple transmission line resonator whose geometry is shown in fig. 3.5. The resonator is excited by a transmission line through a capacitive coupling and at certain frequencies, depending on the electrical length (perimeter) of the resonator, a standing wave pattern forms around the circular path of the resonator. The maximum voltage of the standing wave occurs at the exciting point. The resonant frequencies correspond to a condition where the perimeter of the ring is an integer multiple of the guided wavelength, that is:

$$\lambda_g = \frac{\pi d}{n} \quad n = 1,2,3... \tag{3.3}$$

where d is the average diameter of the ring and λg is a function of the microstrip parameters w, H_1, ε_{r1}, $\tan\delta_1$ and ε_{r2} and $\tan\delta_2$ as shown in figure 3.5.

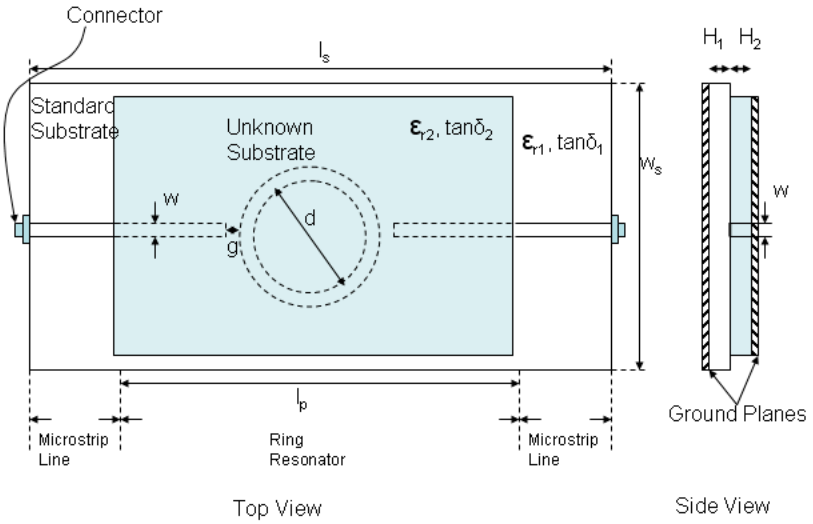

Fig. 3.5: Setup for the Microstrip Ring Resonator Method.

At resonant frequencies there exists a voltage maximum at πd/2 away from the excitation point. By placing a capacitively coupled transmission line at this voltage maximum point, the field in the resonator can be probed to detect the resonant frequencies. Basically, the transmission coefficient S_{12} of the two-port resonator is measured as a function of frequency and the resonant frequencies are identified as frequencies for which $|S_{12}|$ is maximized. Spectral measurement of $|S_{12}|$ can also reveal the quality factor of the resonator which is a measure of power loss in the resonator. The dissipated power in the resonator includes the dielectric loss, the conductor loss and the radiation loss.

The real and imaginary parts of the dielectric constant of the test substrate are to be inferred from the shift in the resonant frequency and the change in the quality factor of the resonator after placing the resonator in contact with the test substrate. An inversion algorithm is provided in [17] to find the solution to this electromagnetic problem. Also simulation of the setup in an EM simulation tool would give accurate results provided that connector losses were accounted for.

This method presents the same strengths and weaknesses as the previous two, except for the fact that as results are not based on the subtraction between loaded and unloaded resonator the method is sensitive to discontinuities in connectors and microstrip-stripline junctions, and will require a more accurate EM simulation model.

Chapter 4

Dielectric Measurement Methods Design and Analysis

4.1. Two-layer Stripline Method

4.1.1. Microstrip Line Design

Using the LineCalc tool, for a given substrate with thickness H_1, permittivity ε_{r1}, loss tangent $tan\delta_1$ and metal thickness T, the width w of the microstrip line that yields to a 50Ω impedance line at 60GHz is easily calculated.

Having into account that if simulation results prove satisfactory the experimental setup will be fabricated, attention has to be put on the election of the substrate material and the dimensions of the microstrip line itself. The design constraints that follow have to be met:

- The substrate material has to be fully electrically characterized at 60GHz.
- The substrate material has to be low loss.
- The width of the microstrip line has to be comparable to the diameter of the V-connectors used (see annex I).

These criteria apply because the method requires a 'known' substrate, low loss materials propagate better the signals and the connector to microstrip transition has to introduce minimal losses.

Some substrate candidates include diverse materials from Rogers Corporation, the only company providing permittivity data up to 50GHz. Our choice is in favor of their RT/d5880 high frequency material, with the lowest loss tangent at 50GHz and excellent electrical stability over frequency that permits interpolation to 60GHz. Figure 4.1 illustrates the permittivity and loss tangent versus frequency data provided by Rogers.

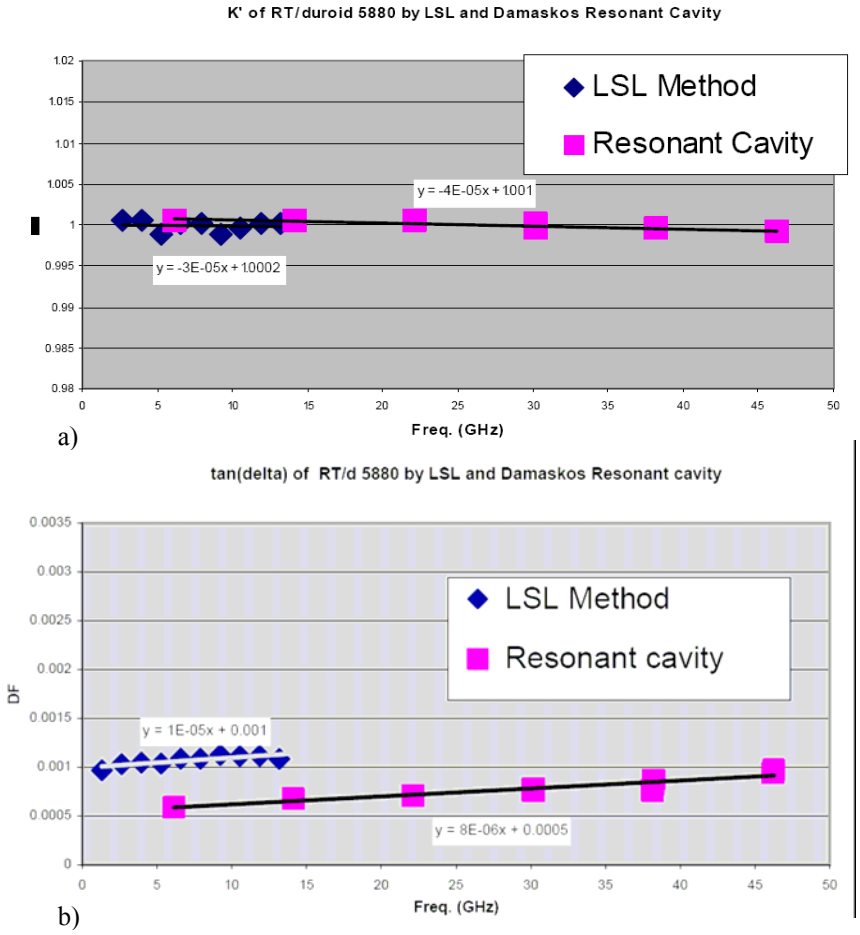

Fig. 4.1: RT/d5880 dielectric measurement data provided by Rogers Corporation a) Permittivity; b) Loss tangent

Considering that the pin diameter of the V-connectors used is 240um, the substrate thickness has been chosen to be 127um because it leads to a microstrip line width w=376.4um, facilitating the transition. Table 4.1 summarizes the design parameters:

Material	RT/d 5880
ε_{r1}	2.195
$tan\delta_1$	0.001
H_1	127um
w	376.4um
T	17um

Table 4.1: Microstrip line design parameters.

Design parameters have then been exported to the EM simulation tool HFSS, from Ansoft Corporation, for simulation of the two-layer stripline problem.

4.1.2. Optimization of the Simulation Design

Simulation of the setup with dimensions equal or close to the ones an experimental setup should have requires an impracticably large number of tetrahedral and takes a substantial amount of memory resources and time to simulate. Efforts to optimize the simulation time by minimizing the setup simulation dimensions while keeping the same performance as with the real setup yield to a 50% reduction in computation time.

Figure 4.2 shows the insertion losses and phase shift for a 50Ω microstrip line for various w_s lengths. It can be concluded that substrate widths greater or equal to 20mm yield to the same results, being thus this dimension a candidate to minimization.

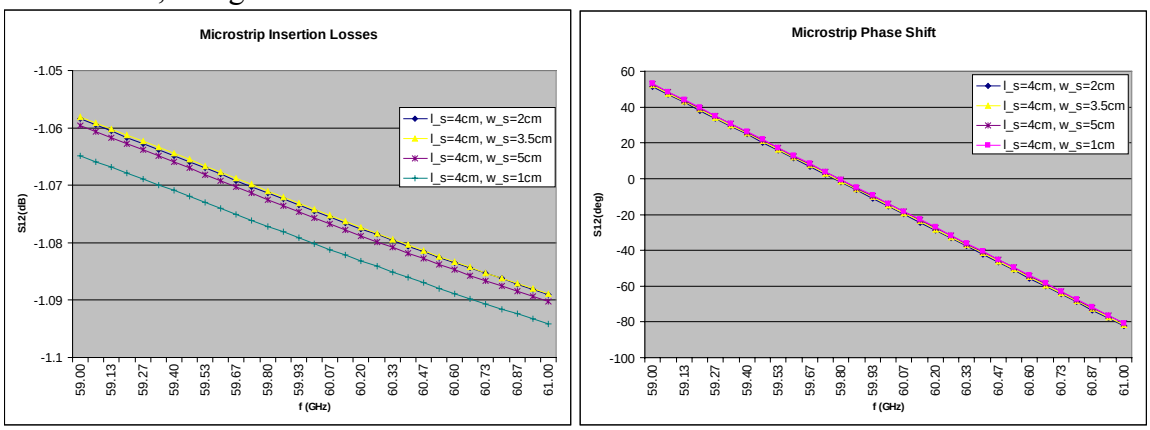

Fig. 4.2: Microstrip insertion losses and phase shift for different substrate widths.

For w_s to be effectively optimized, we also have to prove that simulation results of the two-layer method are not altered when changing its value. The S_{12} loss and phase increase with respect to the uncovered microstrip line when an unmetalized cover with l=2.5cm of an arbitrary material is put on top of the line are plotted on figure 4.3. No significant differences are observed between the 4 simulations.

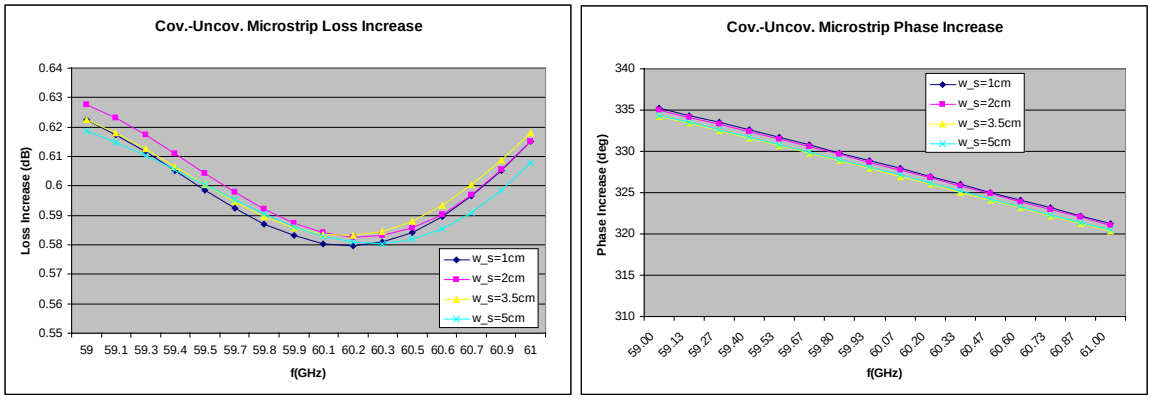

Fig. 4.3: Loss and Phase increase due to an arbitrary unmetalized test substrate for different substrate widths.

Optimization of the l_s dimension can also have a great impact on the simulation time. Tough the length of the test substrate (4cm by design) cannot be minimized because we

need to directly correlate simulation results with experimental results, the length of the microstrip line can be reduced close to 4cm. Figure 4.5 shows simulation results for different values of l_s. The minimum microstrip line length for which results keep unaltered is 5.5cm. Under this length, the microstrip to stripline transition is too close to the ports.

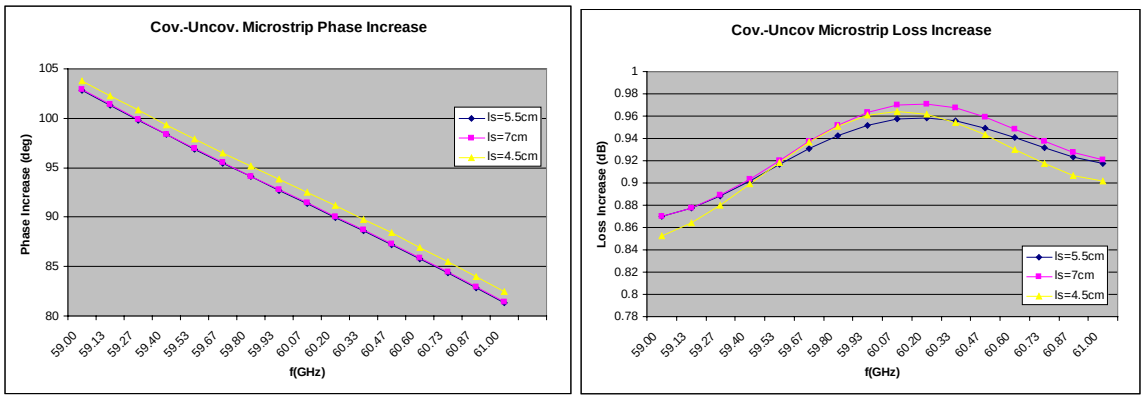

Fig. 4.4: Loss and Phase increase due to an arbitrary unmetalized test substrate for different microstrip line lengths.

In sight of these results, from now on, the simulation width w_s is going to be set to 10mm and the length l_s to 55mm.

4.1.3. Two-Layer Stripline HFSS Simulation Results

With simulation parameters optimized, we will proceed to analyze the accuracy of the method in terms of permittivity and loss tangent resolution, by simulation of different experiments.

Fig. 4.5 shows the phase increase $\Delta\theta_{sim}$ from the covered microstrip versus the same uncovered microstrip line for different test substrate materials. Test substrates are unmetalized, have a loss tangent *tanδ=0.001* and permittivities shown in the graphs. It is observed that the phase difference decreases linearly with the permittivity, with 23deg. deviation each 0.1 permittivity increase. This means that for permittivity increases of 1.5, the same $\Delta\theta_{sim}$ will be found (see graph for perm=3.2 and perm=4.7). Knowingly that permittivity is much more stable over frequency than the loss tangent for most materials, this feature does not limit our capacity to correctly predict this characteristic.

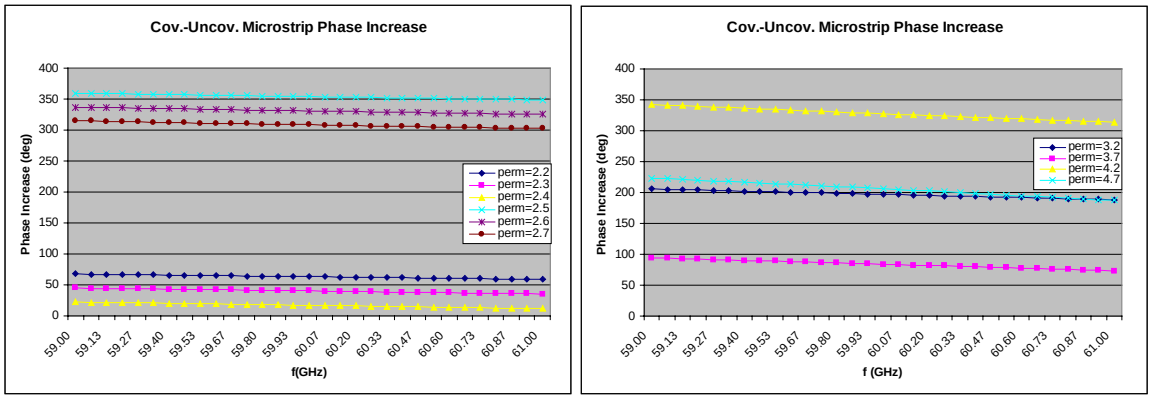

Fig. 4.5: Two-layer Stripline $\Delta\theta_{sim}$ versus permittivity for unmetalized test substrates.

Figure 4.6 plots $\Delta\theta_{sim}$ for unmetalized test substrates with a permittivity of $\varepsilon_r=2.2$ and increasing loss tangents. It is observed that the loss tangent has little or no effect on the detected phase deviation, except for loss tangents above 0.1, when losses are so high that affect the propagation speed of the signal. These results, however, cannot be extrapolated to materials with higher dielectric constants, because, as it will be observed later, changes on low loss tangents also affect the phase. Thus, $tan\delta$ and ε_r have to be simultaneously determined.

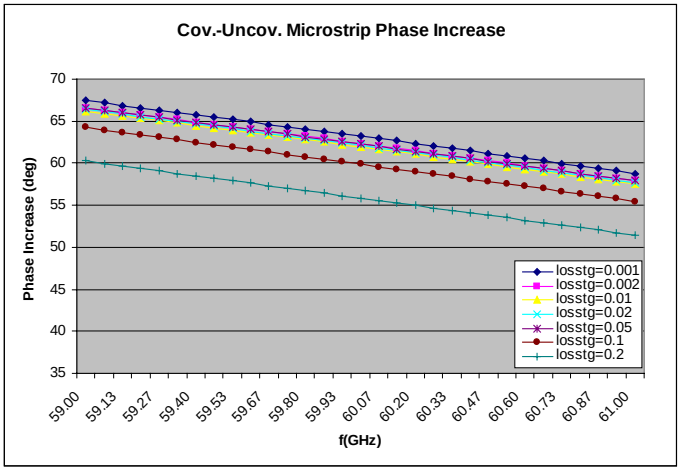

Fig. 4.6: Two-layer Stripline $\Delta\theta_{sim}$ versus loss tangent for unmetalized test substrates.

Calculation of $\Delta\alpha_{sim}$ for unmetalized test substrates with $tan\delta=0.001$ and increasing permittivities shown in fig. 4.7, could lead to the conclusion that firstly, the permittivity of a material has to be found and afterwards, the loss tangent can be inferred as an increase in permittivity affects the losses, but an increase in the loss tangent does not affect the phase for low loss materials. This, however, does not apply for higher permittivity materials, given that losses increase with both permittivity and loss tangent and will be high even for low loss tangent materials, making phase change. Thus, the Kramers-Kronig dispersion relation is verified, and both, the real and imaginary parts of permittivity have to be determined altogether by simulation.

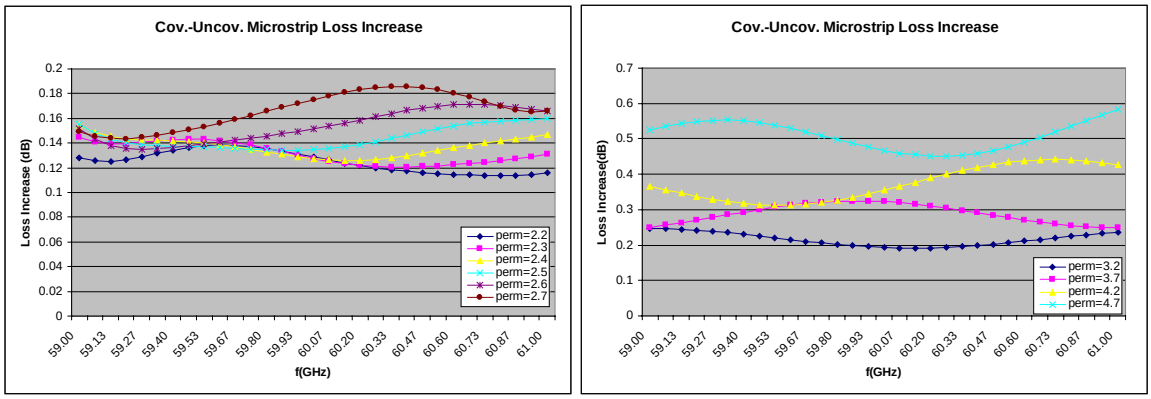

Fig. 4.7: Two-layer Stripline $\Delta\alpha_{sim}$ versus permittivity for unmetalized test substrates.

Figure 4.8 shows $\Delta\alpha_{sim}$ for unmetalized test substrates with a permittivity of $\varepsilon_r=2.2$ and increasing loss tangents. Losses increase linearly with *tanδ*, with approximately 0.8dB for each 0.01 loss tangent increase. Loss tangents above 0.2 will be difficult to accurately determine, because the received signal will be too low. Low loss tangents can also be difficult to determine, because of the small losses introduced.

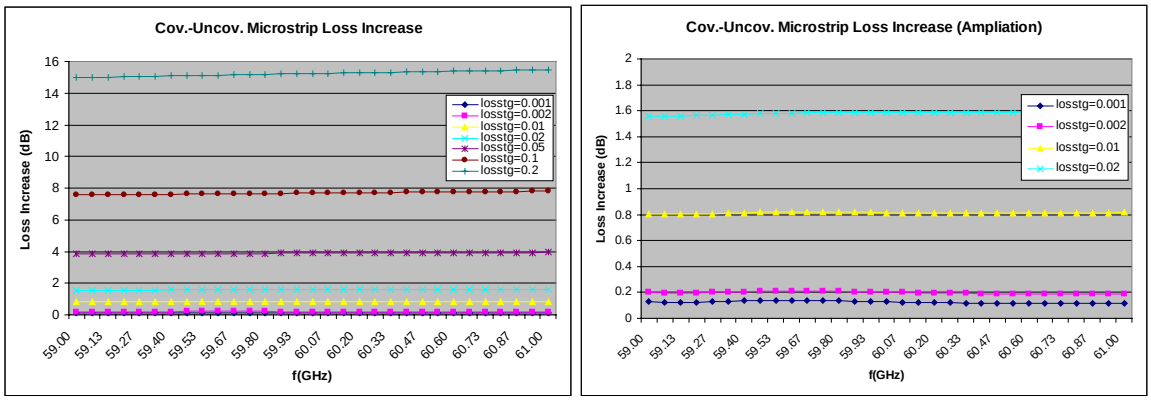

Fig. 4.8: Two-layer Stripline $\Delta\alpha_{sim}$ versus loss tangent for unmetalized test substrates.

With this method, permittivities can be resolved with an accuracy of 0.1 or better and loss tangents with an accuracy of 0.001. So, given this results, that validate the method, we will consider fabrication of a prototype to conduct experimental measurements.

In subsequent paragraphs, the previous study is conducted for the case when the test substrate is top metalized. The objective is to determine if this feature is helpful in obtaining better results. Fig. 4.9 represents the phase increase $\Delta\theta_{sim}$ for metalized test substrates with *tanδ=0.001* and permittivities shown in the graphs. The phase difference decreases linearly with the permittivity, but starts to behave strangely for high permittivities. This is because the test substrate over the microstrip acts as a capacitor.

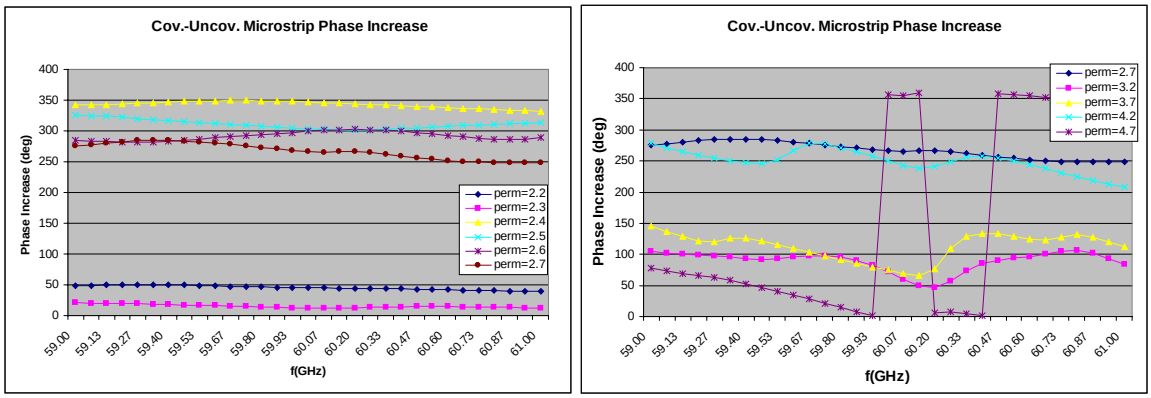

Fig. 4.9: Two-layer Stripline $\Delta\theta_{sim}$ versus permittivity for metalized test substrates.

Figure 4.10 plots $\Delta\theta_{sim}$ for metalized test substrates with a permittivity of $\varepsilon_r=2.2$ and increasing loss tangents. It is observed that the loss tangent has little or no effect on the detected phase deviation, except for loss tangents above 0.05.

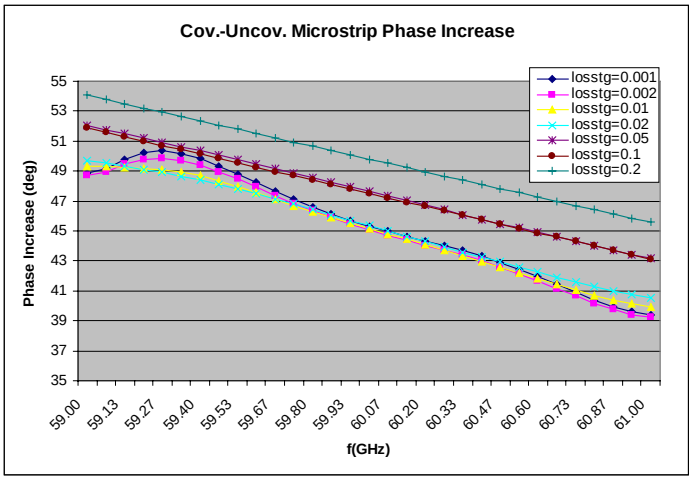

Fig. 4.10: Two-layer Stripline $\Delta\theta_{sim}$ versus loss tangent for metalized test substrates.

Calculus of $\Delta\alpha_{sim}$ for metalized test substrates with $tan\delta=0.001$ and increasing permittivities shown in fig. 4.11, corroborates results from fig. 4.9. The top metallization makes the stripline appear like a capacitor, and introduces uncontrolled losses.

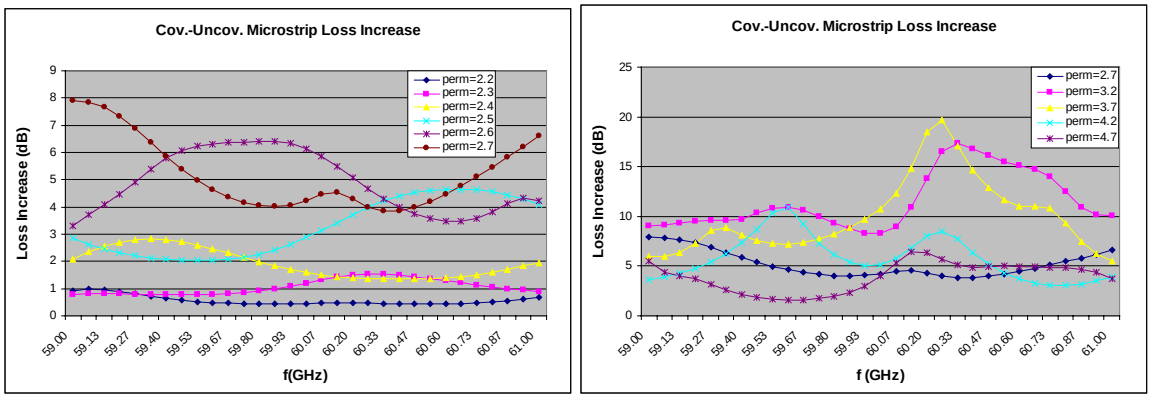

Fig. 4.11: Two-layer Stripline $\Delta\alpha_{sim}$ versus permittivity for metalized test substrates.

Figure 4.12 shows $\Delta\alpha_{sim}$ for metalized test substrates with a permittivity of $\varepsilon_r=2.2$ and increasing loss tangents. Again losses increase linearly with $tan\delta$, and accentuate differences between low loss materials. Loss tangents above 0.2 will be difficult to accurately determine.

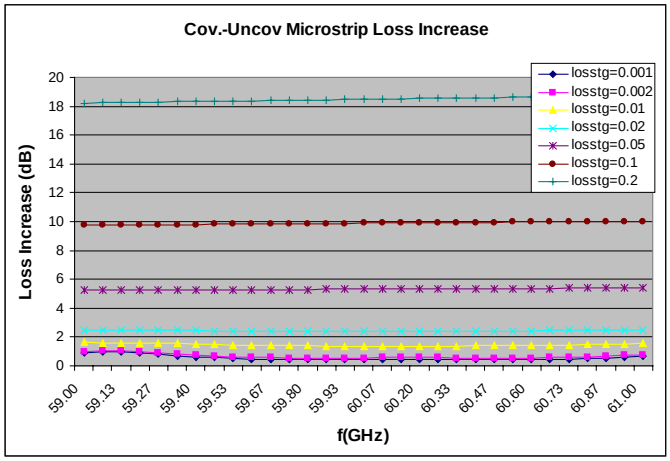

Fig. 4.12: Two-layer Stripline $\Delta\alpha_{sim}$ versus loss tangent for unmetalized test substrates.

We can conclude that the test substrate top metallization will generally not aid us in the dielectric determination. The only case that reports a benefit is for low permittivity materials with very low loss tangents, were loss differences for small loss tangent increases are maximized. In the other cases, especially for higher permittivities, it is going to seriously limit our capability of correctly extracting the test substrates' electrical parameters, so metalized substrates shouldn't be used.

4.2. Two-layer CPW method

4.2.1. CPW Line Design

Using the LineCalc tool, for a given substrate with thickness H_1, permittivity ε_{r1}, loss tangent $tan\delta_1$ and metal thickness T, the width w and gap g of a CPW line that yield to a 50Ω impedance line at 60GHz can easily be found. However, things complicate when you have to take into account the following design criteria for the experiment to be fabricated:

- The substrate material has to be fully electrically characterized at 60GHz.
- The substrate material has to be low loss.
- The minimum machinable gap width g is 76.2um (3mils).
- A Grounded CPW (GCPW) is preferable, to avoid interaction of the electric fields with the surface where the CPW lies, but excitation of the microstrip mode should be avoided.
- The gap to gap distance has to be below 500um to allow probing.

In GCPW lines, the condition of small ground-to-ground (2g+w) spacing compared to substrate thickness is necessary to avoid the excitation of the microstrip mode, and to minimize the deviation of the CPW mode from the "odd" mode of the ideal line. Figure 4.13 shows that to achieve a 50Ω GCPW, for the chosen substrate material RT/d5880 and minimum gap width, the condition is not met for any of the substrate thicknesses available.

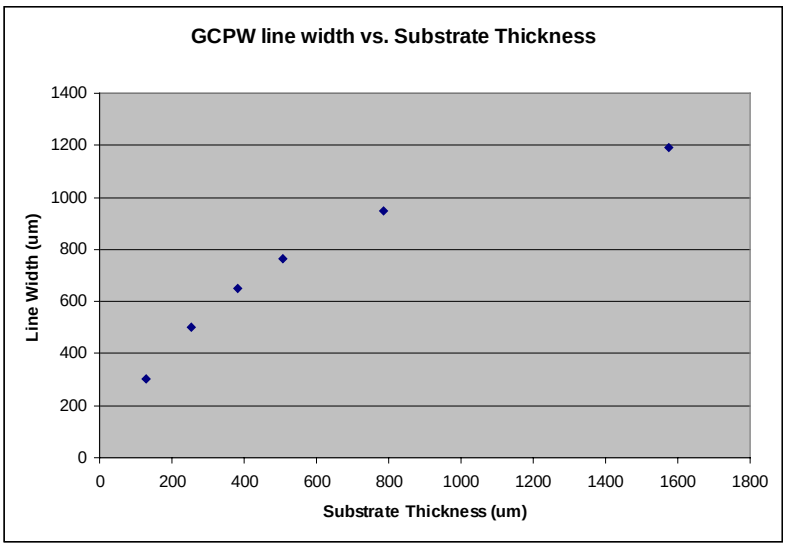

Fig. 4.13: 50Ω GCPW line width versus substrate thickness for RT/d5880 and 76.2um gap width g.

Thus, another material with low loss and higher permittivity has to be considered. The R03006 from Rogers Corporation, with a permittivity of 6.15, loss tangent of 0.0028 at 50GHz and excellent electrical stability over frequency is a good candidate. Figure 4.14 plots the 50Ω GCPW line width versus the available substrate thicknesses. R03006 substrate materials with thicknesses above 1000um satisfy the design criteria, at the expenses of having increased losses compared to RT/d5880.

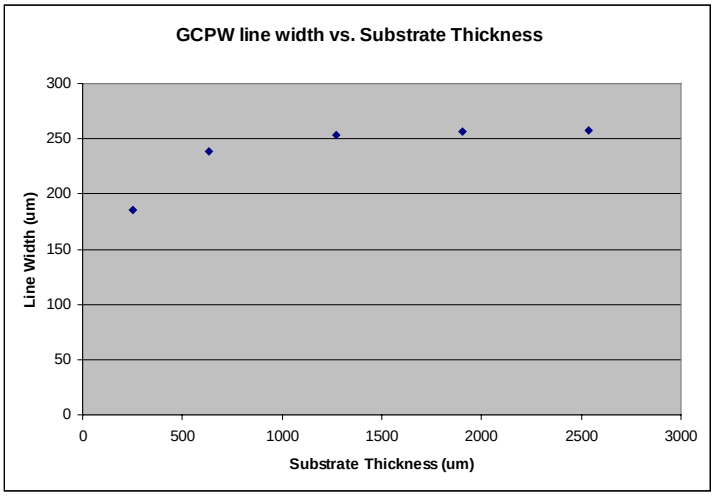

Fig. 4.14: 50Ω GCPW line width versus substrate thickness for R03006 and 76.2um gap width g.

Table 4.2 summarizes the design parameters:

Material	R03006
ε_{r1}	6.15
$tan\delta_1$	0.0029
H_1	1.57mm
w	255.6um
T	17um
g	76.2um

Table 4.2: CPW design parameters.

4.2.2. Two-Layer CPW HFSS Simulation Results

Given the electrical dimensions of the GCPW line and the HFSS waveguide port restrictions [18] that both state a port should have the minimum dimensions depicted in 4.15 and be inferior to λ/2 (2.5mm at 60GHz) in length and width for a correct simulation, we have not been able to simulate a GCPW line and obtain coherent results because we cannot accomplish all the criteria at once. Furthermore, the use of lumped ports has resulted unsuccessful given that return losses proved the line to be unmatched at 50Ω.

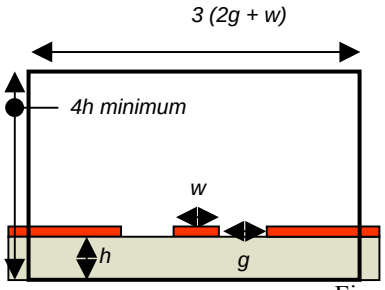

Fig. 4.15: GCPW Waveguide Port dimensions.

The use of a waveguide port with reduced dimensions and located like if we had a CPW line and artificial grounding of the CPW to the back metallization using a series of vias has proved propagation of the CPW mode, but also of higher order modes. No agreement between simulation results for different length lines in the losses/length prevents us from concluding that this approach models the GCPW correctly. Furthermore, simulation using other EM tools, such as IE3D do not agree with HFSS results.

Given the simulation problems stated before, a thorough analysis of the method cannot be conducted. Moreover, the fact that EM simulations are required to extract permittivity data from measurements, we will postpone the design of a prototype until a solution can be found.

4.3. Microstrip Ring Resonator

4.3.1. Ring Resonator Design

Using the LineCalc tool, for a given substrate with thickness H_1, permittivity ε_{r1}, loss tangent $tan\delta_1$ and metal thickness T, the width w of the 60GHz 50Ω microstrip line that couples to the ring resonator has been found. The same design constraints exposed in 4.1.1 in choosing the material and dimensions have been applied, as eventually the experiment will be fabricated. Width of the microstrip ring has been chosen to be equal to w, and the mean radius r of the ring 5mm, a multiple of the free space wavelength at 60GHz. The gap distance g between the microstrip and the ring has been optimized a posteriori, with HFSS. Table 4.3 summarizes the critical design parameters:

Material	RT/d 5880
H1	127um
r	5mm
w	376.4um
T	17um
g	200um

Table 4.3: Ring Resonator design parameters.

Design parameters have then been exported to the EM simulation tool HFSS, for simulation of the microstrip ring resonator problem.

4.3.2. Microstrip Ring Resonator Simulation Results

Figure 4.16 shows the simulated S_{12} parameter for the structure of figure 3.5, with dimensions from table 4.3. Resonances are found at 55.5, 62.5 and 69.4GHz. Calculus of the effective permittivity of the microstrip line using LineCalc gives us an ε_{eff}=1.884, which results in a wavelength at 55.5GHz of λ_g=3.9mm and at 62.5GHz of λ_g=3.5mm. Applying (3.3) we find n to be 7.977 and 8.984 at 55.5 and 62.5GHz respectively. These results corroborate the correctness of the simulation, as resonant frequencies appear for each integer n.

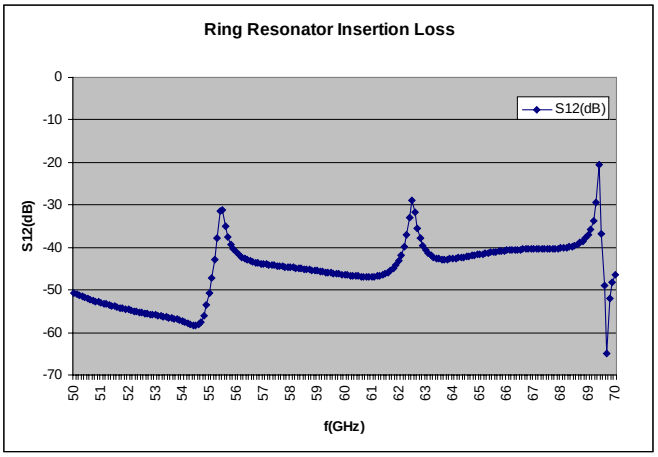

Fig. 4.16: Uncovered Ring Resonator insertion losses.

However, tough the ring is resonant, coupling is very weak (with resonances below 30dB) which implies that the capacity of measuring lossy materials is going to be very limited. To increase coupling between the microstrip line and the ring resonator the design of picture 4.17 is proposed. Simulation results of figure 4.18 corroborate the coupling improvement and ensure higher capacity for loss tangent measurement.

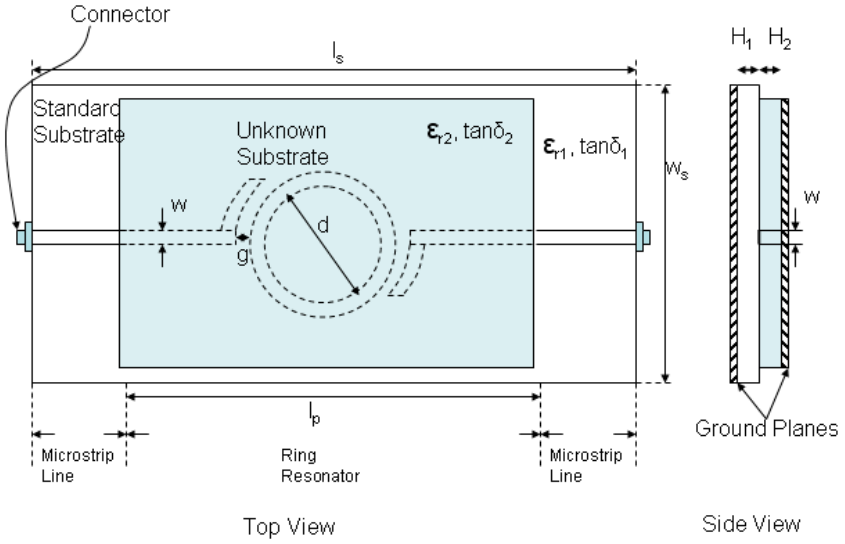

Fig. 4.17: Setup for the improved Microstrip Ring Resonator.

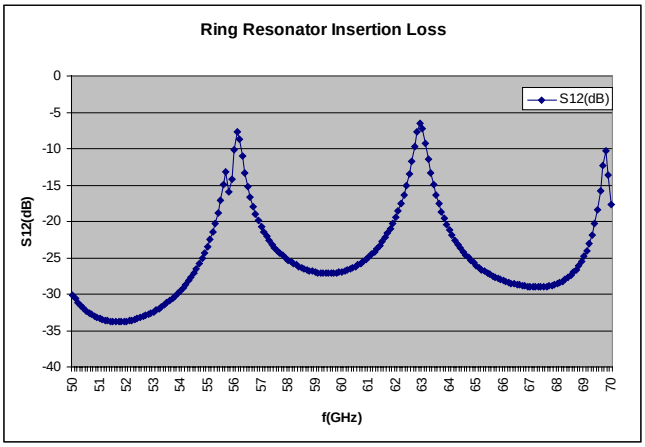

Fig. 4.18: Uncovered improved ring resonator insertion losses.

To determine the capability of the method to distinguish between two materials with different electric characteristics a permittivity and a loss tangent sweep for a fictitious test substrate has been performed. Figure 4.19 plots the resonator insertion losses versus permittivity, for a material with a loss tangent *tanδ=0.001*. For increasing permittivities the resonant frequency shifts down the spectrum, with a shift proportional to the permittivity increase. This is in accordance with what can be inferred from (3.3). The minimum detectable increment in permittivity is 0.1. Figure 4.20 illustrates the resonator insertion losses versus loss tangent, for a material with a permittivity $\varepsilon_r=2.2$. The quality factor is inversely proportional to the loss tangent and allows for its measurement with an

accuracy of 0.001. For loss tangents exceeding 0.1, it becomes practically impossible to accurately measure the resonant frequency and the quality factor of the loaded ring.

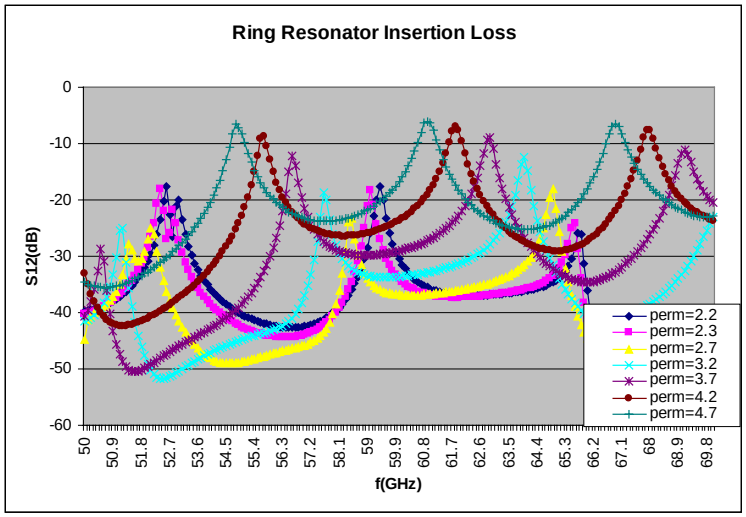

Fig. 4.19: Ring Resonator insertion losses as a function of permittivity.

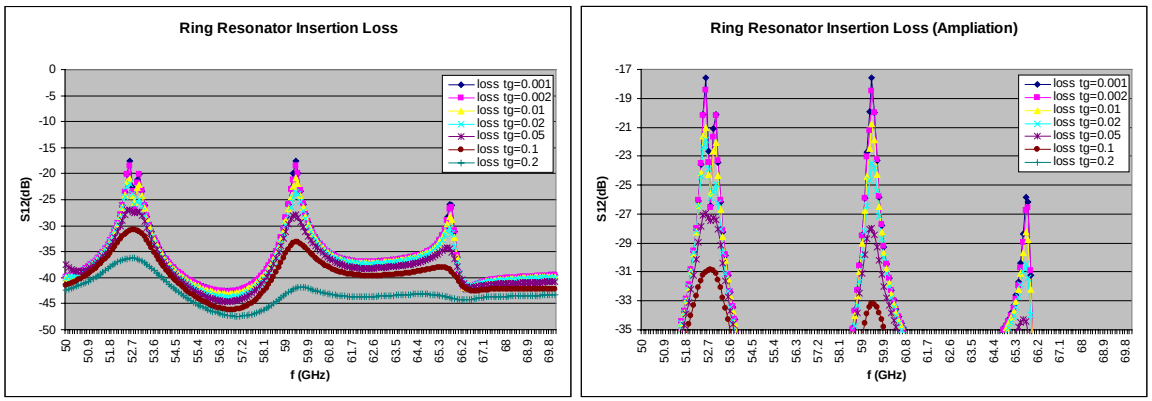

Fig. 4.20: Ring Resonator insertion losses as a function of loss tangent.

Another variant of this method is the distributed coupling ring resonator, whose setup is illustrated in picture 4.21. The strength of this variant is that the test substrate does not have to cover part of the microstrip line, avoiding interaction of the microstrip line with the test substrate.

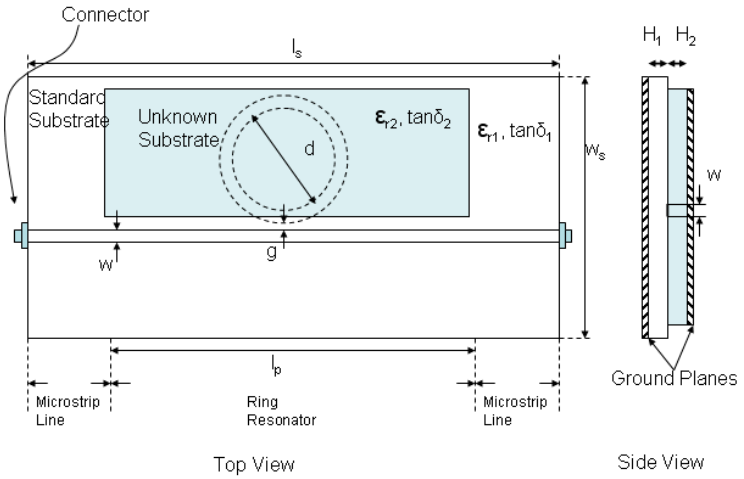

Fig. 4.21: Setup for the distributed coupling Microstrip Ring Resonator.

Figure 4.22 shows the insertion losses for the uncovered distributed coupling ring resonator. The resonant frequencies are identified as frequencies for which $|S_{12}|$ is minimized and correspond to the same frequencies of figure 4.18.

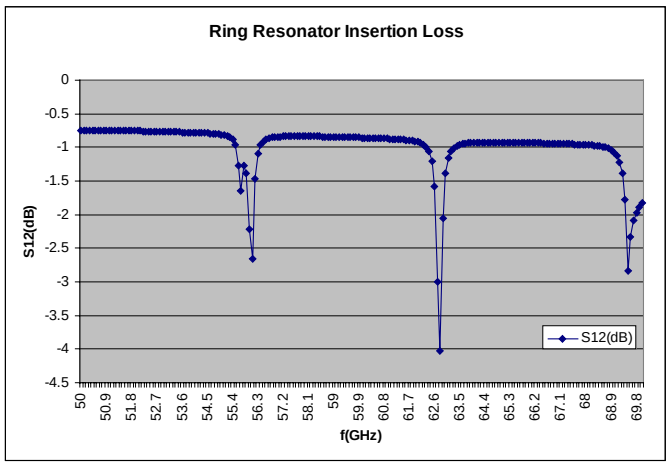

Fig. 4.22: Uncovered distributed coupling ring resonator insertion losses.

Figure 4.23 plots the resonator insertion losses versus permittivity, for a material with a loss tangent *tanδ=0.001*. For increasing permittivities the resonant frequency shifts down the spectrum, with a shift proportional to the permittivity increase, as in the previous approach. However, a second resonance close the first one appears. This is because the ring is both electrically and magnetically coupled, having each its resonance frequency. The minimum detectable increment in permittivity is 0.1. Figure 4.24 illustrates the resonator insertion losses versus loss tangent, for a material with a permittivity $\varepsilon_r=2.2$. The quality factor is inversely proportional to the loss tangent and allows for its measurement with an accuracy of 0.001. For loss tangents exceeding 0.1, it becomes practically impossible to accurately measure the resonant frequency and the quality factor of the loaded ring. On sight of these results we can conclude that this method does not outperform the previous one.

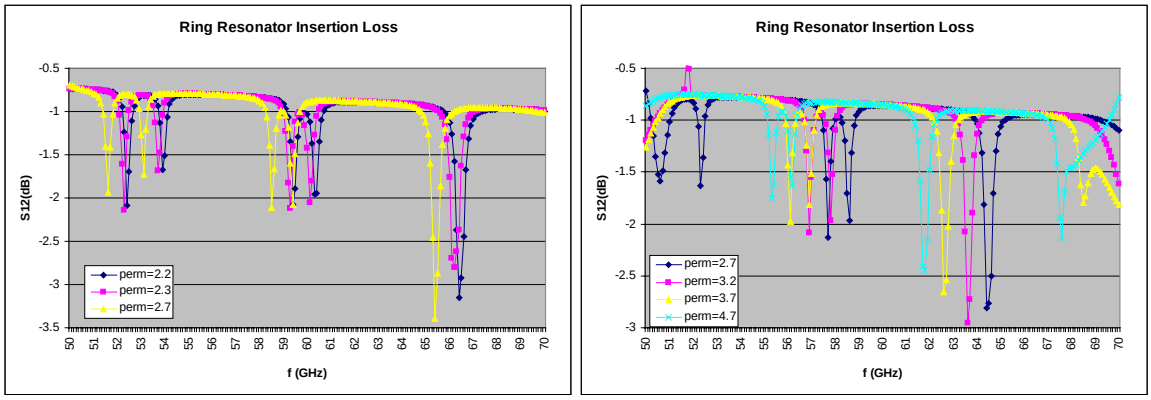

Fig. 4.23: Distributed Coupling Ring Resonator insertion losses as a function of permittivity.

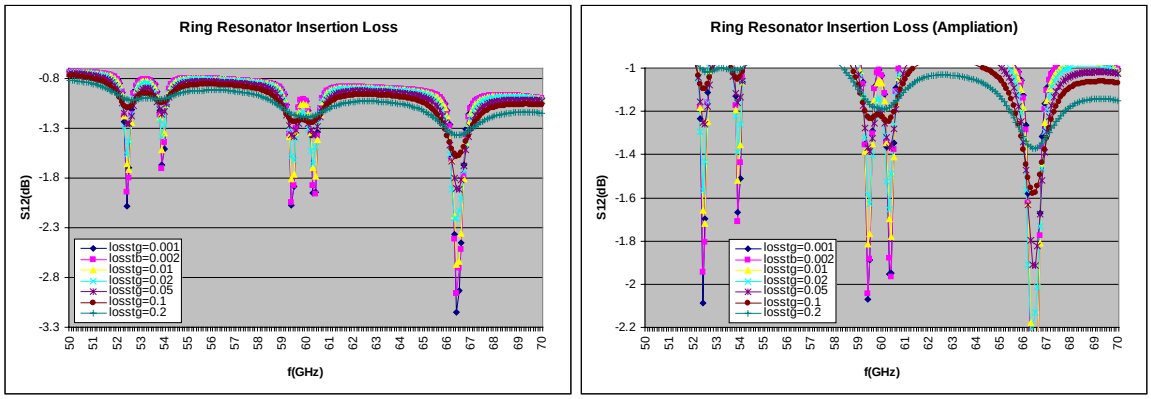

Fig. 4.24: Distributed Coupling Ring Resonator insertion losses as a function of loss tangent.

Chapter 5

Two-Layer Stripline Experimental Dielectric Measurement Results

In this section, the design considerations for the development of a prototype for permittivity measurements using the two-layer stripline method and some experimental results are given.

5.1. Design of the prototype

The design as shown in pictures 3.1 and 3.2 consists on a microstrip line over a perforated substrate with a vacuum chamber. At the ends of the microstrip line connectors are attached. The designed prototype consists on 3 different pieces referred to as:

- RF Test Fixture Part A
- RF Test Fixture Part B
- RF Test Fixture Part C

5.1.1. RF Test Fixture Part A

Contains the microstrip line, air extraction holes and vacuum chamber. Consists on a 5mils duroid RT/d5880 substrate over a 1/4" brass piece. Copper on the top side of the duroid is etched to build the microstrip line. The brass piece acts as its ground. The material and microstrip dimensions have been chosen according to 4.1 and the microstrip line has been gold plated to avoid oxidation.

Small holes are drilled from top to bottom of the piece, in a linear fashion along the sides of the microstrip as can be seen in picture 5.1 and a cavity is drilled from the bottom of the piece into the brass for the vacuum chamber. A hole from one of the sides of the brass onto the vacuum cavity is drilled to allow connection of a vacuum pump.

Mounting holes to allow attachment to parts B and C are drilled both on the bottom and sides of the brass piece and pins included to secure alignment with part C. AutoCad design drawings can be found in Annex II.

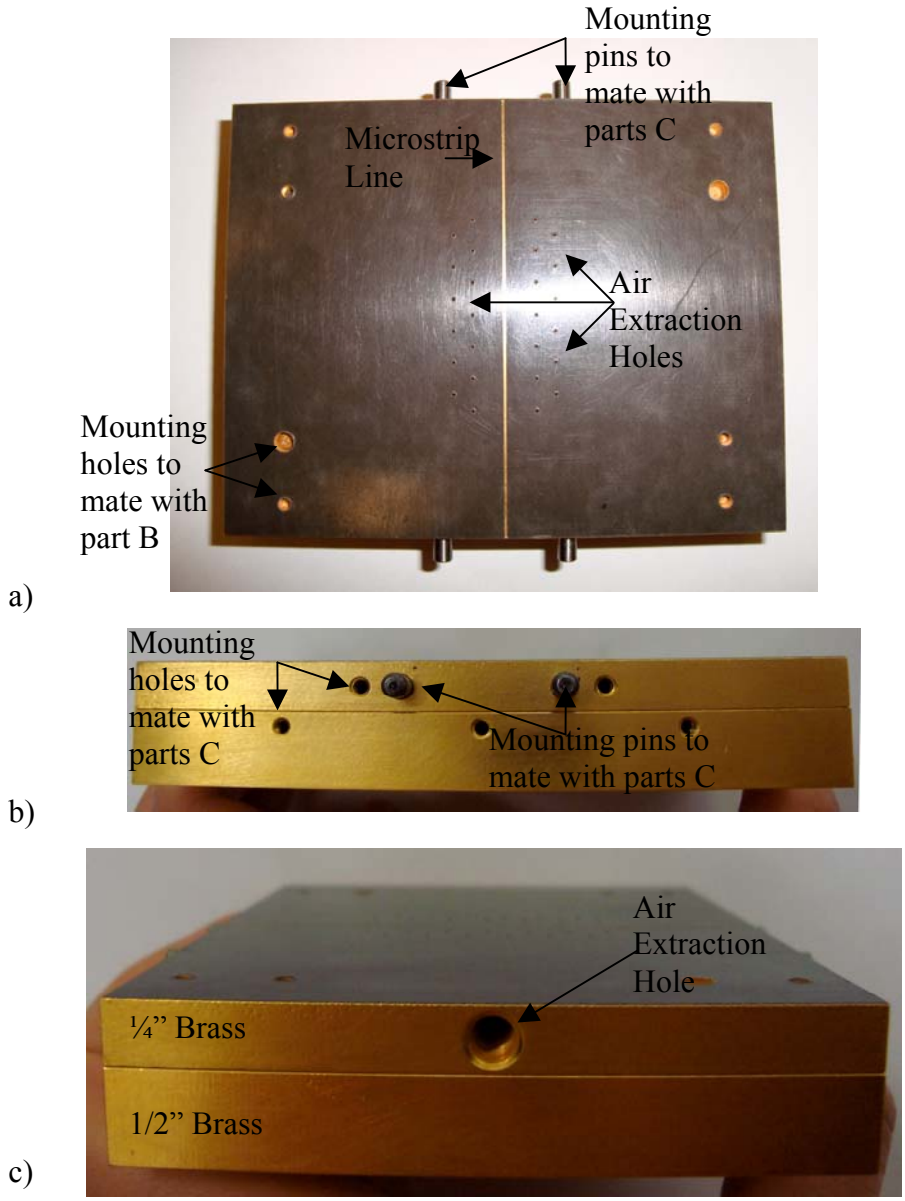

Fig. 5.1: RF Test Fixture Part A a) Top View; b) Connector Side View; c) Air extraction side view.

5.1.2. RF Test Fixture Part B

The only purpose of this part is to seal the vacuum chamber of Part A, thus a very smooth surface finish on both the bottom side of Part A and the mating side of Part B is required. It consists on a 1/2" brass piece.

Mounting holes matching with pieces A and C can be viewed on picture 5.1.

5.1.3. RF Test Fixture Part C

It allocates the V-connectors that allow interconnection between 1.85mm coaxial cables and the microstrip line. Figure 5.2 depicts the sparkplug assembly. The lateral piece (our part C) holds the center conductor and glass bead. Machining dimensions for the mounting hole required for installation of the microstrip to V female sparkplug connector V102F are critical and can be found in annex I.

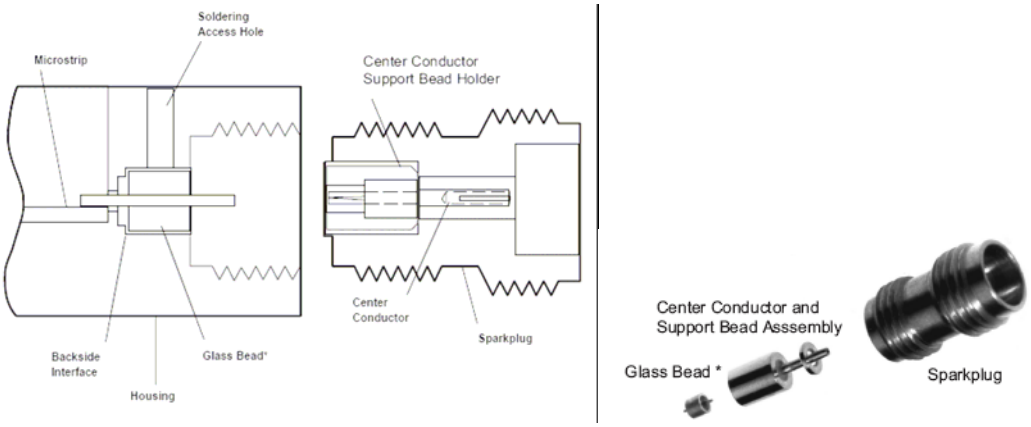

Fig. 5.2: Sparkplug assembly and unassembled V102F Sparkplug connector.

A series of long mounting holes have been drilled in the piece, to allow precise mating with pieces A and B and ensure good contact between the glass bead and the microstrip line. In picture 5.3 we can appreciate all this features.

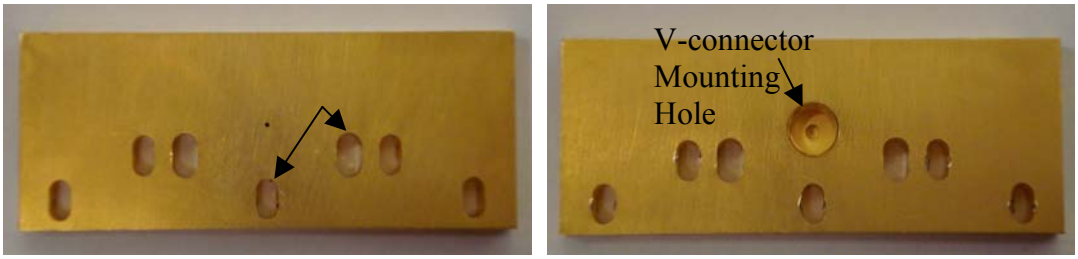

Fig. 5.3: RF Test Fixture Part C.

5.1.4. Complete RF Test Fixture

To start, the V102F flange mount connectors have to be installed. Firstly, the center conductor and support bead assembly are inserted on the V-connector mounting hole. Then, the V102F outer conductor has to be installed onto its housing making sure that the center conductor mates properly with V102F center pin, securing it with two screws.

Finally, pieces A, B and C, one at each end of the microstrip line, are assembled together using the guide pins to position the connectors at the right height above the microstrip line. Some silver conductive epoxy is deposited on the glass bead to connect it to the microstrip line. Pictures of the prototype can be seen in figure 5.4.

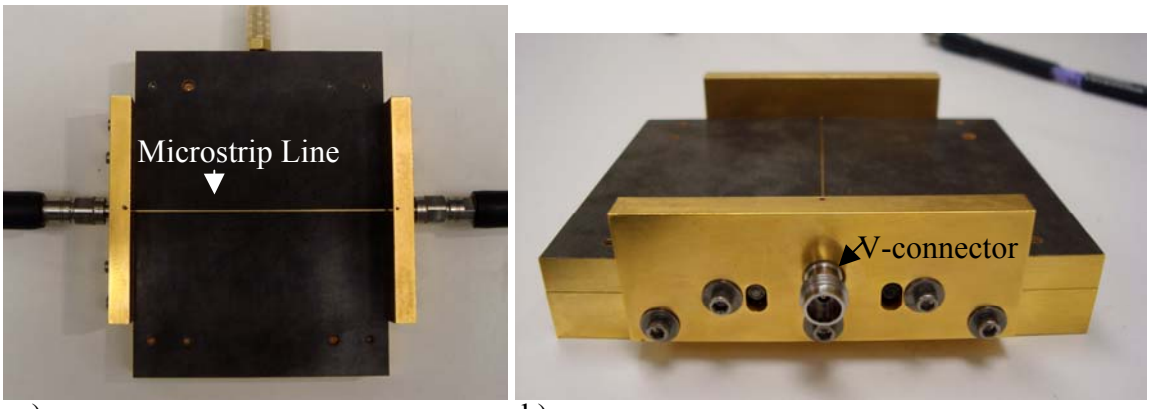

a) b)

Fig. 5.4: RF Test Fixture, a) Top View; b) Side View.

5.2. Measurement Setup

Dielectric permittivity measurements are made in the frequency domain using the E8361C PNA Network Analyzer from Agilent Technologies. The RF text fixture is connected to the VNA (Vector Network Analyzer) via two 1.85mm coaxial connectors and to a vacuum pump as shown in picture 5.5.

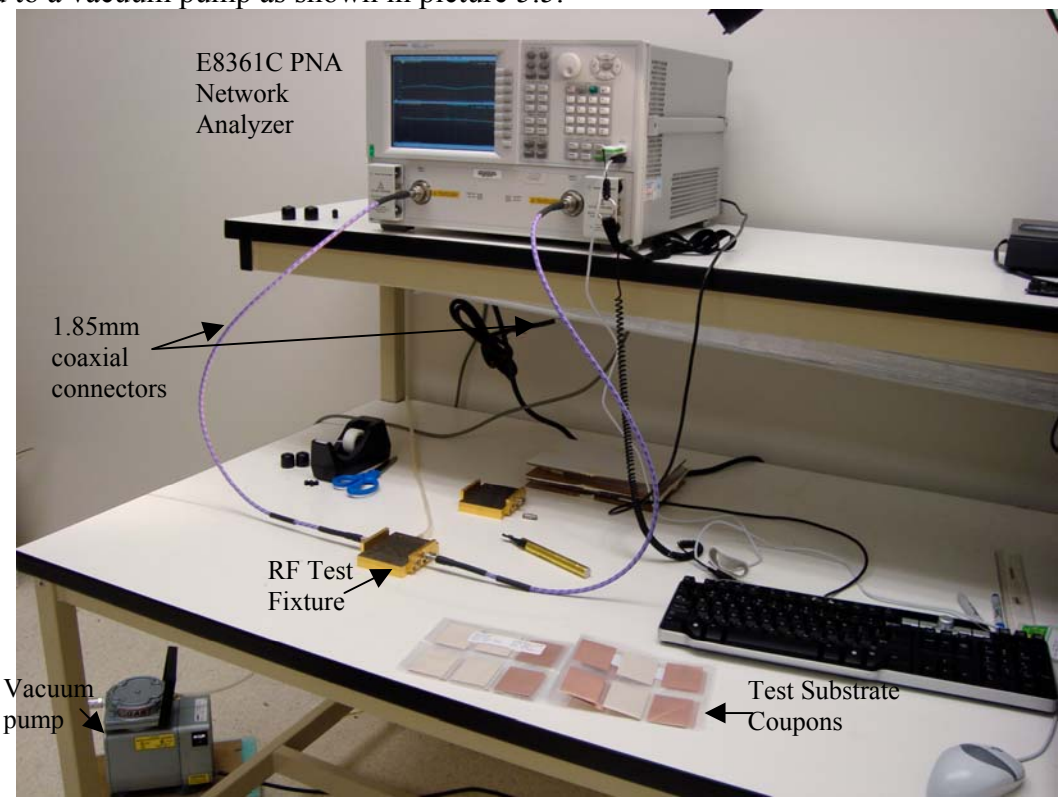

Fig. 5.5: Two-layer Stripline Measurement Setup.

Materials to be tested have been cut in coupons like the ones shown in picture 5.6, with dimensions of 4x5cm. Two coupons without metallization and two coupons with metallization on one side have been processed for each material.

Fig. 5.6: Dielectric test coupons.

S-parameters of the covered microstrip line are measured when coupons are placed on top of the microstrip line as shown in figure 5.7.

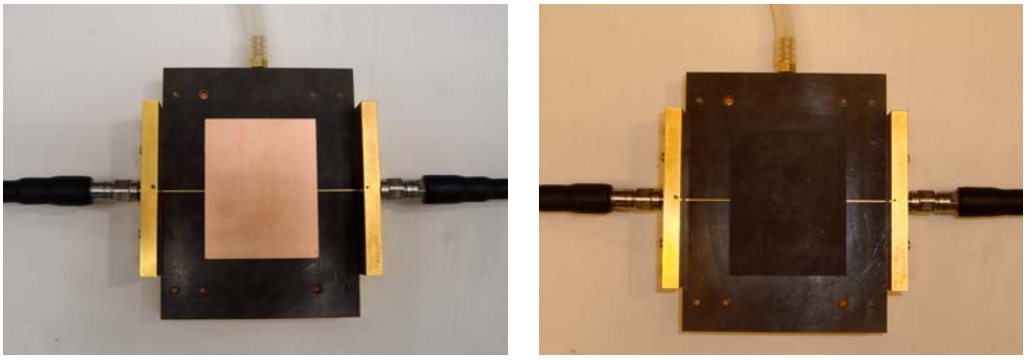

Fig. 5.7: Covered microstrip line measurement.

5.3. Calibration

Prior to start measuring, the VNA and associated cable connections are calibrated. The two-port N4694A Electronic Calibration (ECal) kit from Agilent Technologies is used. To ensure that the network analyzer calibration remains valid during the measurement campaign, at repeated intervals of time, the uncovered microstrip line is measured and results contrasted.

Calibration between the measured and simulated results with HFSS is also required for the applicability of the two-layer stripline method. As the dielectric parameters of the test substrate are inferred from simulation results when they correlate with measurement results, proof of existing correlation must be given for the validity of results.

The calibration method consists on measuring a test sample of the same material of the microstrip line, that is, RT/d5880 and the uncovered microstrip. A simulation with HFSS of the setup is then run, and the two-layer stripline method parameters $\Delta\theta$ and $\Delta\alpha$ extracted both from measurements and simulations. A series of "calibration" simulations are then run on HFSS varying parameters that are susceptible to tolerance errors such as microstrip line width w, substrate height H_1 and metal thickness T, and possible remaining air gap dimensions, until $\Delta\theta_{sim} \approx \Delta\theta_{meas}$ and $\Delta\alpha_{sim} \approx \Delta\alpha_{meas}$.

Fig. 5.8 shows the HFSS calibrated results against the measurement results for the calibration material RT/d5880. Good agreement is achieved in $\Delta\theta$, with simulation results matching the experimental results regression line with less that 1deg. absolute error. Given the low losses of the material and the observed variance with frequency in the measured losses, correlation between simulation and experimental results in $\Delta\alpha$ is not exact. However, simulation results give approximately the mean value of experimental measurements.

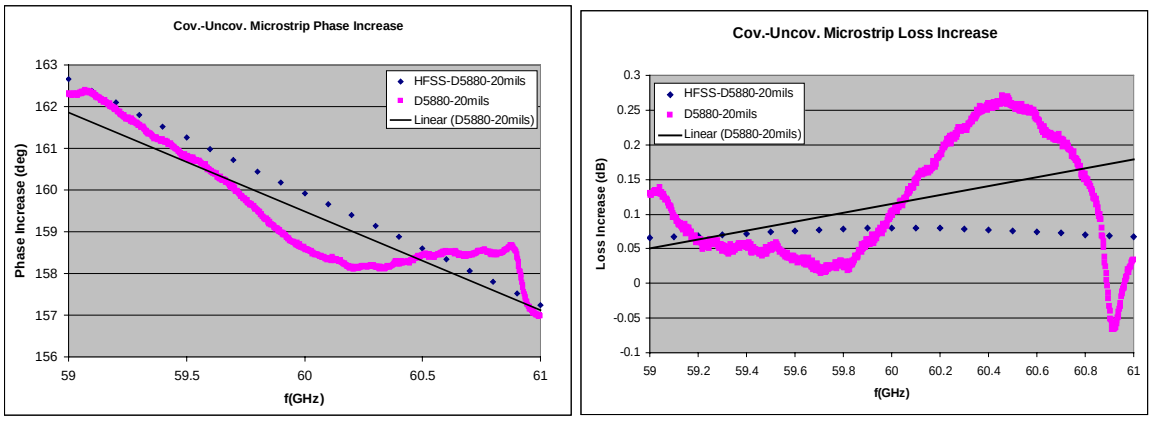

Fig. 5.8: RT/d5880 Calibration Results.

5.4. Measurement Results

Once simulation and experimental results are calibrated, we can proceed to determine the electrical properties of other materials. By doing a series of measurements and extracting the parameters $\Delta\theta_{meas}$ and $\Delta\alpha_{meas}$ from the S-parameters and working backwards in HFSS by changing the simulated test substrate permittivity and loss tangent, we can infer their value.

Fig. 5.9 presents the simulated and experimental results for Rogers material R03003. Simulations, conducted with $\varepsilon_r = 3.12$ and $\tan\delta = 0.003$. show the best possible agreement with experimental data.

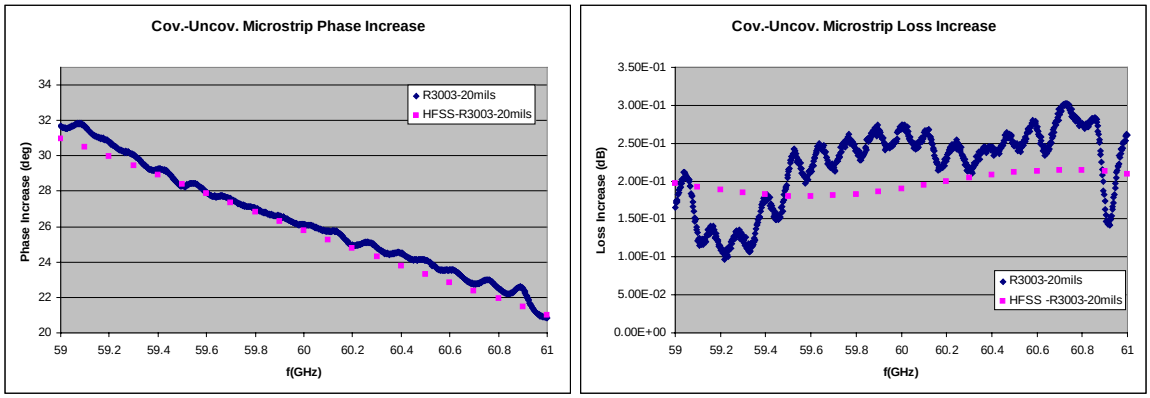

Fig. 5.10: R03003 two-layer stripline measurement and simulation results. Simulations with $\varepsilon_r=3.12$ and $tan\delta=0.003$.

Comparison on fig. 5.11 with test results provided by Rogers Corporation at lower frequencies shows a slight deviation from our measurement data and the observed material tendency over frequency. However, the deviation falls within the measurement uncertainties of the method.

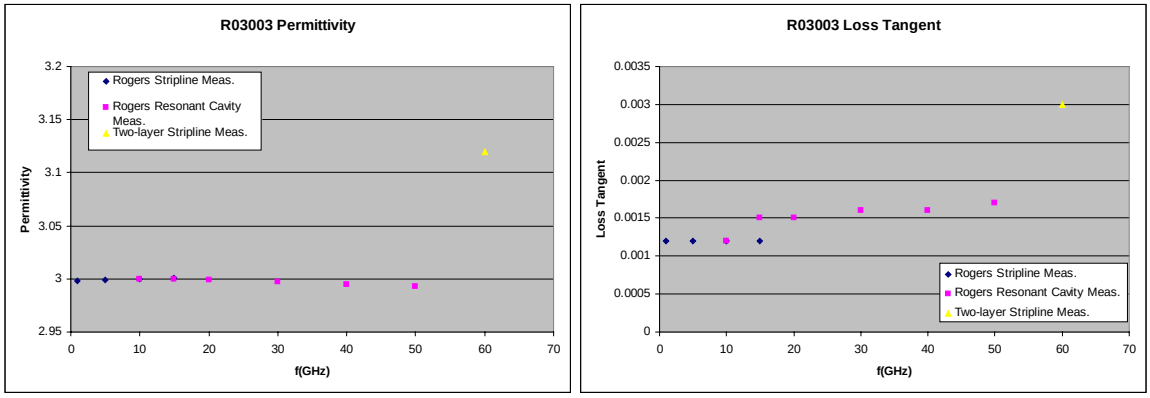

Fig. 5.11: R03003 Permittivity and loss tangent measurements over frequency using different methods.

Fig. 5.12 presents the simulated and experimental results for Rogers material R4350. Simulations, conducted with $\varepsilon_r=3.5$ and $tan\delta=0.01$. show the best possible agreement with experimental data.

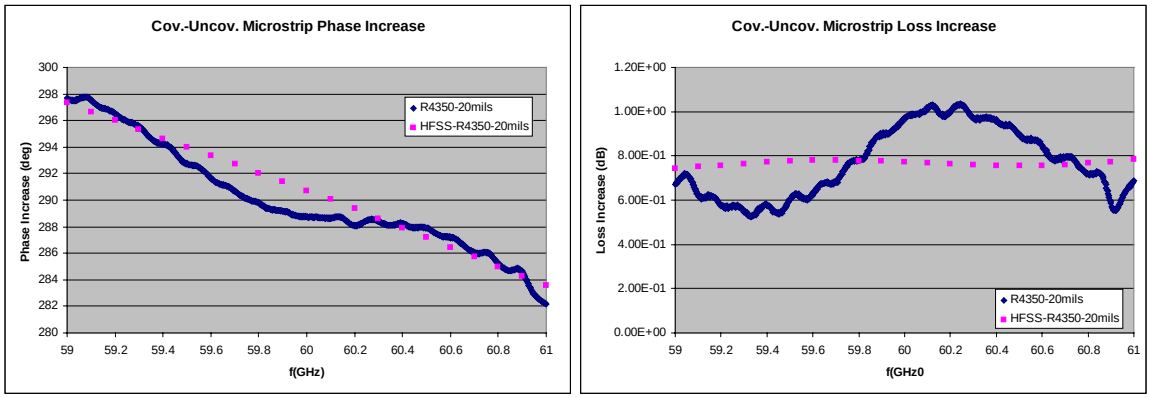

Fig. 5.12: R4350 two-layer stripline measurement and simulation results. Simulations, with $\varepsilon_r=3.5$ and $tan\delta=0.01$.

Comparison on fig. 5.13 with test results provided by Rogers Corporation at lower frequencies shows very good agreement with the material properties tendency over frequency. In particular, it correlates perfectly well with measurements using Rogers stripline method, meanwhile the resonant cavity underestimates the loss tangent.

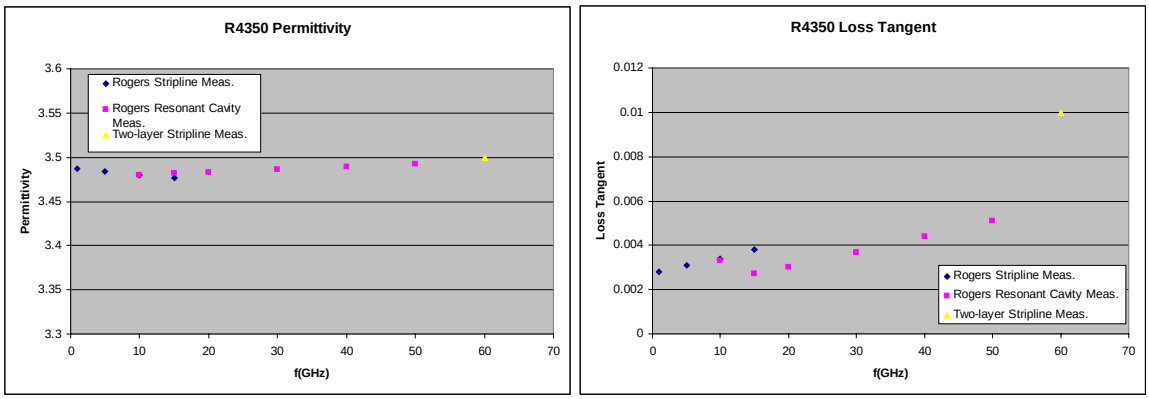

Fig. 5.13: R4350 Permittivity and loss tangent measurements over frequency using different methods.

Results provided in this section corroborate the suitability of the method to determine the electrical properties of various PCB and packaging materials. A more extensive study, including over 12 different materials has been conducted but results will not be available before 2 months time, due to simulation time requirements.

Part II

Design of a Waveguide Antenna Array for the 60GHz Band

Introduction

The 60GHz channel has some unique characteristics that differ significantly from the characteristics of communication channels in the low-GHz regime. Some of these differences stem from basic electromagnetic or materials properties (e.g. oxygen absorption) whereas some of these differences are caused by extrinsic factors such as regulatory or practical issues regarding device from factor.

As interest in 60GHz communications has grown, there have been numerous studies and measurement campaigns quantifying various parameters of the 60GHz indoor channel and its dependence on other physical parameters such as room size, building materials, and antenna configuration. However, still a lot of questions regarding antenna directivity, throughput, SNR (Signal to Noise Ratio) and communications scheme, among others remain unanswered.

In this section, the 60GHz communications channel is introduced and a qualitative discussion of the key characteristics of it is presented. A 60GHz waveguide array is designed for channel measurement purposes, covering the range from 57 to 63GHz and providing 15dB gain up to +/- 60deg beam tilt. To close, the conclusions of 60GHz channel studies conducted to the moment by other groups are presented.

Chapter 6

Key Characteristics of the 60GHz Channel

6.1. Oxygen Absorption and Material Penetration

It is known that oxygen molecules interact with microwave frequencies between approximately 50GHz and 70GHz. As a result, atmospheric oxygen absorbs microwave radiation in the 60GHz band, resulting in excess attenuation of the transmitted signal by as much as 15dB/km at sea level [19]. Since this attenuation is in addition to the Friis path loss (discussed in section 6.2) oxygen absorption severely limits the applicability of 60GHz communications to many long-range applications. However, for indoor, short-range applications such as WLAN or point-to-point media streaming, the O_2 absorption issue has little significance. For instance, a 100m transmit distance would suffer from

only 1.5dB of O_2 absorption; however, the Friis path loss equation predicts a path loss of 108dB over a similar distance, assuming 0dB antenna gain.

Of more significance to indoor communications are the transmissivity and reflectivity of common indoor building materials with respect to 60GHz radiation. Certain building materials are significantly more opaque at 60GHz radiation than to signals at lower frequencies. Measurement campaigns comparing the materials transmissivity at 60GHz to that of 2.5GHz [20], 1.7GHz [21] and 5.85GHz [22] all show that many common building materials have higher penetration loss and lower reflectivity at 60GHz than at these lower frequencies.

As a result of the poor material transmission at 60GHz, partitions in an indoor environment act as isolative boundaries between neighboring areas in a single building. As an example, the material attenuation through a standard wood door would be more than 16dB. Similarly, a typical interior wall and flooring constructions can attenuate 60GHz signals by as much as 24dB. Therefore, partitions in indoor structures, such as walls and floors, prevent appreciable signal energy from propagating from one room to adjacent rooms.

The implications of these findings are threefold: First, unlike low-frequency WLAN systems such as 802.11 a/b/g/n, a 60GHz wireless system is not well-suited to the typical residential deployment model, where a single base station is used to serve many mobile clients scattered throughout the house. The attenuation suffered at 60GHz by propagating through one (or more) interior walls or floors is likely to add too much path loss to make high-bandwidth communications feasible. A corporate setting, however, would be more conducive to a 60GHz WLAN deployment, as a ceiling-mounted base station could serve several mobile clients without suffering from material penetration issues, provided that the internal structure of the office was more akin to a “cubicle farm” than several distinct office rooms.

A second consequence of the poor material penetration at 60GHz is a corollary of the first: since walls and floors prevent signal energy from spilling out of one room into the next, each room naturally becomes its own microcell. Furthermore, since the structural partitions isolate the adjacent cells from one another, frequency reuse can be aggressively exploited. In other words each cell can utilize a large fraction (or perhaps the entirety) of the 7GHz of available spectrum without worrying about intercellular interference. As a result, typical concerns of spectrum efficiency are mitigated, since the opportunities for frequency reuse are significant.

Lastly, the poor material penetration of 60GHz radiation has an effect on the nature of the multipath present in the indoor channel. Most notably, even with omnidirectional antennae, the delay spread of 60GHz indoor channels tends to be smaller than that of lower frequency channels. The path length of multipath reflections is necessarily shorter at 60GHz, since the reflections of sufficient energy can only come from in-room objects.

6.2. Path Loss and Antenna Directionality

The Friis path loss equation describes the free-space path loss incurred by an electro-magnetic wave as it propagates from a transmitter to a receiver:

$$L = \frac{P_{RX}}{P_{TX}} = \frac{G_{TX} G_{Rx} c^2}{f_c^2 (4\pi d)^2} = \frac{G_{TX} G_{RX} \lambda^2}{(4\pi d)^2} \tag{6.1}$$

where P_{TX} and P_{RX} are the power at the transmitter and receiver, G is the antenna gain, f_c is the carrier frequency, λ is the carrier wavelength and d is the propagation distance. Note that the convention used here defines L as the ratio of the power received to the power transmitted. Hence, L is by definition less than or equal to 1 and a smaller value of L indicates a larger amount of path loss.

It can be shown that the antenna gain, G, is proportional to the antenna area, A, as follows:

$$G \propto \frac{A}{\lambda^2} \tag{6.2}$$

If it is assumed that the transmitter is an omnidirectional source and the expression from (6.2) is used for G_{RX}. The path loss equation becomes:

$$L \propto \frac{A_{RX}}{(4\pi d)^2} \tag{6.3}$$

where A_{RX} is the area of the receive antenna.

The Friis equation as shown in (6.1) has led many to conclude that the path loss irrevocably gets worse as the carrier frequency increases. In fact, a direct application of the Friis equation can lead to the conclusion that a 60GHz communications channel has 22dB more loss than an otherwise identical 5GHz communications channel. This conclusion is somewhat misleading, however, as the additional path loss incurred at higher frequencies is not due to some fundamental effect, but is primarily a consequence of the assumption that antenna gain is a fixed constant independent of frequency. As indicated by equation (6.2), the area of an antenna of a fixed gain scales inversely with frequency. Thus, an antenna of fixed gain will be physically smaller at higher frequencies and will capture a smaller fraction of the total radiated power.

The antenna gain, however, is not constrained to be a fixed constant or somehow limited by some a priori fundamental constraint. A more likely constraint is the overall size of the antenna aperture, as physical parameters, such as the size of the wireless device, places an upper-bound on the overall area that can be devoted to the antenna. If it is assumed that the antenna area, A, for a given device is fixed, the Friis equation takes the following form:

$$L \propto \frac{A_{TX} A_{RX}}{\lambda^2 (4\pi d)^2} \tag{6.4}$$

where A_{TX} is the area of the transmit antenna. Now it seems as if the path loss gets more benign as frequency increases, in direct contradiction of equation (6.1). From this, one might conclude that the use of higher carrier frequency and higher antenna gain provides a potentially unlimited benefit. In the example comparison between a 60GHz system and a 5 GHz system, it now appears that the 60GHz system could achieve an improvement in channel gain. Unfortunately, such an optimistic scenario is not the case either; since an antenna is a passive device, increasing the gain of an antenna can only be achieved by increasing its directionality. Directionality can provide many benefits to wireless communications –including the increased antenna gain described here- but it also presents several significant implementation challenges. In particular, the system complexity required to properly produce and align a directional array pattern grows significantly as the antenna gain is increased.

Therefore, it remains to be determined what kind of antenna is suitable for a 60GHz system. The benefit of an omnidirectional antenna is the simplicity of this approach: no additional hardware is necessary in order to create a directional, high-gain antenna pattern, and no scheme to align the pattern is required either. However, the increased path loss suffered at high frequency with an omnidirectional antenna would limit the capacity of the wireless link. An upper-bound of the channel capacity can be approximated using the Shannon capacity calculation for an AWGN channel. The Shannon capacity limit gives the maximum theoretical error-free capacity that can be achieved through a channel using arbitrarily complex coding schemes [23]. The Shannon capacity is:

$$C = BW \log_2\left(1 + \frac{P_{RX}}{BWN_0}\right) \tag{6.5}$$

where C is the channel capacity in bits/sec, BW is the channel bandwidth in Hz, and N_0 is the input-referred noise level at the receiver in W/Hz. In the case of 60GHz communications, the bandwidth is sufficiently large such that it can be approximated as infinite. Given that approximation, equation (6.5) simplifies to:

$$\lim_{BW\to\infty} C = 1.44\frac{P_{RX}}{N_0} \tag{6.6}$$

Equation (6.6) can be used as an upper-bound to determine the theoretically maximum capacity that can be achieved. A more conservative approximation of channel capacity can be based on the observation that common modulation schemes (e.g. BPSK, QPSK, and MSK) require a minimum receiver SNR in order to get a reasonable uncoded error rate. For these modulation schemes, in order to get an uncoded BER (Bit Error Rate) on the order of 10^{-3}, an SNR at receiver of roughly 7dB is required.

Using the Shannon capacity limit or the 7dB SNR requirement, the capacity of an omnidirectional 60GHz link as a function of transmit power can be determined. Figure 6.1 shows such a plot for a transmit distance of 10m and 20m. In this plot, it is assumed that the receiver has an overall noise figure of 10dB, and there are 10dB of losses from miscellaneous sources such as shadowing loss, board losses, and implementation loss. According to the Shannon capacity limit, the transmitter would require 23dBm transmit power to achieve a capacity of 1Gbps at 10m, according to the more realistic 7dB SNR criterion, the transmitter would have to output 30dBm of power to achieve this capacity.

Power amplifiers with these power levels are by now still unrealizable in commercially available CMOS technologies. Therefore, in order to realize a 10m, Gbps link at 60GHz, the path loss dictates that directional antennae are a requirement.

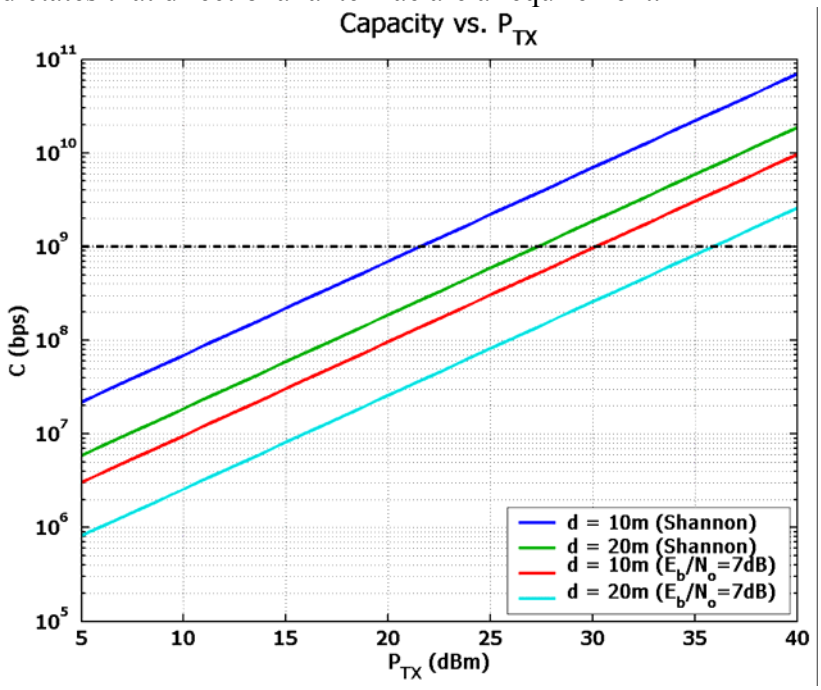

Fig. 6.1: Link capacity vs. transmit power for omnidirectional antenna.

6.3. Feasibility of a High Directionality Antenna

The previous sections demonstrate that the increased path loss at 60GHz and the limited performance of 60GHz CMOS circuits [24] necessitate the use of directional antennae. Luckily, at 60GHz the use of directional antennae becomes much more practical than at lower frequencies. The area required for an antenna of a particular gain is inversely proportional to the square of the carrier frequency. For instance, a rectangular aperture antenna with 12dBi directivity could be synthesized in a 5mm*5mm area at 60GHz, whereas a similar antenna at 2GHz would be 18.6cm on a side. Therefore, for small form-factor mobile devices where PC board real estate is at a premium, operating at 60GHz allows for the use of directional antennae that would be prohibitively large at lower frequencies.

Chapter 7

Waveguide and Radiation Theory

7.1. Rectangular Waveguides

A typical waveguide is fabricated with a hollow conductor. In the hollow rectangular waveguide of Fig. 7.1, only traverse electric (TE) or transverse magnetic (TM) waves can exist. Transverse electromagnetic (TEM) waves cannot propagate in the rectangular waveguide since there is only one conductor. The TE and TM waves can exist in an infinite number of modes. These modes correspond to the number of standing wave maxima that occur in the directions perpendicular to the direction of propagation. The modes that can propagate are dependent on the geometry of the waveguide.

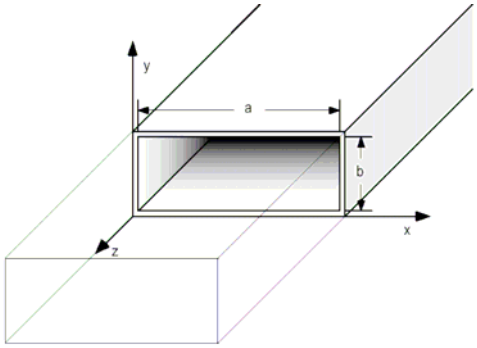

Fig. 7.1: Rectangular Waveguide

For any source free transmission line, Maxwell's curl equations take the form [25]:

$$\nabla \times \vec{E} = -j\omega\mu\vec{H}$$
$$\nabla \times \vec{H} + j\omega\varepsilon\vec{E} \qquad (7.1)$$

Using a vector identity the equations can be represented as the Helmholtz Equations

$$\nabla^2\vec{E} + k^2\vec{E} = 0$$
$$\nabla^2\vec{H} + k^2\vec{H} = 0 \qquad (7.2)$$

where the wave number $k = 2\pi f\sqrt{\mu\varepsilon}$, with f the frequency, μ the permeability and ε the permittivity.

The solutions of these equations for the TE and TM fields yield the classic results of the propagation modes given at reference [25].

When the mode of propagation is TE, the axial component of the electric field, E_z, must be zero. This will result in the propagation constant $\beta = \sqrt{k^2 - k_c^2}$ where k_c is the cut-off wave number given by:

$$k_c = \sqrt{\left(\frac{m\pi}{a}\right)^2 + \left(\frac{n\pi}{b}\right)^2} \tag{7.3}$$

If the wave is to propagate, then the phase constant, β, must be real. This is true for $k > k_c$. This results in a cut-off frequency for each mode (m,n) given by:

$$f_{c_m} = \frac{1}{2\pi\sqrt{\mu\varepsilon}}\sqrt{\left(\frac{m\pi}{a}\right)^2 + \left(\frac{n\pi}{b}\right)^2} \tag{7.4}$$

Frequencies below the cut-off will result in fields with an imaginary propagation constant that will attenuate exponentially. These waves are known as evanescent waves.

In general, waveguides are designed for the propagation of one mode, known as the dominant mode. This will simplify the design of elements used to couple energy to and from the waveguide. If more than one mode propagates, the waveguide is said to be overmoded. This is an undesirable condition and results in unwanted losses in the waveguide. Furthermore, as will be seen later, if the waveguide is used as an antenna element, single mode propagation allows for formation of the desired far-field radiation pattern. The dominant mode in a rectangular waveguide is the TE_{10} mode.

As waveguides do not leak, there are only two loss mechanisms: dielectric losses and losses due to finite conductivity. The losses due to the dielectric in a rectangular waveguide with TE or TM modes are given by:

$$\alpha_d = \frac{k^2 \tan\delta}{2\beta} \tag{7.5}$$

The losses due to the finite conductivity of the wall conductors (σ_c) for the fundamental TE_{10} mode are calculated by:

$$\alpha_c = \frac{\sqrt{\frac{\omega\mu}{2\sigma}}}{a^3 b\beta k\eta}\left(2b\pi^2 + a^3k^2\right) \tag{7.6}$$

The total attenuation constant for the rectangular waveguide is the sum of both coefficients

$$\alpha = \alpha_d + \alpha_c \tag{7.7}$$

7.2. Radiation from apertures

Given an aperture S_0 illuminated by known fields $\vec{E}$ and $\vec{H}$, related by the wave impedance Z_0 and defined by $\vec{E} = E_y \hat{y}$ and $\vec{H} = -\frac{E_y}{Z_0}\hat{x}$, that are equivalent to currents [26]:

$$\vec{J}_s = \hat{n} \times \vec{H} = \hat{z} \times \hat{x} \frac{-E_y}{Z_0} = -\frac{E_y}{Z_0}\hat{y}$$
$$\vec{M}_s = -\hat{n} \times \vec{E} = -\hat{z} \times \hat{y} E_y = E_y \hat{x} \tag{7.8}$$

The radiation vectors are:

$$N_y = \iint_{S_0} \left(-\frac{E_y}{Z_0} \right) e^{jk_x x'} e^{jk_y y'} dx' dy'$$
$$L_x = \iint_{S_0} E_y e^{jk_x x'} e^{jk_y y'} dx' dy' \tag{7.9}$$

with $k_x = k \sin\theta \cos\phi$ and $k_y = k \sin\theta \sin\phi$. Their components in spherical coordinates are:

$$N_\theta = N_y \cos\theta \sin\phi \qquad L_\theta = L_x \cos\theta \cos\phi$$
$$N_\phi = N_y \cos\phi \qquad L_\phi = -L_x \sin\phi \tag{7.10}$$

That result in radiation fields:

$$E_\theta = -j \frac{e^{-jkr}}{2\lambda r} \left(\eta N_y \cos\theta - L_x \right) \sin\phi$$
$$E_\phi = j \frac{e^{-jkr}}{2\lambda r} \left(-\eta N_y + L_x \cos\theta \right) \cos\phi \tag{7.11}$$

And as a function of illuminating fields:

$$E_\theta = j \frac{e^{-jkr}}{2\lambda r} \left(1 + \frac{\eta}{Z_0} \cos\theta \right) \sin\phi \iint_{S_0} E_y e^{jk_x x'} e^{jk_y y'} dx' dy'$$

$$E_\phi = j \frac{e^{-jkr}}{2\lambda r} \left(\frac{\eta}{Z_0} + \cos\theta \right) \cos\phi \iint_{S_0} E_y e^{jk_x x'} e^{jk_y y'} dx' dy' \tag{7.12}$$

Note that the expressions for the radiated fields can be interpreted as bidimensional Fourier transforms of the illuminating fields in the aperture. These expressions, that consider only the contribution due to the fields in the antenna aperture and not account for the residual currents in the exterior walls, provide accurate results only for directions close to the main lobe and first secondary lobes.

The directivity in planar apertures can be expressed as:

$$D = \frac{\wp_{\max}}{P_r / \left(4\pi r^2 \right)} \tag{7.13}$$

with $\wp_{\max} = \frac{|E_{\max}|^2}{\eta}$, where $|E_{\max}| = \sqrt{|E_\theta|^2 + |E_\phi|^2}$ and P_r is the antenna radiated power:

$$P_r = \frac{1}{\eta}\int_0^{2\pi}\int_0^{\pi}\left(|E_\theta(\theta,\phi)|^2 + |E_\phi(\theta,\phi)|^2\right) r^2 \sin\theta d\theta d\phi \tag{7.14}$$

7.2.1. Radiation from rectangular waveguides

The illuminating fields in a rectangular waveguide due to dominant mode TE_{10} are [26]:

$$E_y = E_0 \cos\left(\frac{\pi}{a}x\right)$$

$$H_x = -\frac{E_y}{Z_0} \tag{7.15}$$

with $Z_0 = \frac{\eta}{\sqrt{1-\left(\frac{\lambda}{2a}\right)^2}}$.

From (7.12) the radiation fields can be obtained, with resulting expressions:

$$E_\theta = j\frac{e^{-jkr}}{2\lambda r}\left(1+\frac{\eta}{Z_0}\cos\theta\right)\sin\phi\frac{\pi a}{2}\frac{\cos\left(k_x\frac{a}{2}\right)}{\left(\frac{\pi}{2}\right)^2-\left(k_x\frac{a}{2}\right)^2}b\frac{\sin\left(k_y\frac{b}{2}\right)}{k_y\frac{b}{2}}$$

$$E_\phi = j\frac{e^{-jkr}}{2\lambda r}\left(\frac{\eta}{Z_0}+\cos\theta\right)\cos\phi\frac{\pi a}{2}\frac{\cos\left(k_x\frac{a}{2}\right)}{\left(\frac{\pi}{2}\right)^2-\left(k_x\frac{a}{2}\right)^2}b\frac{\sin\left(k_y\frac{b}{2}\right)}{k_y\frac{b}{2}} \tag{7.16}$$

7.2.2. Radiation from H-plane Horns

The use of rectangular waveguides as radiators provides moderate directivities but present some mismatch at the radiation point. To increase directivity and adaptation the electrical dimensions have to be increased, assuring that the structure is still single mode. Size has to be increased gradually, in the form of a horn.

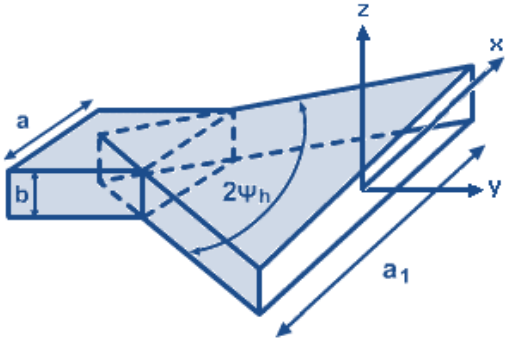

Fig. 7.2: H-plane Horn

For the Horn of picture 7.2 it can be demonstrated that the illuminating field is [26]:

$$E_y = E_0 \cos\left(\frac{\pi}{a_1}x\right) e^{j\beta\delta(x)} \tag{7.17}$$

with $\delta(x) = \frac{a_1^2}{8l_H} - \frac{x^2}{2l_H}$.

Radiation fields can be equally calculated from (7.12), resulting in:

$$E_\theta = j\frac{e^{-jkr}}{2\lambda r}\left(1 + \frac{\eta}{Z_0}\cos\theta\right)\sin\phi \int_{-a_1/2}^{a_1/2} \cos\left(\frac{\pi}{a_1}x'\right) e^{j\beta\delta(x')} e^{jk_x x'} dx' * b \frac{\sin\left(k_y \frac{b}{2}\right)}{k_y \frac{b}{2}}$$

$$E_\phi = j\frac{e^{-jkr}}{2\lambda r}\left(\frac{\eta}{Z_0} + \cos\theta\right)\cos\phi \int_{-a_1/2}^{a_1/2} \cos\left(\frac{\pi}{a_1}x'\right) e^{j\beta\delta(x')} e^{jk_x x'} dx' * b \frac{\sin\left(k_y \frac{b}{2}\right)}{k_y \frac{b}{2}} \tag{7.18}$$

7.3. Array Theory

As directional antennae are a requirement at 60GHz as has been previously demonstrated, and a single antenna does not provide enough gain, the end goal of the project is to develop an array. We define an array as a group of N equal antennas that radiate or receive simultaneously. The total field of the array is determined by vector addition of the fields radiated by the individual elements, and the placement and excitation of the array can be configured so that the net array radiation pattern has a high directivity aimed in the intended direction.

A common antenna array is the N-element linear array. This array is composed of N identical antennae that are placed in a linear fashion with an element-to-element spacing of *d* and fed by currents I_n, where n=0..N-1. Figure 7.3 shows an example of this array.

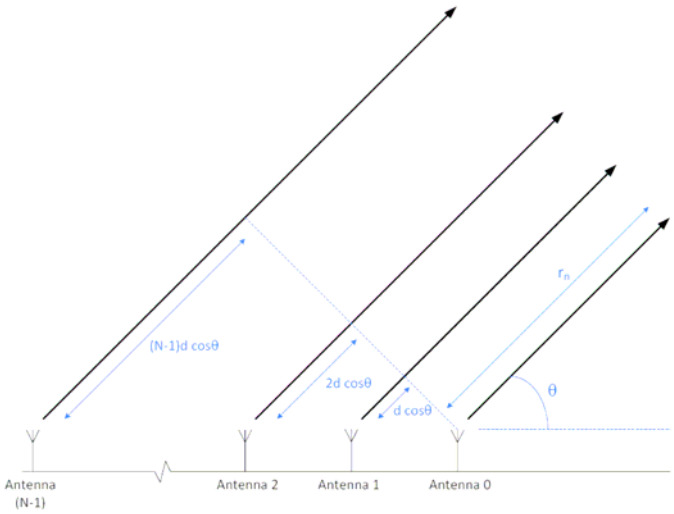

Fig. 7.3: N-element linear antenna array (Annotations in blue)

Following the development from [26] the expression for the radiation vector is:

$$\vec{N}(\hat{r}) = \vec{N}_0(\hat{r}) \sum_{n=0}^{N-1} I_n e^{jnkd\cos\theta} \tag{7.19}$$

As usually the feeding vectors present a progressive phase between consecutive antennae, we can express In as $I_n = a_n e^{jn\alpha}$. Combining the above equations:

$$\vec{N}(\hat{r}) = \vec{N}_0(\hat{r}) \sum_{n=0}^{N-1} a_n e^{jn(kd\cos\theta+\alpha)} \tag{7.20}$$

From the radiation vector, all the radiation characteristics from the antenna can be extracted. For example, the radiated electric field is:

$$\vec{E}(\hat{r}) = \vec{E}_0(\hat{r}) \sum_{n=0}^{N-1} a_n e^{jn(kd\cos\theta+\alpha)} \tag{7.21}$$

To simplify the calculus, we can express (7.21) as a function of the electrical angle ψ $\psi = kd\cos\theta + \alpha$ that represents the phase difference between the far field contributions of 2 consecutive antennae. Using this notation, the radiated electric field by the array is:

$$\vec{E}(\hat{r}) = \vec{E}_0(\hat{r}) \sum_{n=0}^{N-1} a_n e^{jn\psi} \tag{7.22}$$

We can observe that the radiated field diagram is the product of the basic antenna diagram $\vec{E}_0(\vec{r})$ by a factor that accounts for the interference produced by the N waves generated by the N antennas. This factor, called Array Factor (AF) depends uniquely on the separation between antennas, the feeding and the frequency of operation:

$$AF(\psi) = \sum_{n=0}^{N-1} a_n e^{jn\psi} \tag{7.23}$$

Chapter 8

Waveguide Array Design and Analysis

8.1. Design constraints

The main objective of the global project is to perform 60GHz channel measurements to temporarily characterize the 60GHz channel and extract a variety of metrics ranging from path loss to RMS (Root Mean Square) delay spread and material transmissivity and reflectivity. Also, the impact of antenna directivity and alignment in both LOS (Line of Sight) and NLOS (Non-Line of Sight) environments has to be analyzed.

The array should thus, cover the frequency range from 57 to 63GHz and be composed of between 6 to 8 elements to enable beamforming and provide sufficient gain (around 15dB) to ensure 10m range coverage.

The array and feeding network has to be designed so each antenna can be connected to EW601W and EW602W transceivers (see annex III for specifications), provided by Endwave. The main feature of these transceivers is that they operate from 57 to 59GHz and 61 to 63GHz and provide waveguide WR15 outputs for the high-frequency signal.

Fig. 8.1: EW601W 60GHz transceiver.

8.2. Proposed Solution

One of the problems we face at these frequencies is represented by the fact that any beamforming structure such as microstrip antenna patches will require a feed network to provide the proper signal to the antenna in the array. However, traditional substrates that

are currently used for WLAN products today, such as fiber glass laminates, present prohibitive loss factor at 60GHz and can completely cancel the advantage of the array gain. Therefore, a more expensive type of substrate or alternative solution will have to be investigated.

Given that the transceivers outputs are WR15 waveguides, and in order to reduce the complexity of the feeding network to bring the 60GHz signal to the antennae and reduce the path losses, we will consider open-ended metallic waveguides as the basic radiating element.

From the open-ended waveguide radiation fields of (7.16) and applying (7.13), the basic element directivity is 6.6dB. Considering a linear array with element spacing of λ/2 at 60GHz and same feeding amplitude, with 8 elements, the array factor provides 9dB. Thus, the directivity of the array would be 15.6 dB.

The effective gain of the antenna can be extracted from:

$$G = \eta_{rad}\eta_{mat}D \tag{8.1}$$

where η_{rad} is the radiation efficiency, η_{mat} the matching efficiency and D the directivity. From (8.1) we can deduce that to ensure 15dB gain we will need higher directivities, as the combined efficiencies are rarely above 80%.

The use of flare horns eases the transition from waveguide to air, improves bandwidth and provides higher directivity. From (7.18) and (7.13), the horn provides 8.77dB directivity and 8 elements arrayed in the same fashion achieve a directivity of 17.77dB.

The proposed solution consists then on an 8 element H-plane horn terminated waveguide array, with structure as shown in picture 8.2. Design drawings can be found in annex V.

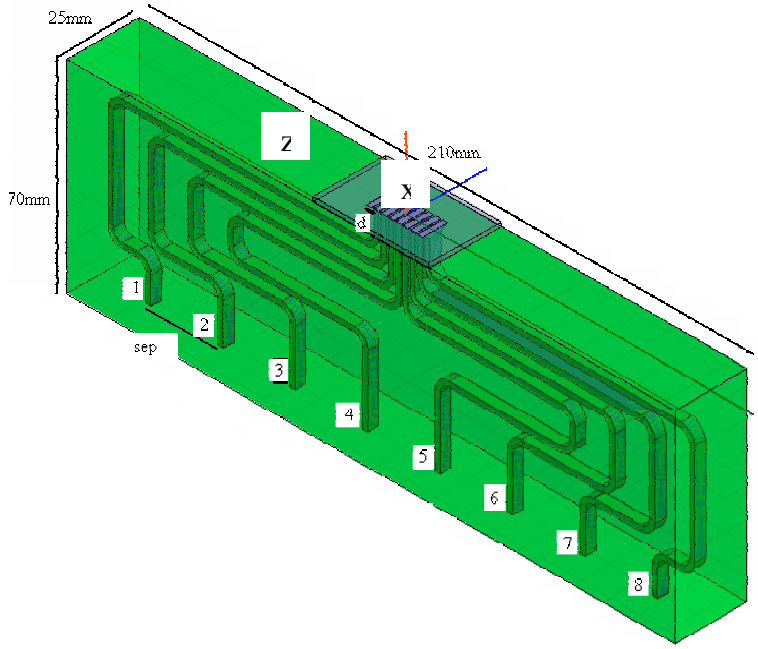

Fig. 8.2: Waveguide Array Design

Due to the small wavelength the openings of the array are packed tight together (λ/2=2.5mm at 60GHz). However, since the feed is done using standard WR15 waveguide (see annex III), a space between the lines must be added to be able to have connection with the transceiver modules. In order to obtain this, each waveguide is shaped such that the signal goes through identical path length and same number of transitions. This will guarantee accurate phase and magnitude of the signal at the mouth of each horn.

The electrical length of waveguides is a function of frequency:

$$\lambda_g = \frac{v_p}{f} = \frac{2\pi}{\beta} = \frac{\lambda}{\sqrt{1-\left(\frac{\lambda}{2a}\right)^2}} \tag{8.2}$$

In order to ensure that fields are in phase at the aperture, all waveguides need to have lengths that differ $n\lambda_g$ where n is an integer. As can be extracted from figure 8.3 and figure 8.4, no design at a specific frequency can guarantee the same phase at the radiation point for the whole bandwidth. Thus, we have to ensure by design that all the paths that drive the signal from the feeding point to the antennae have the same physical length.

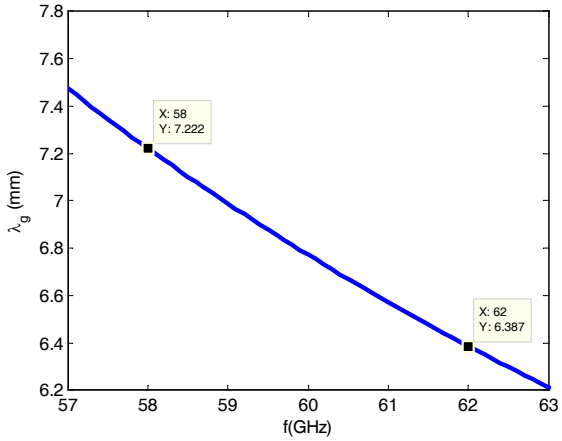

Fig. 8.3: Waveguide wave length as a function of frequency.

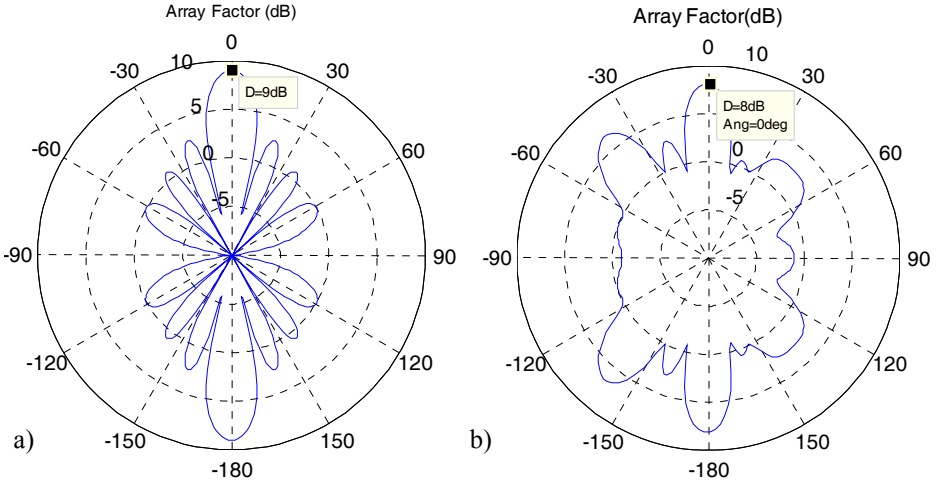

Fig. 8.4: Array factor for λ,2λ,3λ,λ,2λ,3λ path length elements at: a) 58GHz; b) 62GHz.

8.3. Analytical array results

Given the equations for the radiation pattern and array factors detailed in chapter 7, it is possible to study the ideal behavior of the 8 element array depicted in figure 8.2. It is important to note that the following results are from uniform phase and/or progressive phase excitation apertures. Effects of non-identical elements are studied in 8.5.

← sin(π)

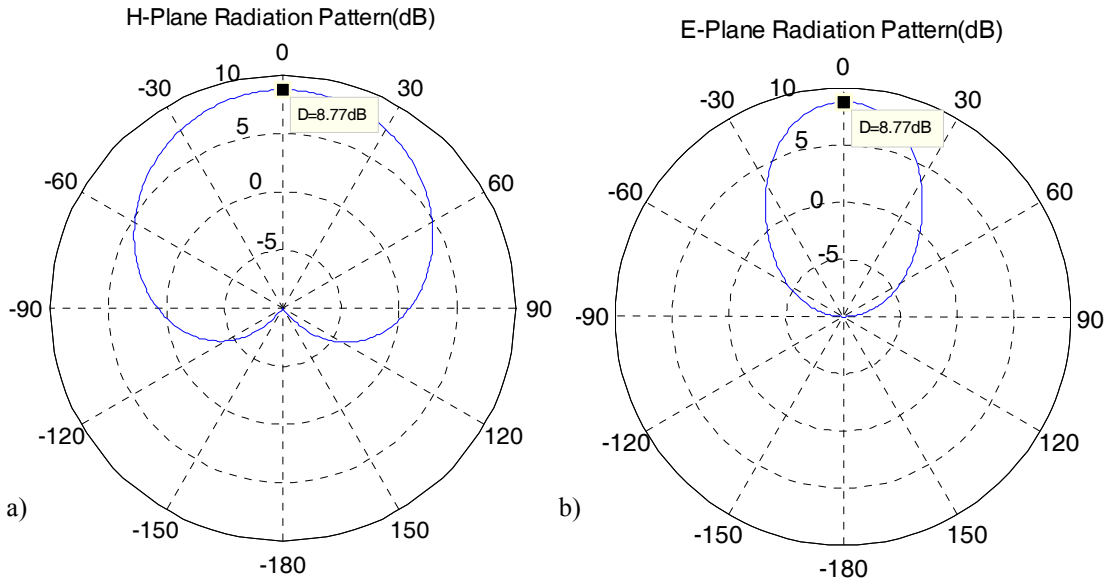

Fig. 8.5: H-plane Horn radiation pattern at 60GHz a) H-Plane b) E-Plane

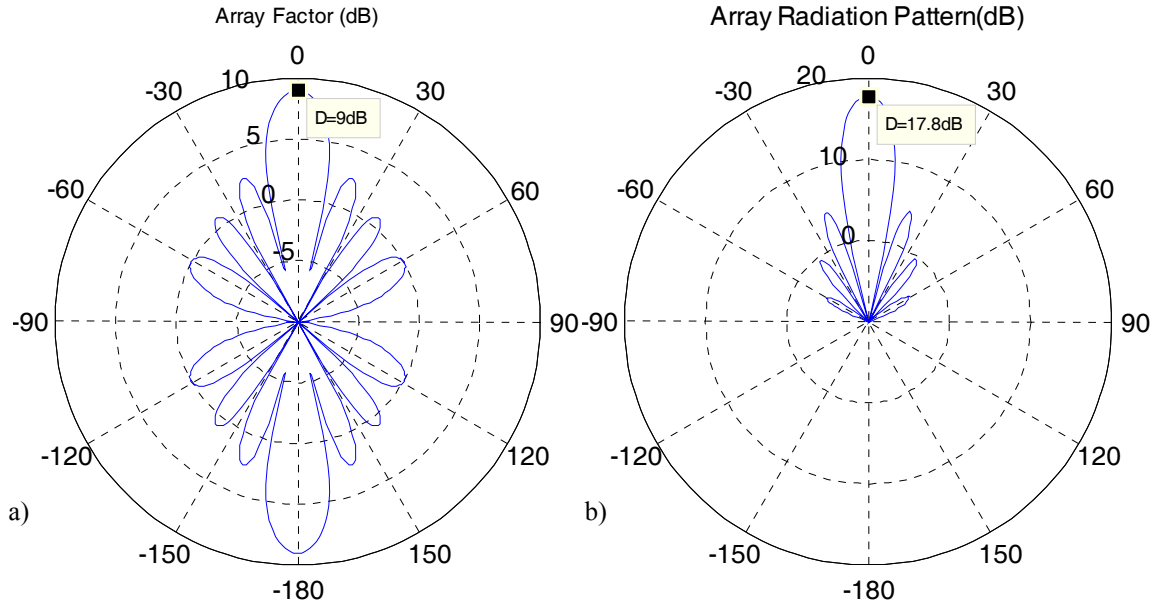

Fig. 8.6: a) 8-element Array Factor, b) H-plane radiation pattern of the proposed antenna array.

Figure 8.5 shows the theoretical horn radiation pattern for the E and H-planes. The directivity of the basic element is 8.77dB. Figure 8.6 shows the array factor for uniform excitation coefficients and the H-plane array radiation pattern, with a directivity of 17,8dB. As can be seen, the array factor has resulted in additional side lobes in the H-plane. These side lobes can be eliminated if the excitation coefficient follows a binomial distribution, but this option will not be analyzed here.

It is also possible to electronically scan the main beam. As the array has elements along the y-axis, it can only be effectively scanned along this axis, which is H-plane. To direct the beam in the direction of θ_{max}, the required phase shift between elements is given by:

$$\alpha = -kd\sin(\theta_{max}) \tag{8.3}$$

The result of the array radiation pattern for progressive phase shifts of 10, 50, 100 and 150 deg. is presented in figure 8.7. As can be seen, the 8-element array can be scanned to +/-60deg. from broadside with a directivity of 14dB. Higher scanning angles are not possible due to high gain additional side lobes.

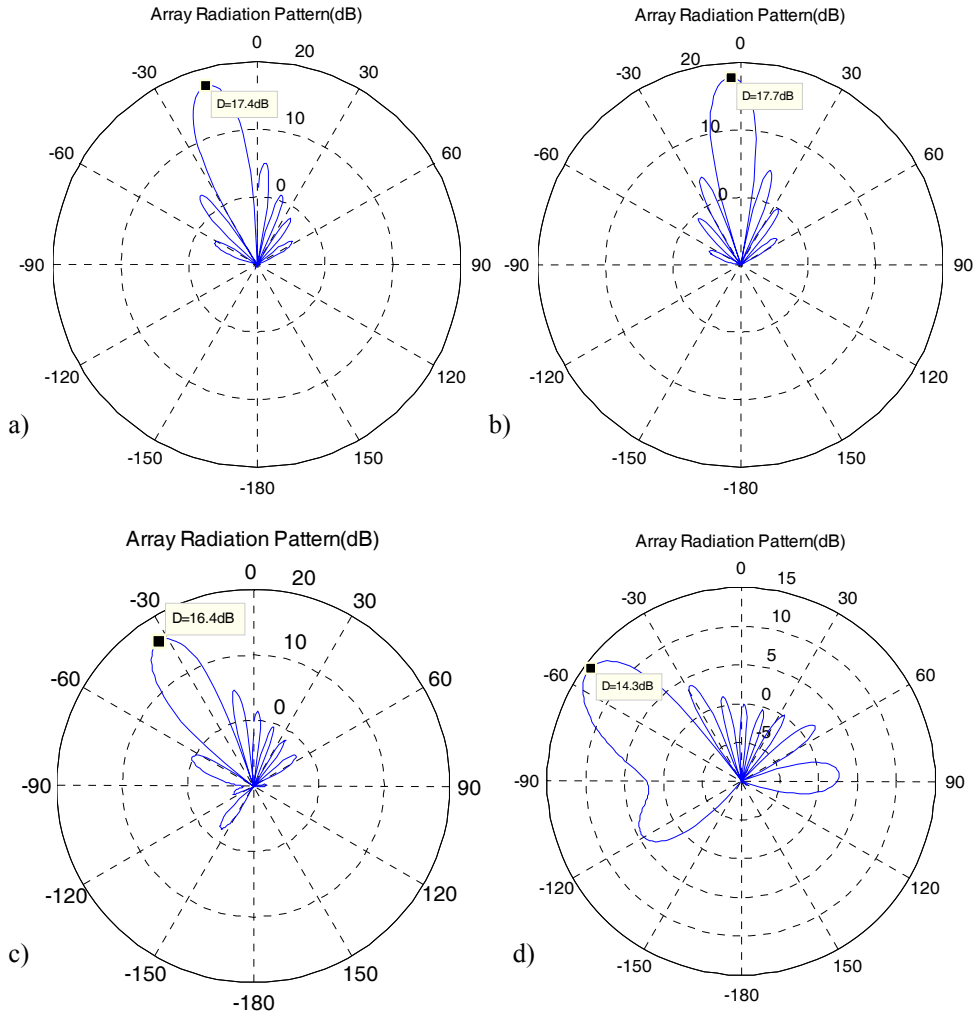

Fig. 8.7: Array radiation pattern at 60GHz for different progressive phase shifts: a) α=10deg. b) α=50deg. c) α=100deg. d) α=150deg.

8.4. HFSS array results

Simulation of a single element provides 60 GHz radiation patterns shown in figure 8.8. Comparison with the theoretical results provided in the previous paragraph shows very good agreement.

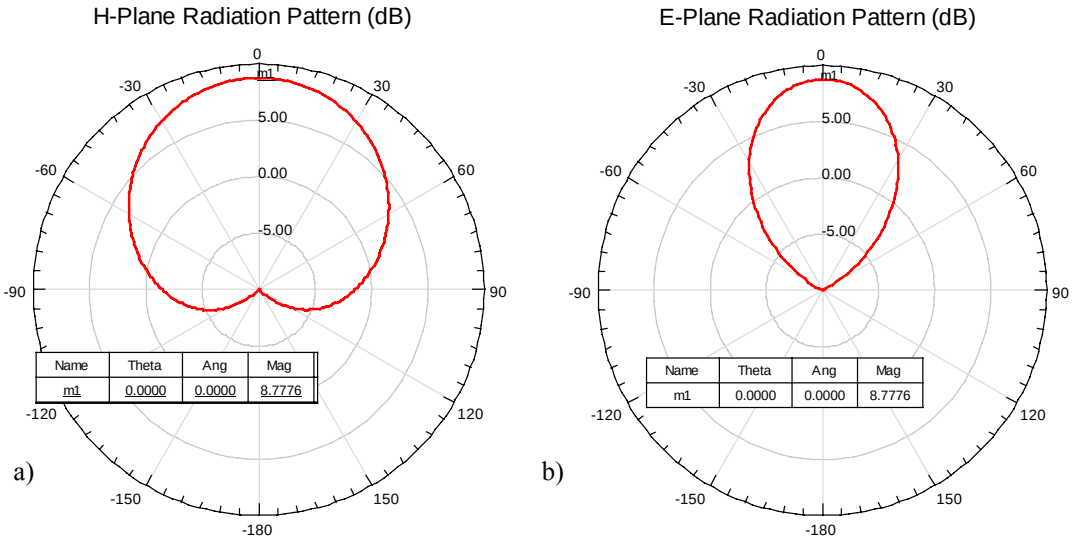

Fig. 8.8: H-plane Horn radiation pattern a) H-plane; b) E-plane.

Simulations of the whole array show that a directivity larger than 17.4 dB is obtained over the whole bandwidth without any noticeable beam distortion for broadside radiation (fig. 8.9). For progressive phase shifts of 10, 50, 100 and 150deg. the beam is tilted up to 60deg. in the H-plane for all the frequency of interest, as shown in fig. 8.10.

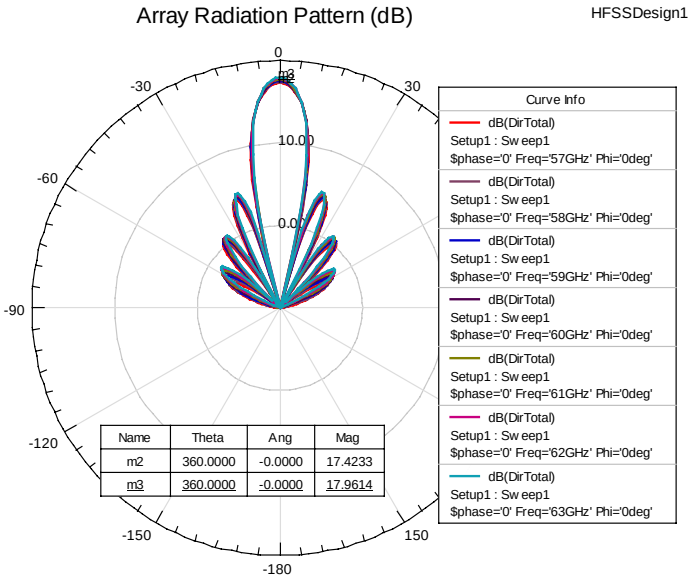

Fig. 8.9: Broadside Array Radiation pattern at various frequencies.

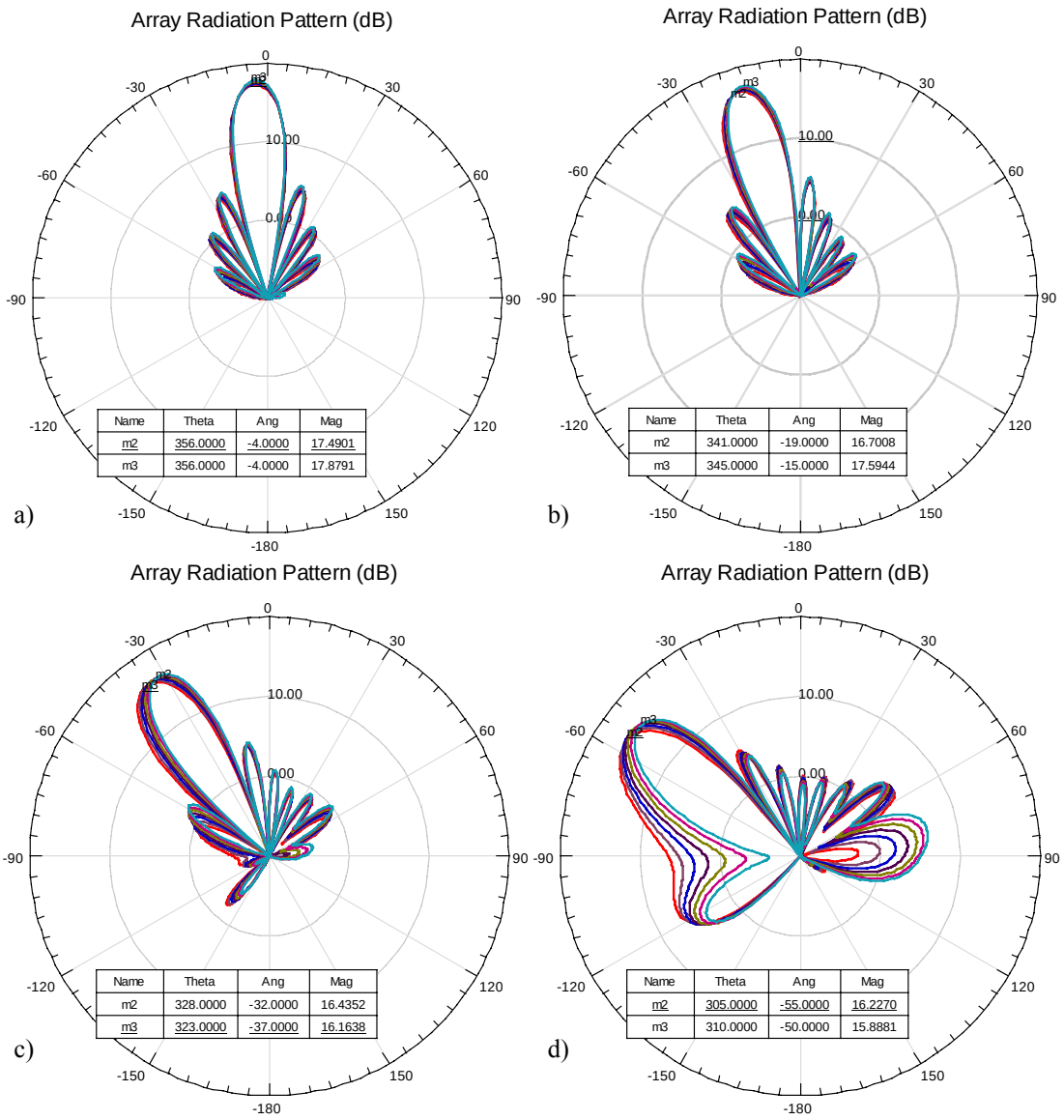

Fig. 8.10: Array radiation pattern at various frequencies for different progressive phase shifts: a) α=10deg. b) α=50deg. c) α=100deg. d) α=150deg.

Again, comparison with theoretical results provides good agreement. Slightly greater directivities for bigger beam scanning angles are obtained by simulation, but this is because theoretical equations offer precise results only for directions close to the broadside direction and immediate lobes.

Because of the high frequency of operation, several practical factors also have to be considered in the design. The waveguide material and its roughness will play an important role on the antenna final performance. Figure 8.11 shows the antenna computed efficiency for different materials (brass, gold, aluminum and silver) over the frequency band. Results show that efficiency increases with the conductivity of the

material, being gold and silver the best options, with a preference for gold as it does not oxide. The perfect electric conductor case has been included for comparison.

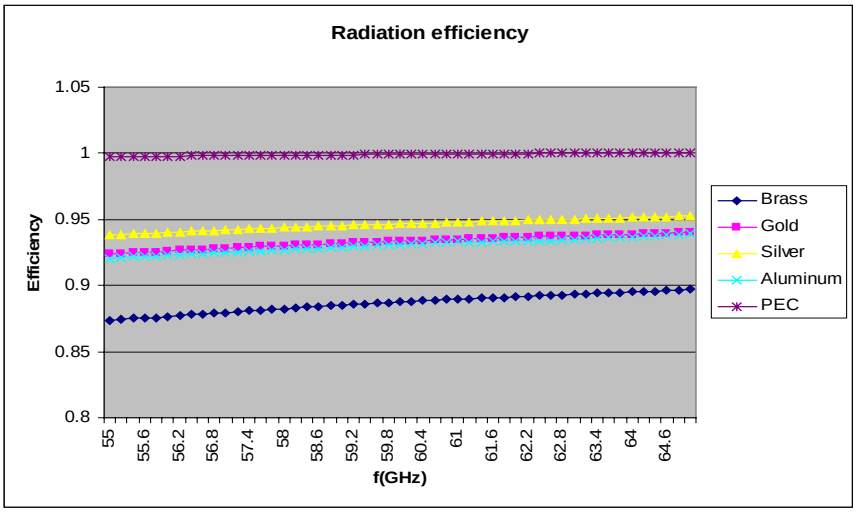

Fig. 8.11: Radiation efficiency versus frequency for some common waveguide materials.

Surface roughness of the material will decrease the ideal efficiency coefficient previously computed. Fig. 8.12 shows the results for brass with 100um surface roughness. It is found that there is a direct relationship between surface roughness and RF surface resistivity. Low loss can be achieved when the internal part of the waveguide is smoothed using chemical or abrasive smoothing techniques.

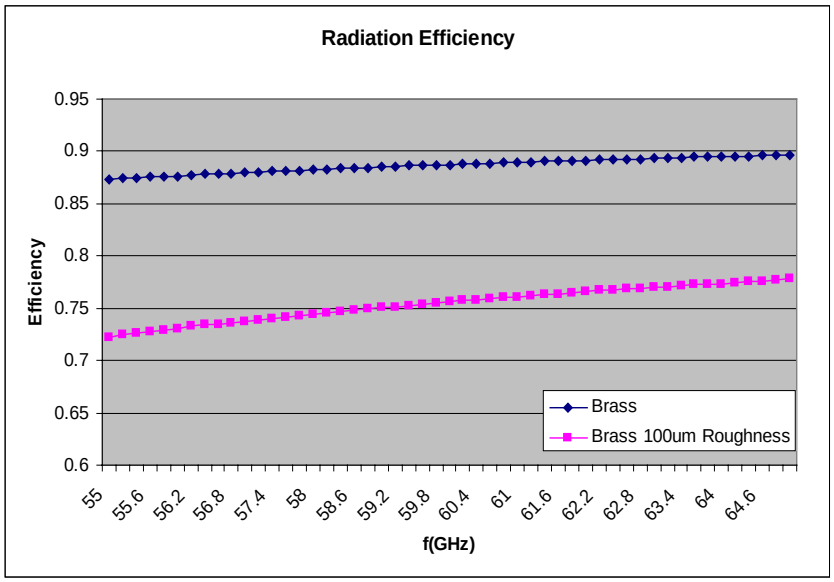

Fig. 8.12: Surface Roughness effect on the radiation efficiency versus frequency.

As the final gain of the array depends also on the matching efficiency (8.1), we have to take into account the return losses. Fig. 8.13 shows the return losses versus the progressive phase shift at 4 different frequencies. Good matching (-10dB) is obtained up to 120deg. at the lowest frequency. Scanning up to 150deg is still possible tough the gain

will be reduced by 1.25dB (see table. 8.1). At higher frequencies matching is below 10dB until 150deg.

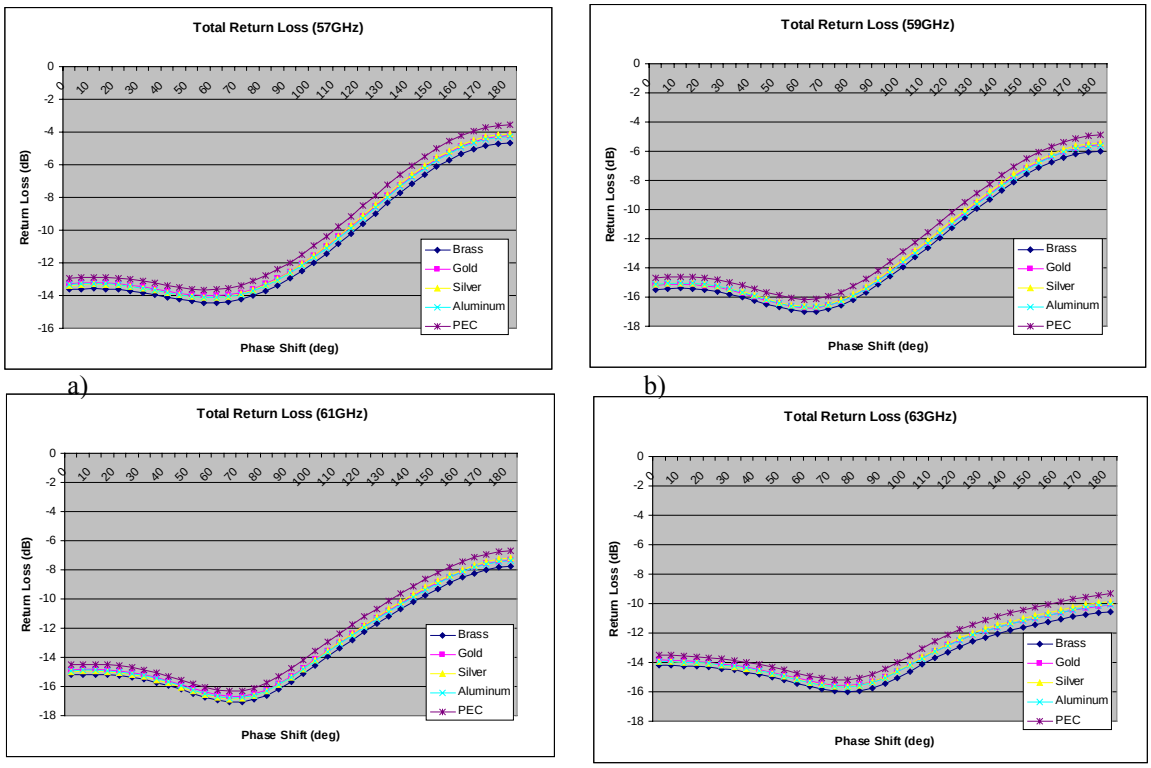

Fig. 8.13: Return losses versus phase shift at: a) 57GHz; b) 59GHz; c) 61GHz; d) 63GHz.

Return Loss	Mismatch Loss
-12dB	0.22dB
-10dB	0.46dB
-8dB	0.75dB
-6dB	1.25dB
-4dB	2.2dB

Table 8.1: Mismatch Loss incurred given a return loss.

8.5. Array Performance versus Errors

Fabrication tolerances, phase shifters noise and some transceiver malfunctioning will influence on the radiation pattern. In order to size the effect of each of these parameters on the array performance, some simulations have been conducted.

8.5.1. Waveguide length

All waveguides have been designed to have the same length, but fabrication produces it to randomly vary. Assuming that the maximum deviation is +/-1mm, corresponding to a

maximum of approximately 75deg phase shift at the radiation point, the effects on the theoretical array factor (fig. 8.14) can be viewed on figures 8.15 to 8.17 and can be divided in two categories:

- **Beam deviation from the theoretical pointing direction**. The shift on the beam corresponds to the beam tilt due to a phase shift at the radiation point equal to the slope of the regression line.
- **Appearance of high gain secondary lobes**. Constructive interference on other than the main direction creates secondary lobes that will decrease directivity in the desired direction.

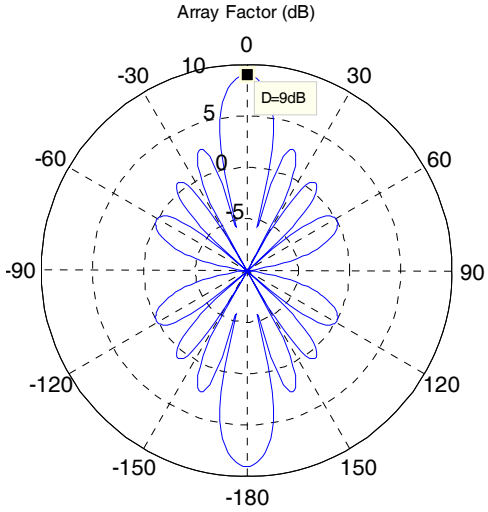

Fig. 8.14: 8-element theoretical array factor at 60GHz.

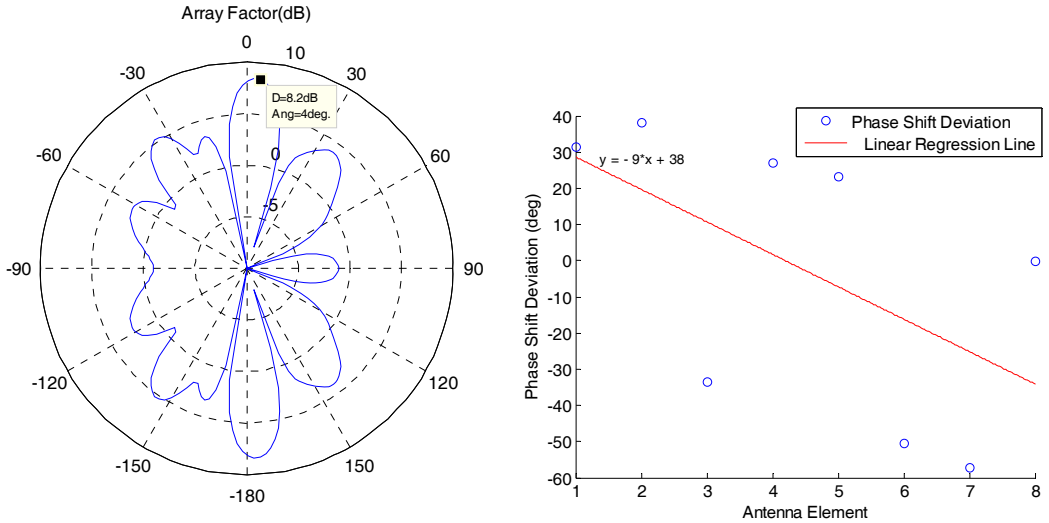

Fig. 8.15: Array Factor at 60GHz due to the given random Phase Shift Deviation at radiation point.

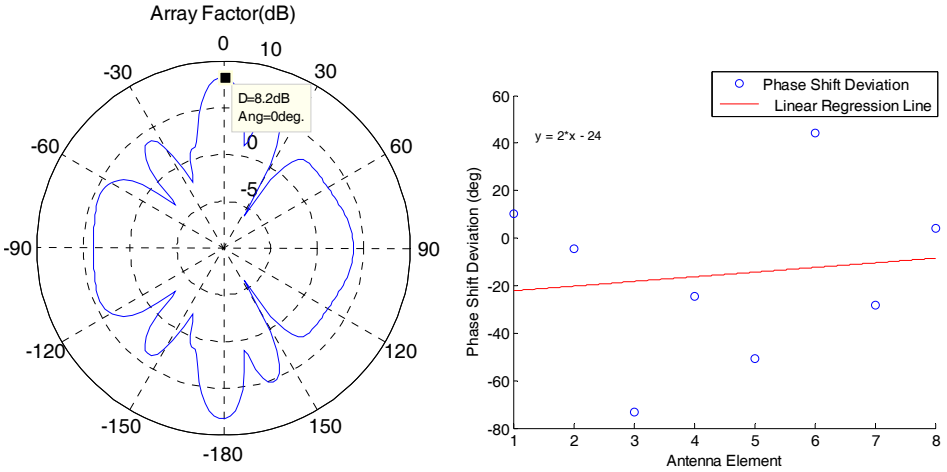

Fig. 8.16: Array Factor at 60GHz due to the given random Phase Shift Deviation at radiation point.

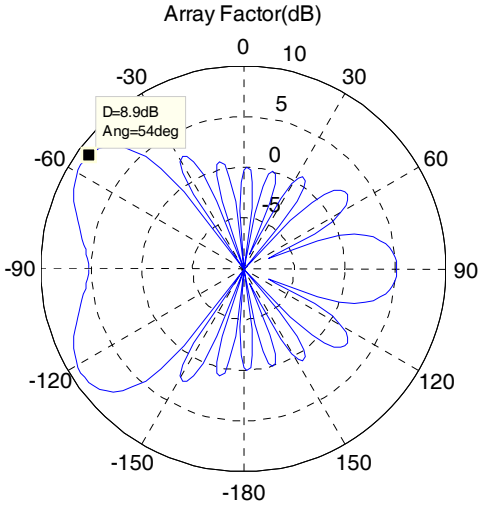

Fig. 8.17: 8-element theoretical array factor at 60GHz with α=150deg.

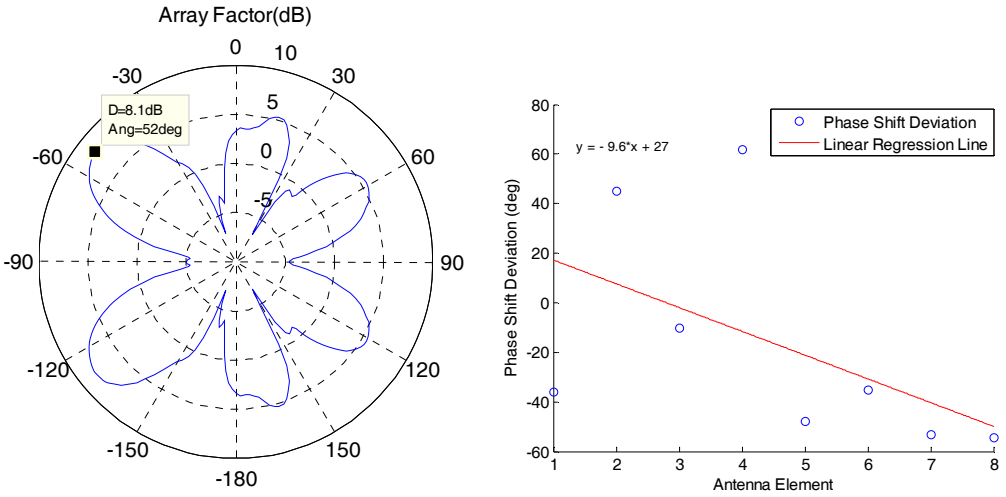

Fig. 8.18: Array Factor at 60GHz due to the given random Phase Shift Deviation at radiation point with respect to α=150deg.

8.5.2. Phase Shifters Accuracy

Supposing a phase shift deviation from nominal value of a maximum of +/- 15deg in the phase shifters, the effects on the radiation pattern can be neglected. As seen in figure 8.19, neither the direction of maximum radiation is appreciably changed nor do high gain side lobes appear.

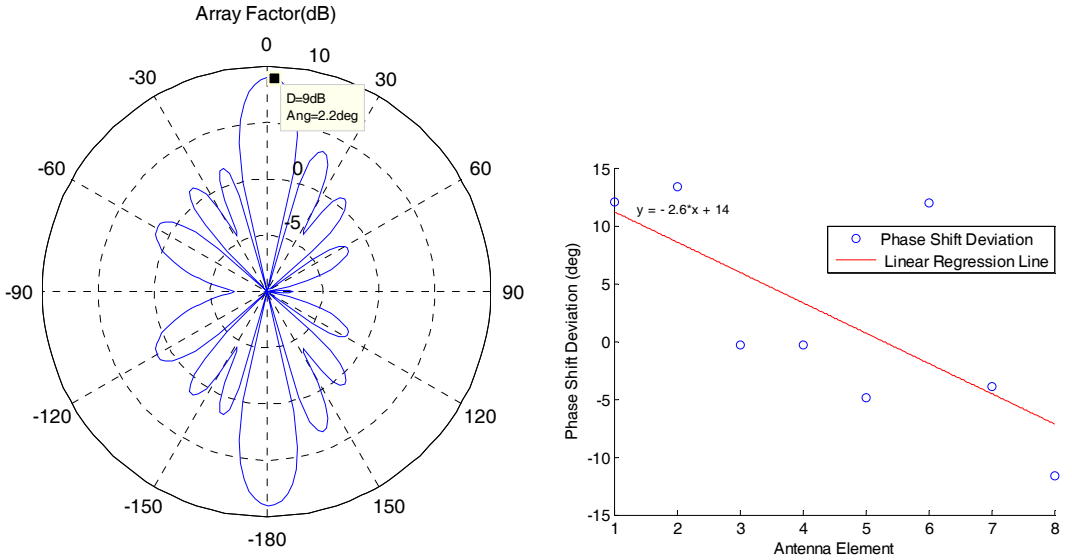

Fig. 8.19: Array Factor at 60GHz due to the given random Phase Shift Deviation at radiation point.

Also, one of the transmitters could be working completely out of phase due to some malfunctioning. In this case, the maximum radiation direction is not altered, and the worst effects consist on the appearance of high gain side lobes, as seen in fig. 8.20.

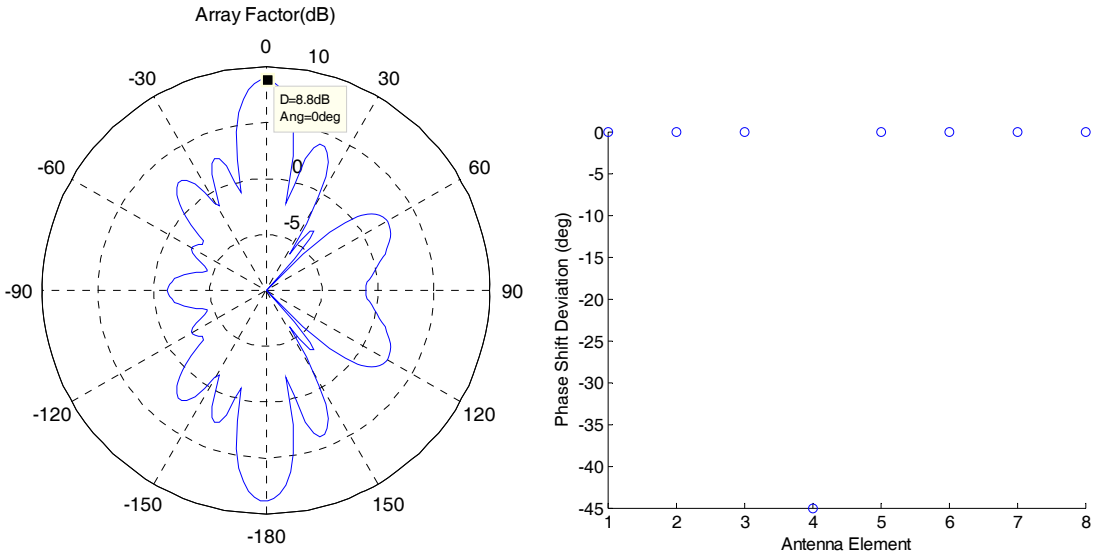

Fig. 8.20: Array Factor at 60GHz due to the given random Phase Shift Deviation at radiation point.

8.5.3. Calibration

From the above results, and having into account that in the worst case all these errors will add up, calibration is required to ensure the desired behavior of the array. In this direction, a calibration piece (see fig. 8.21) has been designed.

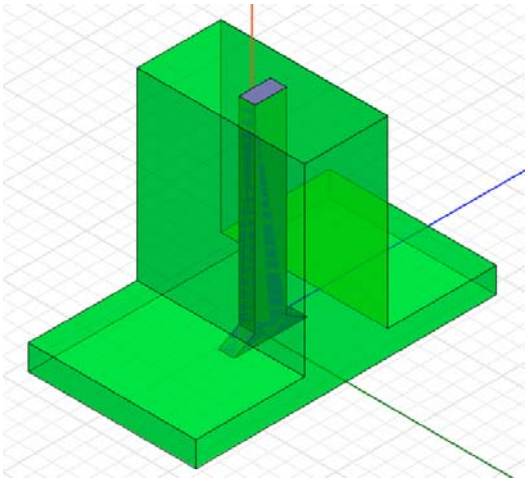

Fig. 8.21: Waveguide Array Calibration Piece.

This piece consists on a WR15 waveguide ended on a flare horn of the same dimensions of the array horns. A unique piece has to be sequentially connected to each antenna, and by measuring the phase of the received signal at all antennas, the phase deviation can be known. It is important that the same piece is used to calibrate all antennas to ensure no errors due to fabrication length tolerances (refer to 8.5.1) affect measurements.

With this calibration method, if phase shifters are included at the feeding point, by tuning them, all the above error sources can be compensated for. The only phase deviation could be due to a misaligned connection between each antenna and the calibration piece. Misalignment effects on the measured phase can be seen in figure 8.22.

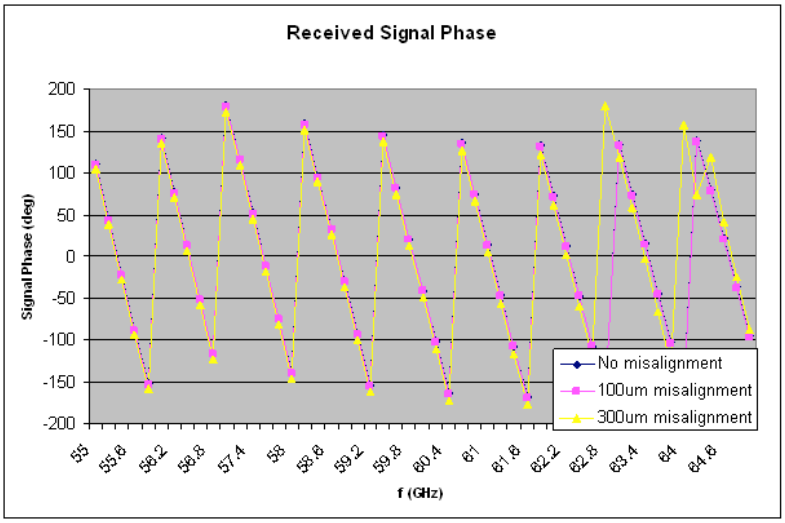

Fig. 8.22: Interconnection misalignment effect on measured received signal phase.

For small misalignments, only a few degrees (2deg. with 100um misalignment) deviation is observed. Given the results from 8.5.2, where errors up to 15deg. were considered, this phase errors can be neglected as they do not have appreciable effects. Greater misalignments (>300um) should be avoided using guide pins for precise interconnection. If this is not possible due to the tight spacing between antennas and reduced dimensions, measurements should be taken at the lowest frequencies, where the deviation is smaller.

8.6. Conclusions

In the light of all the results exposed in this chapter, we can conclude that:

- A 60GHz waveguide 8-element array with 15dB gain, beam scanning capability up to +/-60deg. from broadside and covering the frequency range from 57 to 63GHz is feasible.
- Its performance is verified both by simulation and theoretically, with very good agreement between all results.
- To maximize radiation efficiency the waveguide has to be gold or silver plated, with a preference for gold platting, as it does not oxidize.
- Careful attention has to be put on the fabrication process to ensure minimum surface roughness. In that direction some chemical or abrasive smoothing technique will have to be applied.
- As calibration is necessary, a calibration method of the array is designed so the desired phase shift at the radiation point can be ensured.

Chapter 9

Literature Review of 60GHz Channel Studies

The recent interest in 60GHz communications has led to a number of studies of the properties of the 60GHz indoor channel in an effort to characterize it in an accurate manner. The studies published in literature fall into one of two categories: measurement-based campaigns and simulation-based campaigns using ray-tracing tools. Each technique has their own set of advantages and complement the other. Measurement-based campaigns generate the required physical data of 60GHz propagation, transmission, and reflection that form the basis of any understanding of the 60GHz channel. However, measurement campaigns are labor-intensive and as a result are limited in their scope and in the diversity of physical environments measured. Simulation-based campaigns can build upon the measurement campaigns by applying the propagation and material properties discerned from these earlier studies and quickly and easily applying them to a variety of physical environments and room geometries. As will be discussed below, these studies indicate that the indoor channel properties are heavily dependent on room geometry and configuration, so a wide variety of environments need to be simulated. As mentioned above, channel simulations generally have used optics-based ray-tracing tools to simulate the wave propagation and generate a deterministic channel model for a particular environment. One limitation for ray-tracing simulators is that they typically do not model diffusion, diffraction or other scattering mechanisms; however, many studies of the 60GHz channel indicate that these scattering mechanisms typically do not occur in 60GHz indoor channels and that a ray-traced simulation with only specular reflections will produce valid data.

9.1. Material Properties

Many of the measurement studies characterize the reflectivity and transmissivity of common indoor building materials. The transmissivity of a material is typically specified as the transmission loss (in dB/cm) that 60GHz radiation incurs while propagating through a given distance of that material. The reflectivity of a material is typically specified as the loss incurred by reflecting off the surface of that material. Table 9.1 summarizes the material property measurements of a few measurement campaigns.

	Ref [27]		Ref [28]	Ref [29]	Ref [20]	Ref [30]
Material	Trans (dB/cm)	Refl (dB)	Refl (dB)	Trans (dB/cm)	Trans (dB/cm)	Trans (dB/cm)
Concrete	>6	6.5	N/A	6.67	N/A	6.7
Plasterboard	2	5.5	14.8	1.5	2.4	N/A
Wood	6.3	18	14	4.2	N/A	4.2
Chipboard	N/A	N/A	N/A	5.15	N/A	5.1
Acrylic glass	4.2	5.5	7.3	1.03	N/A	N/A
Glass	5.1	12	N/A	5.05	11.3	6.03
Wire-mesh glass	>14	3	N/A	N/A	31	N/A
Office whiteboard	N/A	N/A	N/A	N/A	5	N/A

Table 9.1: Transmission and reflection loss of common building materials at 60GHz.

A few conclusions can be reached by looking at the table above. First, material transmission at 60GHz is poor, particularly through exterior structural elements such as concrete and wood. Therefore, 60GHz communications is not suitable for short-range building-to-building links where LOS is not guaranteed. Even in indoor environments with most building materials of typical thickness, room-to-room isolation is usually greater than 20dB. Therefore, 60GHz links seem most suitable to single-room environment, and a microcellular approach utilizing a high degree of frequency reuse is realizable.

Additionally, non-metallic building materials tend to be poor reflectors of incident 60GHz radiation. With the exception of wire-mesh glass and tiles, all of the 32 materials tested in [27] had a reflection loss greater than 5dB, with typical losses exceeding 10dB. As a result, the amplitude of most multipath reflections in 60GHz channels will be relatively small. For example, the extensive measurements in [31] conclude that in the absence of strong reflectors, "the reflected multipath components are at least 10dB below the LOS component." Similarly, the delay spread of several different interior structures was measured at both 1.7GHz and 60GHz. In all cases, the delay spread measured at 60GHz was between two to four times smaller than that measured at 1.7GHZ. Additional measurements of 60GHz indoor channel properties are discussed in the next section.

9.2. Channel Properties

The aim of the measurement and simulation campaigns summarized here was to extract meaningful properties of the 60GHz channel. While the exact metric extracted differed from study to study, the metrics can be roughly grouped into the following categories:

- **Temporal characterization of channel multipath**: A variety of metrics were extracted to determine the temporal characteristics of the channel multipath. Some metrics included RMS delay speread, Rician k-factor and 90% settling time.
- **Spatial characterization of channel multipath**: Some of the studies characterized the spatial nature of the 60GHz channel multipath. For instance, [31] conducted extensive spatial measurement using highly directional antenna to extract angle of arrival information. Other studies measured the

impact of antenna directivity, alignment, and polarization on the temporal properties of the multipath channel.

- **Path loss**: Most studies conducted a set of location-specific path loss measurements. For instance, [31] reported the path loss as a function of distance in an interior corridor. This is the simplest metric extracted, and while it provides the least level of detail, the overall path loss in an indoor environment is of crucial importance.

9.3. Summary

A few key points about the 60GHz channel can be culled from the wealth of data available in the literature. They are summarized below:

- **Common building materials significantly attenuate 60GHz transmission.** Many indoor building materials are relatively opaque to 60GHz signal radiation, especially when compared to lower frequencies. In the absence of a strong reflective path, the extra path loss incurred in NLOS environments would significantly degrade the overall performance of the wireless link.
- **Common building materials are poor reflectors at 60GHz**. With the exception of metallic objects, most other building materials do not reflect 60GHZ radiation very well. Also, the reflections tend to be specular in nature, rather than diffuse. As a result, the multipath at 60GHz will be smaller than the multipath at lower frequencies.
- **Configurations with omnidirectional antennae will require additional techniques to mitigate multipath, even in LOS conditions**. Delay spreads with omnidirectional antenna were measured in the range of 15-50ns in LOS conditions. Rician K-factors in the 1 to 5dB range would be common. When compared to the desired data rate of 1GB/s, the delay spread is big enough that significant efforts would be required to compensate the multipath. For instance, an OFDM approach would require over 100 subcarriers, and an equalizer might require over 100 taps.
- **Directional antenna can significantly decrease the channel multipath**. Moderately directive antennae (6 to 12 dBi) can reduce the delay spread below 10ns and maintain a Rician K above 10dB, even in some NLOS scenarios. Highly directive antennae (16dBi and above) can further reduce the delay spread to 1 to 5 ns range or below.
- **Directive antenna rely upon proper alignment of beam pattern to be effective**. Directive antennae can increase the received power due to their antenna gain. However, this benefit is lost if the antennae are not properly aligned. In fact, misalignment can cause upwards of 20-30dB of additional path loss, which is well in excess of the benefit provided by the antenna gain. Also, the delay spread and Rician K degrade with misalignment, and alignment sensitivity increases with antenna gain. A rule of thumb is that the pointing error must be less than 30% of the HPBW (Half Power Beamwidth) in order to suffer minimal performance degradation.

Chapter 10

Relevance to the Telecommunications Industry

The key factor for many industries to be on the cutting edge of wireless technology depends heavily on the use of accurate models to predict the functioning of their systems. Moreover, an accurate model of the environment where such systems are going to be deployed is vital for a market winning design, as it will satisfy the needs to a greater extent.

Accurate knowledge of the complex permittivity of PCB and packaging materials is needed for circuit design, minimization of crosstalk and characterization of signal-propagation speed. The research developed on Part I of this project provides a method to measure the complex permittivity and gives some valuable data that can be applied to circuit design for greater simulation accuracy and prediction of behavior at 60GHz.

Knowledge of the channel propagation characteristics when developing a new communications system is vital to determine the communication devices features. The research developed on Part II provides a tool for channel measurement.

The fact that this project has been developed entirely at Broadcom Corporation, one of the world's largest fabless semiconductor companies and global leader in semiconductors for wired and wireless communications, is proof of the increasing interest of the Telecommunications Industry in 60GHz communications and their need to better understand the 60GHz channel.

Chapter 11

Future Work

The development of communication systems efficiently working on the 60GHz band still presents a lot of unknowns future research must give an answer to. The research and results provided in this thesis can further be complemented with work on the following topics:

- Permittivity measurements using other techniques: Will allow contrast between measurement results from various techniques and awareness of the errors and uncertainties incurred in the application of each method.
- Extension of the measurements to silicon and radome materials.
- Development of a mathematical model that characterizes the two-layer stripline method.
- Design of an on-package 60GHz antenna array, with beamforming capability: Cost reduction and antenna feeding losses drive the tendency to smaller on-chip antennas and arrays. Beamforming will be a must for pointing high-gain antennas accurately.
- Design of different 60GHz antennas (arrays) for particular devices (TV, cell phone) depending on angular coverage and gain requirements: The standards under definition envision different electronic devices and applications for the 60GHz band, each with different coverage, bandwidth and transmission data rates, that will require different antenna models.

Bibliography

[1] J. Feorster, E. Green, S. Somayazulu, D. Leeper, “Ultra-WideBand Technology for Short or Medium Range Wireless Communications”, Intel Architecture Labs.

[2] B. Razavi, “Gadgets Gab at 60GHz”, *Spectrum, IEEE*, vol. 45, no. 2, pp. 46-58, February 2008.

[3] C. Chong, K. Hamaguchi, P. Smulders, S. Yong, “Millimeter-Wave Wireless Communication Systems: Theory and Applications”, *Wireless Communications and Networking, EURASIP Journal on*, vol. 2007.

[4] “Rules to permit use of radio Frequencies Above 40GHz for New Radio Applications.” FCC ET Docket, no. 94-124, December 1995.

[5] “Amendment of Part 2 of the Commission’s Rules to Allocate Additional Spectrum to the Inter-Satellite, Fixed, and Mobile Services and to Permit Unlicensed Devices to Use Certain Segments in the 50.2-50.4GHz and 51.4-71.0GHz Bands.” FCC ET Doket, no. 99-261, December 2000.

[6] R. Fisher, “60GHz WPAN Standardization within IEEE 802.15.3c”, *Systems and Electronis, 2007, International Symposium on*, pp. 103-105, July 2007.

[7] WirelessHD Consortium. [Online] http://www.wirelesshd.org.

[8] J. Park, Y. Wang, T. Itoh, “A 60GHz Integrated Antenna Array for High-Speed Digital Beamforming Applications”, *Microwave Symposium Digest, 2003 IEEE MTT-S International*, vol. 3, pp. 1677-1680, June 2003.

[9] D. McPherson, D. Bates, M. Lang, B. Edward, D.Helms, “Active Phased Arrays for Millimeter Wave Communications Applications”, *Military Communications Conference, MILCOM’95, IEEE*, vol. 3, pp. 1061-1065, November 1995.

[10] J.A.G. Akkermans, M.H.A.J. Herben, “Planar Beam-Forming Array for Broadband Communication in the 60GHz Band”, *Antennas and Propagation, EuCAP 2007, The Second European Conference on*, pp. 1-6, November 2007.

[11] k. Wu, Y.Huang, “LTCC Technology and Its Applications in High Frequency Front End Modules”, *Antennas, Propagation and EM Theory, Proceedings, 2003 6th International Symposium on*, pp. 730-734, October 2003.

[12] J. Baker-Jarvis, M. D. Janezic, B. Riddle, C. L. Holloway, N.G. Paulter and J.E. Blendell, " Dielectric and Conductor-Loss Characterization and Measurements on Electronic Packaging Materials", *NIST Technical Note* 1520, July 2001.

[13] N. J. Damsakos and B. J. Kelsall, "Cavity Techniques for Substrate Properties at Microwave/Millimeter-Wave Bands", *Microwave Journal*, vol. 46, no. 12, pp. 112, December 2003.

[14] Papoulis, A. "The Fourier Integral and Its Applications", New York: McGraw-Hill, 1987.

[15] N. K. Das, S. M. Voda and D. M. Pozar, "Two Methods for the Measurement of Substrate Dielectric Constant", *Microwave Theory and Techniques, IEEE Transactions on*, vol. MTT-35, no. 7, pp. 636-642, July 1987.

[16] T. Zwick, A. Chandrasekhar, C. W. Baks, U. R. Pfeiffer, S. Brebels, and B. Gaucher, " Determination of the Complex Permittivity of Packaging Materials at Millimeter-Wave Frequencies", *Microwave Theory and Techniques, IEEE Transactions on*, vol. 54, no. 3, pp.1001-1010, March 2006.

[17] k. Sarabandi, E. Li, "Microstrip Ring Resonator for Soil Moisture Measurements", *Geoscience and remote sensing, IEEE Transactions on*, vol. 35, no. 5, pp. 1223-1231, September 1997.

[18] Ansoft Corportaion "HFSS Port Series: Coplanar Waveguide". [Online] http://ansoft.com/ots/training.cfm.

[19] L. Correia, J. Reis. P. Frances, "Analysis of the Average Power to Distance Decay Rate at the 60GHz Band", *Vehicular Technology Conference, IEEE 47th*, vol. 2, pp. 994-998, May 1997.

[20] C. Anderson, T. Rappaport, "In-Building Wideband Partition Loss Measurements at 2.5 and 60GHz", *Wireless Communications, IEEE Transactions on*, vol. 3, pp. 922-928, May 2004.

[21] R. Davies, M. Bensebti, M. Beach, J. McGeehan, "Wireless Propagation Measurements in Indoor Multipath Environments at 1.7GHz and 60GHz for Small Cell Systems", *Vehicular Technology Conference, IEEE 41st Proceedings of*, pp. 489-593, May 1991.

[22] G. Durgin, T. Rappaport, H. Xu, "Measurements and Models for Radio Path Loss and Penetration Loss In and Around Homes and Trees at 5.85GHz", Communications, IEEE Transactions on, vol. 46, pp. 1484-1496, November 1998.

[23] J. Proakis, "Digital Communications", 3rd Edition, Boston: McGraw-Hill, 1995.

[24] J. Laskar, S. Pinel, C-H. Lee, S. Sarkar, B. Perumana, J. Papapolymerou and E. Tentzeris, "Circuit and Module Challenges for 60 GHz Gb/s Radio", Wireless *Communications and Applied Computational Electromagnetics, IEEE/ACES International Conference on*, pp. 447-450, April 2005.

[25] D. Pozar, "Microwave Engineering", 2nd Edition, New York: John Wiley & Sons Inc., 1998.

[26] A. Cardama, L. Jofre, J. Rius, J. Romeu, S. Blanch, M. Ferrando, " Antenas", 2nd Edition, Barcelona: Edicions UPC, 2002.

[27] B. Langen, G. Lober, W. Herzig, "Reflection and Transmission Behaviour of Building Materials at 60GHz", *PIMRC, IEEE 5th International Symposium on*, vol. 2, pp. 505-509, September 1994.

[28] M. Williamson, "60GHz Measurement Program", Hewlett Packard Laboratories Internal Report, December 1997.

[29] L. Correia, P. Frances, "Transmission and Isolation of Signals in Buildings at 60GHz", *PIMRC, IEEE 6th International Symposium on*, vol. 3, pp. 1031, September 1995.

[30] P. Smulders, L. Correia, "Characterization of propagation in 60GHz radio channels", *Electronics and Communication Engineering Journal*, pp. 73-80, April 1997.

[31] H. Xu, V. Kukshya, T. Rappaport, "Spatial and Temporal Characteristics of 60-GHz Indoor Channels", *IEEE Journal on Selected Areas in Communications*, vol. 20, pp. 620-630, April 2002.

Annex I

V-connectors Specifications

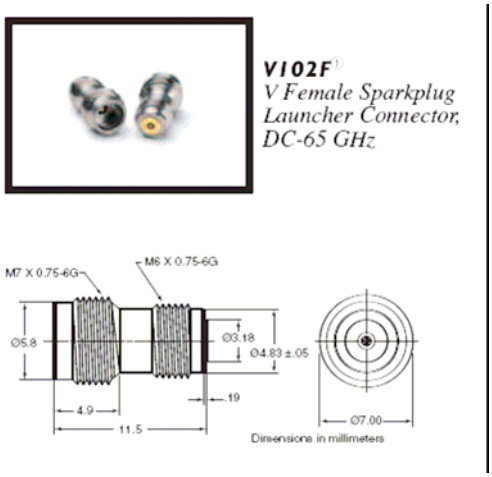

Fig. A.1: V102F Sparkplug Connector.

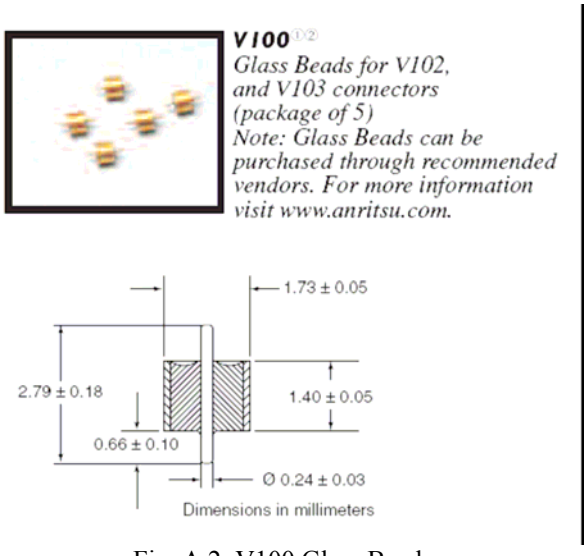

Fig. A.2: V100 Glass Beads

Annex II

Microstrip Test Fixture Design Drawings

In this section we include the Autocad Drawing "RF Test Fixture Part A" used to manufacture the microstrip test fixture for the experiments of Part I, described in Chapter 5:

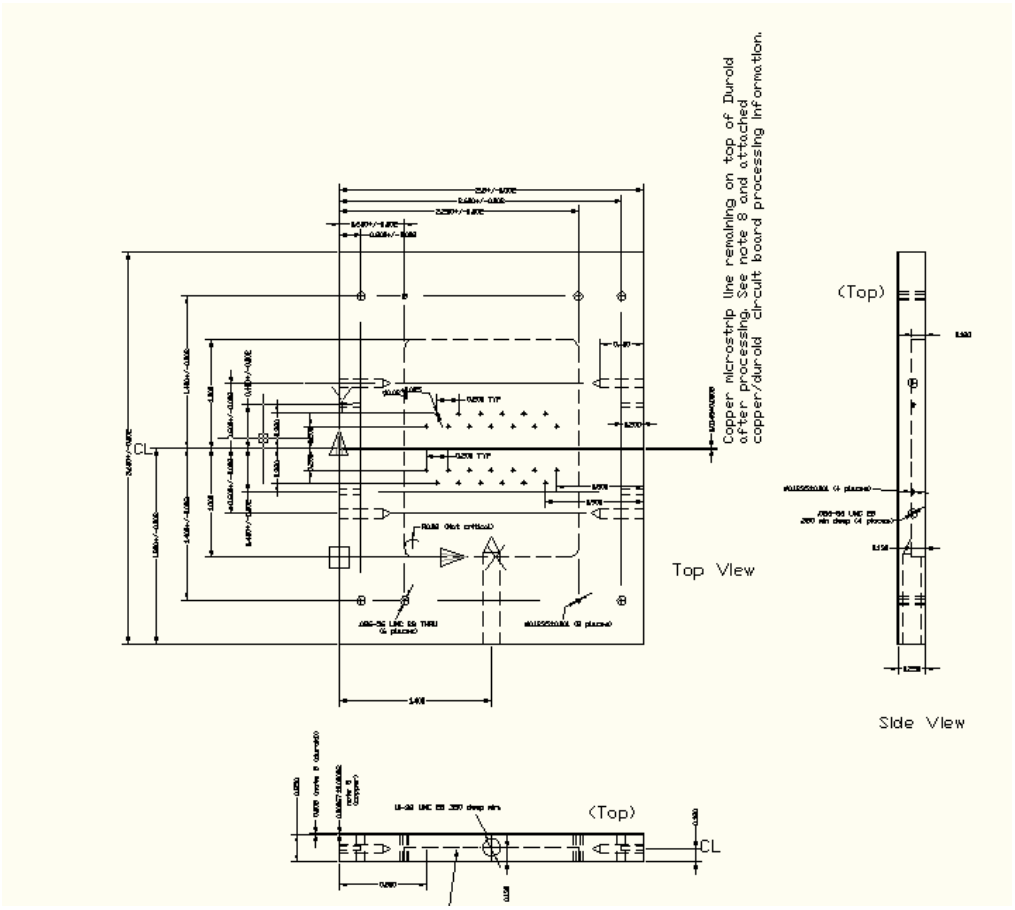

Fig. A.3: Miniature view of the RF Test Fixture Part A Autocad Drawing.

Annex III

Endwave Transceivers and WR15 Specifications

III-A: EW601W and EW602W 60GHz Transceivers Specifications (dimensions in millimeters)

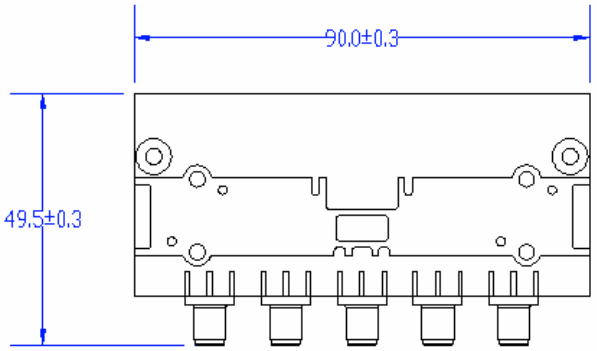

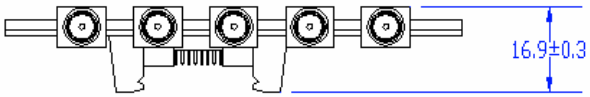

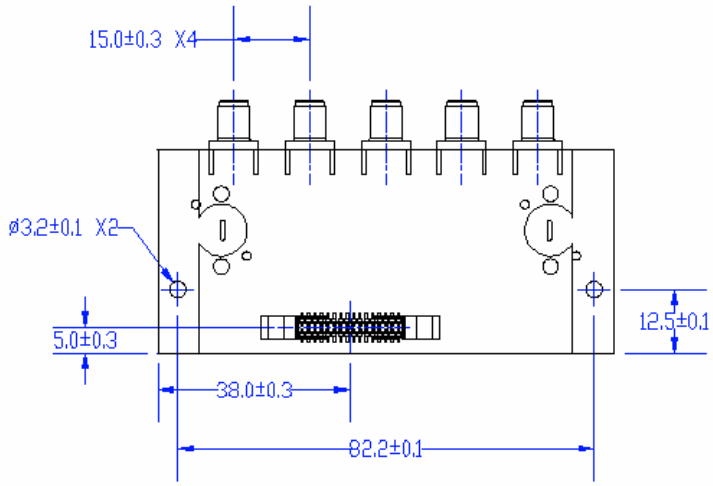

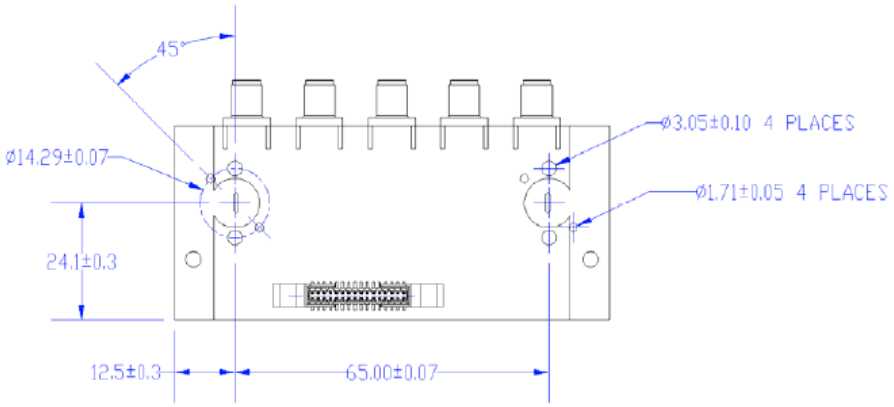

Fig. A.4: EW601W and EW602W Waveguide port configuration –note that off-center positioning of the flanges with respect to the ports on the transceivers is intentional.

III-B: WR-15 Rectangular Waveguide Specifications

Rectangular Waveguide Specifications and MIL-Specification Cross Reference

Frequency GHz	EIA Waveguide	Frequency Band	TE_{10} Mode Cutoff, GHz	Inside Waveguide Dimensions, Inches (mm)	Flange Type and Descriptive Interface Standards			
					Size/Type	Connective Hole Type	MIL-Spec Flange MIL.F-3922	UG-XXX/U Equivalent (Referenece)
18-26.5	WR-42	K	14.08	0.420 x 0.170 (10.7 x 4.3)	.875/SQ 1.125/RD	CLR. HOLES THD. HOLES	/54-001 /67B-004	UG-595/U
26.5-40	WR-28	Ka	21.10	0.280 x 0.140 (7.11 x 3.56)	.750/SQ 1.125/RD	CLR. HOLES THD. HOLES	/54-003 /67B-005	UG-599/U UG-381/U
33-50	WR-22	Q	26.35	0.224 x 0.112 (5.7 x 2.8)	1.125/RD	THD. HOLES	/67B-006	UG-383/U
40-60	WR-19	U	31.41	0.188 x 0.094 (4.8 x 2.4)	1.125/RD	THD. HOLES	/67B-007	UG-383/U-M
50-75	WR-15	V	39.90	0.148 x 0.074 (3.8 x 1.9)	.750/RD	THD. HOLES	/67B-008	UG-385/U

Table A.1: Rectangular Waveguide Specifications and MIL-specification cross reference.

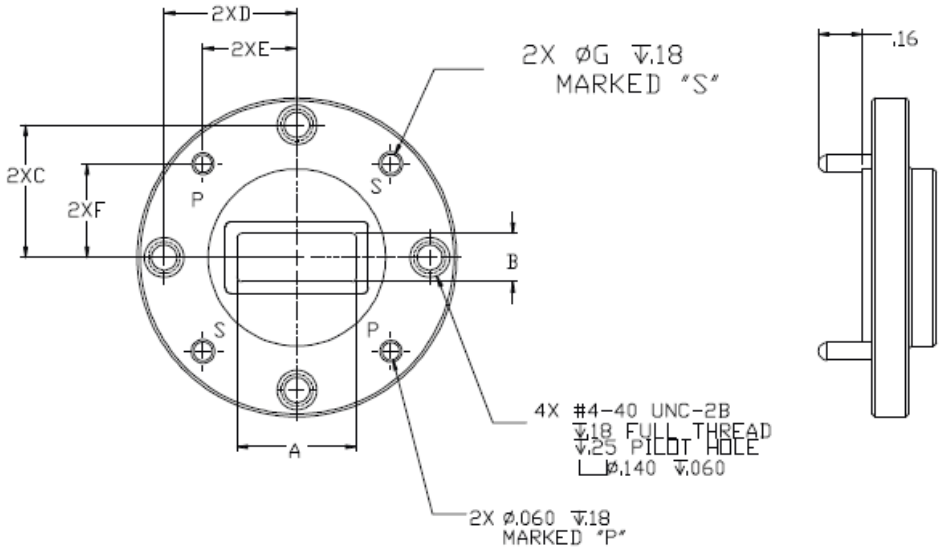

Positioning Dimensions

Model Number	WR-42	WR-28	WR-22	WR-19	WR-15
A, inches	0.420	0.280	0.224	0.224	0.148
B, inches	0.170	0.140	0.112	0.112	0.074
C, inches	0.468	0.468	0.468	0.468	0.280
D, inches	0.468	0.468	0.468	0.468	0.281
E, inches	0.331	0.331	0.331	0.331	0.199
F, inches	0.331	0.331	0.331	0.331	0.199
G, inches	0.067	0.067	0.067	0.067	0.067

Fig. A.5: Rectangular Waveguide Round Flange –Hole Positioning dimensions.

Annex IV

Matlab Code

IV-A: Array Factor Calculus

```
% Calculation of the array factor

close all;
clear all;

N=8;                                            % Number of antennas
an=ones(1,N);                                   % Feed amplitude at each antenna
freq=57*10^(9):0.1*10^9:63*10^9;                %Frequency vector
d=0.0025;                                       % Separation between antennas
alpha=0*pi()/180;                               % Progressive phase between elements
o=-pi():pi()/99.5:pi();
a1= 0.0087;                                     % E-plane Horn length
b=0.0019;                                       % H-plane Horn length
lh=0.005;                                       % H-plane Horn apperture length
Eo=1;
r=1;
maxphasedif=0;  % Maximum phase error at the radiation point (To calculate effects of random
phase deviation from nominal value between elements)

lambda = 2.9986*10^8./(freq*sqrt(1.0006));      % Wavelength
k=2*pi()./lambda;
Y=d*k'*cos(o)+alpha;
af=zeros(size(Y,1),size(Y,2));                  % Array Factor
angle=zeros(1,N);

for t=1:N
    angle(t)=(rand-0.5)*2*maxphasedif*pi()/180;
    af=af+an(t)*exp(i*(t*Y+angle(t)));          % Include error on the phase shift between
elements.
end

auxaf2=max(0,10*log10(abs(af(30,:)))+10);

% Plot the array factor
figure
axis off;
hold on;
axes('FontSize',12);
polar(o,auxaf2);
title('Array Factor(dB)');

% Plot the phase shift
figure
axis off;
hold on;
axes('FontSize',12);
scatter(1:8,angle*180/pi());
xlabel('Antenna Element');
ylabel('Phase Shift');
```

```
% Plot the amplitude
figure
axis off;
hold on;
axes('FontSize',12);
scatter(1:8,an);
xlabel('Antenna Element');
ylabel('Amplitude');
```

IV-B: Horn Antenna and Horn Antenna Array Radiation Patterns Calculus

```
% Calculate the E- and H-plane radiation patterns of Horn antennas
% Calculate the Array Factor and the radiation pattern of an H-plane Horn antenna array

clear all;
close all;

a=0.0087;                               % E-plane Horn length
b=0.0019;                               % H-plane Horn length
lh=0.005;                               % H-plane Horn apperture length
imp=370;                                % Wave impedance
lb=0.005;                               % Wavelength

zo=imp/(sqrt(1-(lb/(2*a))^2));
k=2*pi()/lb;
n_points_theta=180; %theta=o
n_points_phi=360;
phi=0:2*pi()/(n_points_phi):2*pi()*(1-1/n_points_phi);
o=0:pi()/(n_points_theta):pi()*(1-1/n_points_theta);
r=3;

integral = 0;
maxim=0;
Efield0=zeros(n_points_phi,n_points_theta);
Efield1=zeros(n_points_phi,n_points_theta);

for n=1:n_points_phi
        for m=1:n_points_theta
                kx=k*sin(o(m))*cos(phi(n));
                ky=k*sin(o(m))*sin(phi(n));
                Fun=@(x)cos(pi()/a*x).*exp(i*k.*(a^2/(8*lh)-x.^2./(2*lh))).*exp(i*kx.*x);

                if(ky==0)
                        Eo=i*exp(-i*k*r)/(2*lb*r)*(1+imp/zo*cos(o(m)))*sin(phi(n))*quad(Fun,-
                a/2,a/2)*b;
                        Ep=i*exp(-i*k*r)/(2*lb*r)*(imp/zo+cos(o(m)))*cos(phi(n))*quad(Fun,-
                a/2,a/2)*b;

                else
                        Eo=i*exp(-i*k*r)/(2*lb*r)*(1+imp/zo*cos(o(m)))*sin(phi(n))*quad(Fun,-
                a/2,a/2)*b*sin(ky*b/2)/(ky*b/2);
                        Ep=i*exp(-i*k*r)/(2*lb*r)*(imp/zo+cos(o(m)))*cos(phi(n))*quad(Fun,-
                a/2,a/2)*b*sin(ky*b/2)./(ky*b/2);
                end

                Efield0(n,m)=Ep;
                Efield1(n,m)=Eo;
                integral =
        integral+(abs(Eo)^2+abs(Ep)^2)*sin(o(m))*(2*pi()/n_points_phi)*(pi()/n_points_theta)*r^2;
                if sqrt(abs(Eo)^2+abs(Ep)^2)>maxim
                        maxim=sqrt(abs(Eo)^2+abs(Ep)^2);
                end
        end
end
```

```
Directivity = 4*pi*maxim^2*r^2/integral;
DirectivitydB = 10*log10(Directivity);

% H-plane Radiation Pattern
DirH=abs(Efield1(91,:)).^2*r^2*4*pi/integral;
DirectivityH=horzcat(DirH,fliplr(DirH));
DirectivityHdB=max(0,10*log10(DirectivityH)+10);

figure
axis off;
hold on;
axes('FontSize',12),
polar(phi+pi/2, DirectivityHdB);
title('H-Plane Radiation Pattern(dB)');

% E-plane Radiation Pattern
DirE=abs(Efield0(1,:)).^2*r^2*4*pi/integral;
DirectivityE=horzcat(DirE,fliplr(DirE));
DirectivityEdB=max(0,10*log10(DirectivityE)+10);

figure
axis off;
hold on;
axes('FontSize',12),
polar(phi+pi/2, DirectivityEdB);
title('E-Plane Radiation Pattern(dB)');

% Calculation of the array factor
N=8;                                    %Number of antennas
an=ones(1,N);                           %Feed amplitude at each antenna
d=0.0025;                               %Separation between antennas
alpha=0*pi/180;                         %Progressive phase between antennae

Y=k*d.*cos(phi)+alpha;

af=zeros(size(Y));
for t=1:N
    af=af+an(t)*exp(i*t*Y);
end

afactor=max(0,10*log10(abs(af))+10);
figure
axis off;
hold on;
axes('FontSize',12),
polar(phi, afactor);
title('Array Factor(dB)');

% Calculation of the array radiation pattern

afaux=horzcat(af,af);
afdef=afaux(91:360+90);
RP=afdef.*horzcat(Efield1(91,:),fliplr(Efield1(91,:)));
RPDir=abs(RP).^2*r^2*4*pi/(integral*N);
RPDirdB=max(0,10*log10(RPDir)+10);

figure
axis off;
hold on;
axes('FontSize',12),
polar(phi+pi/2, RPDirdB);
title('Array Radiation Pattern(dB)');

Dirmax=max(RPDirdB);
```

IV-C: Open-ended Waveguide Radiation Pattern Calculus

```
% Calculate the E- and H-plane radiation patterns of an open-ended waveguide

clear all;
close all;

a=0.0038;                               % E-plane Horn length
b=0.0019;                               % H-plane Horn length
lb=0.005;                               % Wavelength
imp=370;                                % Wave impedance

zo=imp/(sqrt(1-(lb/(2*a))^2));
k=2*pi()/lb;
n_points_theta=180;
n_points_phi=360;
phi=0:2*pi()/(n_points_phi):2*pi()*(1-1/n_points_phi);
o=0:pi()/(n_points_theta):pi()*(1-1/n_points_theta);
r=3;

integral = 0;
maxim=0;
Efield0=zeros(n_points_phi,n_points_theta);
Efield1=zeros(n_points_phi,n_points_theta);

for n=1:n_points_phi
        for m=1:n_points_theta
                kx=k*sin(o(m))*cos(phi(n));
                ky=k*sin(o(m))*sin(phi(n));

                if(ky==0)
                        Eo=i*exp(-
                i*k*r)/(2*lb*r)*(1+imp/zo*cos(o(m)))*sin(phi(n))*pi()*a/2*(cos(kx*a/2)/((pi()/2)^
                2-(kx*a/2)^2))*b;
                        Ep=i*exp(-
                i*k*r)/(2*lb*r)*(imp/zo+cos(o(m)))*cos(phi(n))*pi()*a/2*(cos(kx*a/2)/((pi()/2)^2-
                (kx*a/2)^2))*b;

                else
                        Eo=i*exp(-
                i*k*r)/(2*lb*r)*(1+imp/zo*cos(o(m)))*sin(phi(n))*pi()*a/2*(cos(kx*a/2)/((pi()/2)^
                2-(kx*a/2)^2))*b*sin(ky*b/2)/(ky*b/2);
                        Ep=i*exp(-
                i*k*r)/(2*lb*r)*(imp/zo+cos(o(m)))*cos(phi(n))*pi()*a/2*(cos(kx*a/2)/((pi()/2)^2-
                (kx*a/2)^2))*b*sin(ky*b/2)./(ky*b/2);
                end

                Efield0(n,m)=Ep;
                Efield1(n,m)=Eo;
                integral =
        integral+(abs(Eo)^2+abs(Ep)^2)*sin(o(m))*(2*pi()/n_points_phi)*(pi()/n_points_theta)*r^2;

                if sqrt(abs(Eo)^2+abs(Ep)^2)>maxim
                         maxim=sqrt(abs(Eo)^2+abs(Ep)^2);

                end
        end
end

Directivity = 4*pi*maxim^2*r^2/integral;
DirectivitydB = 10*log10(Directivity);

% H-plane Radiation Pattern
DirH=abs(Efield1(271,:)).^2*r^2*4*pi/integral;
DirectivityH=horzcat(DirH,fliplr(DirH));
DirectivityHdB=max(0,10*log10(DirectivityH)+10);
```

```
figure
axis off;
hold on;
axes('FontSize',12),
polar(phi+pi/2, DirectivityHdB);
title('H-Plane Radiation Pattern(dB)');

% E-plane Radiation Pattern
DirE=abs(Efield0(360,:)).^2*r^2*4*pi/integral;
DirectivityE=horzcat(DirE,fliplr(DirE));
DirectivityEdB=max(0,10*log10(DirectivityE)+10);

figure
axis off;
hold on;
axes('FontSize',12),
polar(phi+pi/2, DirectivityEdB);
title('E-Plane Radiation Pattern(dB)');
```

Annex V

Waveguide Antenna Array and Calibration Piece Design Drawings

In this section we include the Pro/Engineer Drawings used to manufacture the 60GHz waveguide array described in Chapter 8:

- Waveguide Array: Divided in two equal halves that match together, to enable machining.
- Complete Waveguide Array
- Calibration Piece: Divided in two equal halves that match together, to enable machining.
- Waveguide Array + mounted Calibration Piece
- Waveguide Array + mounted Calibration Piece as seen from outside